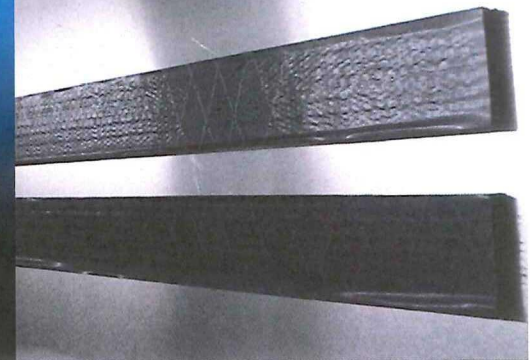
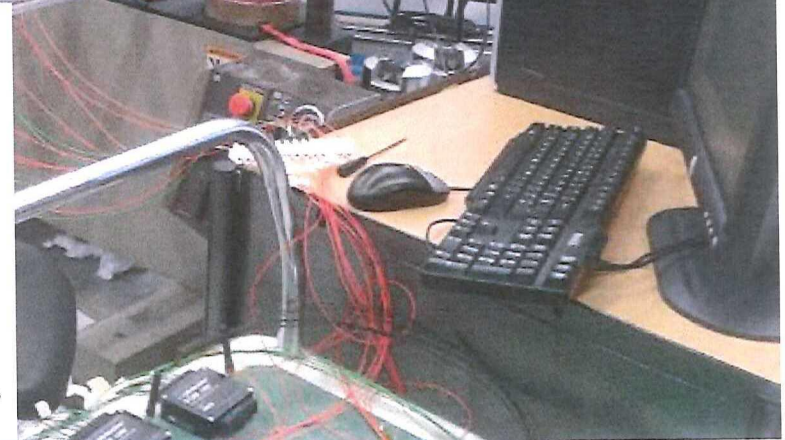
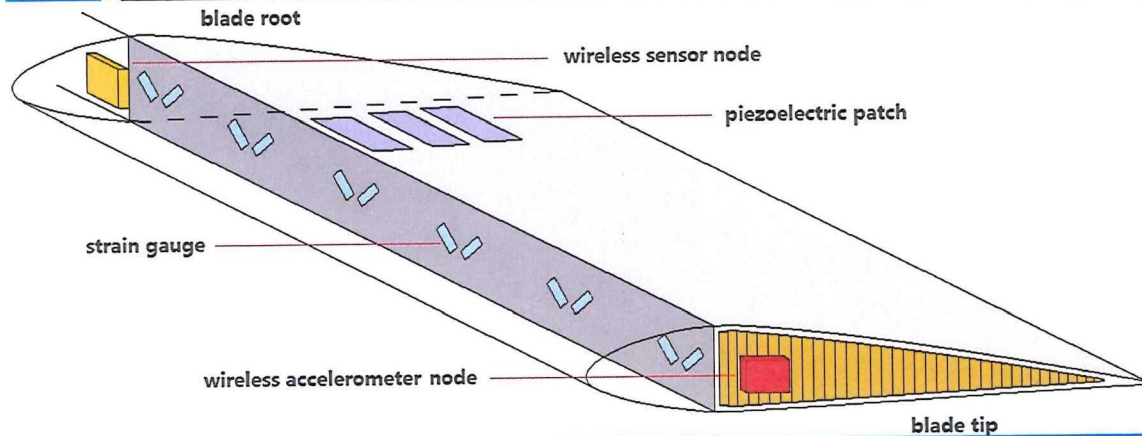
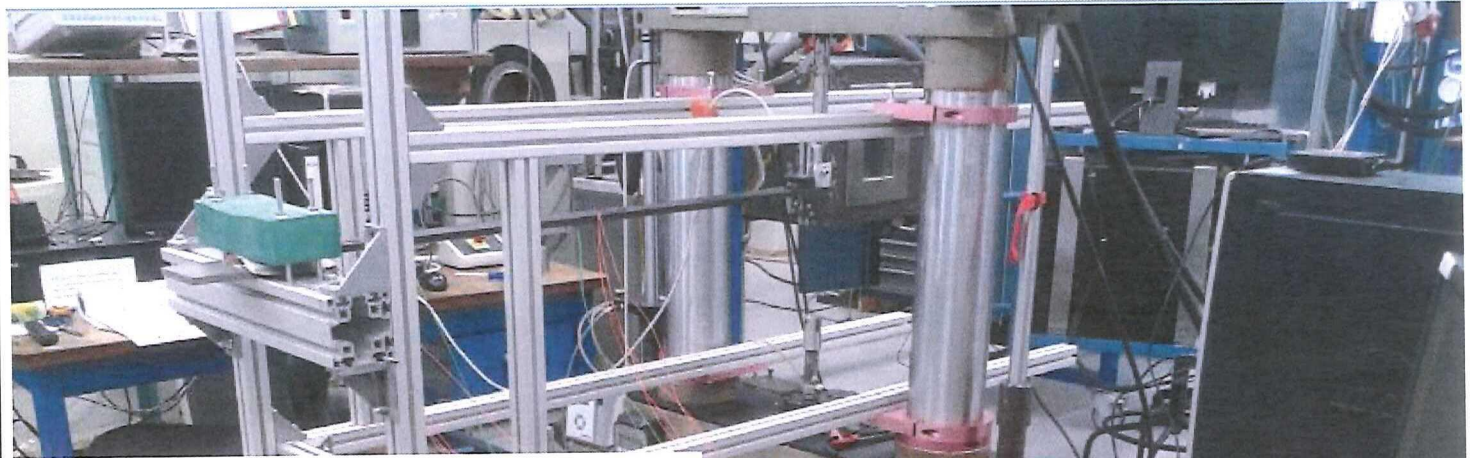
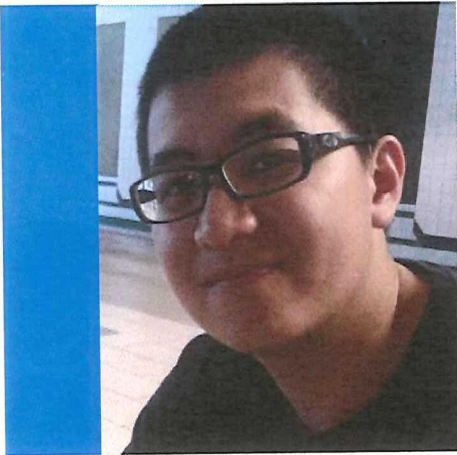


Structural Health Monitoring of a Helicopter Rotor Blade with a Wireless Sensor Network

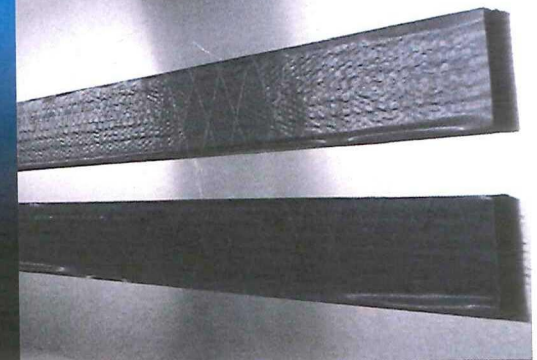
Donghang Wang
March 30, 2015





Structural Health Monitoring of a Helicopter Rotor Blade with a Wireless Sensor Network

Donghang Wang
March 30, 2015





MASTER OF SCIENCE THESIS

Structural Health Monitoring of a Helicopter Rotor Blade with a Wireless Sensor Network

Donghang Wang

Faculty of Aerospace Engineering • Delft University of Technology



Structural Health Monitoring of a Helicopter Rotor Blade with a Wireless Sensor Network

Master of Science Thesis

For obtaining the degree of Master of Science in Aerospace Engineering
at Delft University of Technology

Donghang Wang

Faculty of Aerospace Engineering · Delft University of Technology

Delft University of Technology
Faculty of Aerospace Engineering
Department of Aerospace Structures and Materials

GRADUATION COMMITTEE

Dated: 30 Mar. 2015

Chair holder:

Prof. dr. ir. Rinze Benedictus

Committee members:

Dr. Roger M. Groves

Dr. Marilena D. Pavel

Abstract

Rotor blades are critical structures of a helicopter due to their severe loading and significant deformation during operations. Out of considerations of flight safety and economic benefits, there is a need to monitor the structural health of rotor blades. However, applications of a structural health monitoring (SHM) system for rotor blades are limited by issues of positioning, communicating, and powering of sensors on the blades. In this thesis, a wireless sensor network (WSN) is proposed to be employed in an on-board SHM system and to perform real-time measurements of composite blades' structural parameters. Based on this WSN, the SHM system is capable of directly monitoring the operation of rotor blades and detecting defects on them by analyzing the measurement results. Such an SHM system for composite rotor blades is especially needed by civil helicopters, which have a dramatically increasing number and are used for various operations nowadays.

In order to configure the SHM system incorporating a WSN, specimens simplified from the R22 helicopter rotor blades were designed and manufactured, and experiments including stiffness tests, static tests, slow dynamic tests, and dynamic tests were performed. Testing results from these specimens were compared and analyzed to investigate the rotor blade performance in a simulated dynamic condition, to verify the applicability and reliability of the WSN, to determine the organization of sensors and the WSN components, and to identify useful indicators of defects. According to the experimental results, it was concluded that rotor blade performance such as strain level and distribution in highly dynamic conditions is completely different with that in a static condition, and affected by the movement frequency of the rotor blade. In addition, the WSN was verified to be capable of performing accurate measurements on quickly moving specimens and implementing real-time wireless data transmissions.

Shear strains on the front surface of the composite material wrapping the honeycomb structure in a rotor blade are proposed to be a defect indicator because an obvious change in shear strains was found induced by the presence of an artificial debonding area during experiments. The acceleration at the blade tip is another important parameter as it is possible to monitor the operation condition of the blade by analyzing acceleration measurements. The work of this thesis gave a full picture of the configuration of a SHM system based on a WSN, determined candidates of structural parameters to indicate defects or to monitor the operation, and provided guidance on work to establish a complete practical SHM system for rotor blades.

Acknowledgements

Foremost, I would like to express my deepest thanks to my supervisor, Dr. Roger M. Groves, for his guidance and continuous support throughout research and writing of this thesis. His patience, encouragement, and immense knowledge became important motivations for my master study. I have learnt from Roger vital skills of critical thinking and rigorous planning. His work of constructive and detailed revision of my technical writing was invaluable and will benefit my writing style all my life. I cannot think of a better supervisor to have.

Besides my supervisor, I wish to thank my colleagues and friends in the Aerospace Non-Destructive Testing Laboratory, TU Delft. Special thanks to Dr. Andrei Anisimov, Dr. Ping Liu, Victor Fraguas Garcia, and Guyonne Alleman for their practical help in the laboratory work. My sincere thanks also go to Dr. Marcias J. Martinez, Adrian Fernandez Vigo, and the technicians of the Delft Aerospace Structures and Materials Laboratory: Berthil Grashof, Misja Huizinga, Gertjan Mulder, Johan Boender, and Cees Paalvast for offering me guidances in laboratory techniques. A special mention is for Hans van der Marel of AE Sensors, for our discussions about the wireless sensor node setup.

Finally, the Department of Aerospace Structures and Materials has provided me support and equipment to complete this thesis.

Table of Contents

Chapter 1 Introduction	1
1.1 Background	1
1.1.1 Structural health monitoring.....	1
1.1.2 SHM on helicopter rotor system	1
1.2 Objective and motivation.....	2
1.2.1 Goal	2
1.2.2 Motivation.....	3
1.2.3 Thesis question.....	4
1.3 Outline.....	4
1.3.1 Scope of work.....	4
1.3.2 Outline.....	5
1.4 References.....	6
Chapter 2 Composite Specimen	7
2.1 Theory	7
2.1.1 Composite rotor blade	7
2.1.2 Manufacture.....	8
2.1.3 Defects.....	9
2.2 Design.....	11
2.2.1 R22	11
2.2.2 R22 rotor blade	12
2.2.3 Specimen design	13
2.2.3.1 Structure.....	13
2.2.3.2 Dimension	14
2.2.3.3 Skins and walls.....	15
2.2.3.4 Defect	15
2.3 Manufacture.....	15
2.3.1 CFRP plate fabrication	16
2.3.1.1 Preparation of carbon fiber fabric.....	16
2.3.1.2 Mold cleaning.....	16

2.3.1.3. Placement.....	16
2.3.1.4. Vacuum connection.....	17
2.3.1.5. Resin preparation	18
2.3.1.6. Resin infusion	18
2.3.2 Adhesive bonding.....	19
2.3.2.1 Preparation.....	19
2.3.2.2 Placement.....	20
2.3.2.3 Sending to autoclave	20
2.3.3 Optimized fabrication setup.....	21
2.3.4 Specimen.....	22
2.4 Summary	22
2.5 References.....	24

Chapter 3 Measurement and Monitoring Hardware.....25

3.1 Introduction.....	25
3.2 Strain gauge.....	25
3.2.1 Theory	25
3.2.1.1 Electrical strain gauge.....	25
3.2.1.2 Fiber optic sensor.....	26
3.2.1.3 Selection.....	27
3.2.2 Placement.....	27
3.2.2.1 Strain gauge layout.....	28
3.2.2.2 Bridge circuit configuration	29
3.3 Wireless sensor networks	30
3.3.1 Theory	30
3.3.2 Application	31
3.3.2.1 LXRS protocol.....	31
3.3.2.2 V-Link-LXRS sensor node	32
3.3.2.3 G-Link-LXRS sensor node.....	32
3.3.2.4 Base Station.....	33
3.3.2.5 Node Commander	33
3.4 Other hardware	34
3.5 Summary	34
3.6 References.....	36

Chapter 4 Stiffness Test39

4.1 Introduction.....	39
4.2 Test setup	39
4.3 Theory	40
4.4 Experiment	41
4.4.1 Beam 1	42
4.4.2 Beam 2 and beam 3.....	42
4.5 Results and analysis.....	42
4.5.1 Beam 1	42

4.5.2 Beam 2 and beam 3.....	44
4.5.3 Analysis.....	47
4.5 Summary	48
4.6 References.....	49
Chapter 5 Static Test and Slow Dynamic Test	51
5.1 Introduction.....	51
5.2 Test setup	51
5.3 Experiment	53
5.3.1 Static test.....	53
5.3.1.1 Beam 1.....	53
5.3.1.2 Beam 2 and beam 3.....	55
5.3.2 Slow dynamic test	55
5.4 Results and analysis.....	57
5.4.1 Static test.....	57
5.4.1.1 Beam 1.....	57
5.4.1.2 Beam 2 and beam 3.....	62
5.4.1.2.1 WSN noise signal	62
5.4.1.2.2 Strain	64
5.4.1.2.3 Load.....	67
5.4.1.3 Analysis.....	68
5.4.1.3.1 Bending strain.....	68
5.4.1.3.2 Shear strain.....	70
5.4.2 Slow dynamic test	71
5.5 Summary	73
5.6 References.....	75
Chapter 6 Dynamic Test.....	77
6.1 Introduction.....	77
6.2 Test setup	77
6.3 Experiment	79
6.4 Results and analysis.....	81
6.4.1 Load.....	81
6.4.2 Strain	84
6.4.2.1 Strain measurement.....	84
6.4.2.2 Shear strain noise	88
6.4.2.3 Strain ratio.....	90
6.4.3 Acceleration	94
6.5 Summary	98
Chapter 7 Discussion.....	101
7.1 Specimen.....	101
7.2 Wireless sensor network.....	102
7.3 Dynamic effect	103

7.3.1 Force.....	103
7.3.2 Strain	104
7.3.3 Acceleration	104
7.4 Debonding	105
7.5 Noise.....	105
7.6 Summary	106

Chapter 8 Conclusion and Recommendation109

8.1 Thesis work review.....	109
8.2 Results	109
8.3 Limitations	111
8.4 Recommendations	111
8.5 Design proposal.....	112

List of Figures

Figure 2. 1	Sectional view of a composite Sea King helicopter rotor blade (5).....	9
Figure 2. 2	Water percolates between two borders near the stiffener (10)	10
Figure 2. 3	Robinson R22 (13)	11
Figure 2. 4	Rotor hub of the R22 (16).....	12
Figure 2. 5	Cross section of R22 rotor blade (17)	12
Figure 2. 6	Sectional view of experimental model.....	14
Figure 2. 7	Placement for resin infusion	17
Figure 2. 8	Top view of adhesive film bonding placement for two specimens	21
Figure 2. 9	Sketch of protective wooden blocks.....	21
Figure 2. 10	Final products of beam 2 and beam 3.....	22
Figure 3. 1	Three-element stacked rosette strain gauge (3).....	26
Figure 3. 2	Principle of FBG sensor operation (7)	27
Figure 3. 3	Strain gauge layouts on (a) beam 1 and (b) beam 2/ beam 3	28
Figure 3. 4	Bridge circuits for strain measurement.....	29
Figure 3. 5	Configuration of the wireless sensor network (16)	31
Figure 3. 6	V-Link-LXRS sensor node (18).....	32
Figure 3. 7	G-Link-LXRS sensor node (19)	33
Figure 3. 8	WSDA-Base-102-LXRS base station (20).....	33
Figure 4. 1	Stiffness test rig.....	40
Figure 4. 2	Placement of beam 1 in the four consecutive stiffness tests.....	42
Figure 4. 3	Comparison of stiffness in two directions.....	43
Figure 4. 4	Stiffness measurements of beam 1 in two directions.....	43
Figure 4. 5	Stiffness measurements of beam 2 in two directions.....	44
Figure 4. 6	Performance of beam 2 in stiffness tests.....	45
Figure 4. 7	Structural behavior at the debonding area in two stiffness tests on beam 3	46
Figure 5. 1	Schematic diagram of test setup for static tests and slow dynamic tests.....	52
Figure 5. 2	Actuator setup (a) and mounting structure (b)	53
Figure 5. 3	Dissymmetry of lift causes blade flapping.....	56

Figure 5. 4	Comparison of (a) bending strain and (b) shear strain measured by two measurement systems for beam 1 in pre-test 1	57
Figure 5. 5	Comparison between conditions with and without sensor node attachment for (a) bending strain and (b) shear strain for beam 1 in pre-test 2	58
Figure 5. 6	Recordings of bending strain with different holding time.....	59
Figure 5. 7	Comparison of (a) bending strain and (b) shear strain measurements with different holding times.....	59
Figure 5. 8	Relation between bending strains at different locations	60
Figure 5. 9	Comparison of shear strains at different locations	60
Figure 5. 10	Strain recording during a test with multiple cycles	61
Figure 5. 11	Force recording during a test with multiple cycles.....	61
Figure 5. 12	Data of strain gauge 1 in frequency domain with 64 Hz sampling rate.....	62
Figure 5. 13	Data of strain gauge 1 in frequency domain with 8 Hz sampling rate.....	63
Figure 5. 14	Aliasing of noise signal	64
Figure 5. 15	Bending strain recording of strain gauge 1 on beam 3.....	65
Figure 5. 16	Shear strain recording of strain gauge 6 on beam 3.....	65
Figure 5. 17	Strain gauge layout on beams 2 and 3	65
Figure 5. 18	Comparison of strain ratios between beam 2 and beam 3	66
Figure 5. 19	Load history for beam 2 and beam 3 in static test.....	67
Figure 5. 20	Free body diagram analysis of bending strain.....	69
Figure 5. 21	Recordings of bending strain at different frequencies.....	72
Figure 5. 22	Recordings of shear strain at different frequencies	72
Figure 6. 1	Fatigue machine (a) and metal frame fixed to the fatigue machine (b).....	78
Figure 6. 2	Connection between the fatigue machine and the specimen	78
Figure 6. 3	Physical layout of the experimental apparatus during a dynamic test	79
Figure 6. 4	Schematic plot of dynamic testing system incorporating a WSN.....	80
Figure 6. 5	Collection of maximum forces with various movement parameters for beam 3	82
Figure 6. 6	Comparison between (a) symmetrical and (b) asymmetrical movement patterns with the same amplitude for beam 3.....	82
Figure 6. 7	Load history and displacement recording in movement (-10 mm, 10 mm) at 16 Hz for beam 3	83
Figure 6. 8	Force data in the frequency domain in movement (-5 mm, 5 mm) at 16 Hz for beam 3	84
Figure 6. 9	Bending strain recording of beam 2 in movement (-20 mm, 20 mm) at 8 Hz....	85
Figure 6. 10	Bending strain recording of beam 3 in movement (-20 mm, 20 mm) at 8 Hz	86
Figure 6. 11	Collection of bending strains measured on beam 2 at 8Hz.....	86
Figure 6. 12	Comparison in the variation trend of bending strains from (a) SG3 and (b) SG4 with frequency between beam 2 and beam 3	87
Figure 6. 13	Shear strain recording of beam 2 in movement (-20 mm, 20 mm) at 8 Hz.....	88
Figure 6. 14	Shear strain measured by SG5 on (a) beam 2 and (b) beam 3 in the frequency domain	89

Figure 6. 15	Shear strain measured by wired system in the frequency domain	90
Figure 6. 16	Bending strain ratio (SG2/SG1) of (a) beam 2 and (b) beam 3	90
Figure 6. 17	Comparison of bending strain ratio (SG2/SG1) between beam 2 and beam 3	91
Figure 6. 18	Bending strain ratio (SG4/SG3) of (a) beam 2 and (b) beam 3	91
Figure 6. 19	Comparison of bending strain ratio (SG4/SG3) between beam 2 and beam 3	92
Figure 6. 20	Shear strain relative difference of (a) beam 2 and (b) beam 3	92
Figure 6. 21	Comparison of shear strain relative difference between beam 2 and beam 3	93
Figure 6. 22	Shear strain recording of beam 3 in the movement (20 mm amplitude, 8 Hz)	94
Figure 6. 23	Relationship between accelerations (Ch1 and Ch2) and amplitude	95
Figure 6. 24	Relationship between accelerations (Ch1 and Ch2) and frequency	95
Figure 6. 25	Collection of accelerations (Ch3) on beam 3	96
Figure 6. 26	Recording of acceleration (Ch3) in a movement (15 mm, 12 Hz) on beam 2 ..	96
Figure 6. 27	Display of acceleration (Ch3) in the frequency domain	97
Figure 6. 28	Display of accelerations of (a) Ch1 and (b) Ch2 in the frequency domain	97
Figure 8. 1	Physical design of SHM system components on a rotor blade	113

List of Tables

Table 2. 1	Specifications of the carbon fiber fabric.....	16
Table 2. 2	Specifications of the carbon fiber	16
Table 2. 3	Specifications of the Nomex honeycomb sheet	19
Table 4. 1	Summary of calculation results for beam 1	44
Table 4. 2	Summary of calculation results for beam 2	45
Table 4. 3	Summary of calculation results for beam 3	46
Table 4. 4	Collection of stiffness test results	47
Table 5. 1	Summary of static tests for beam 1	54
Table 5. 2	Comparison of bending strain between theoretical values and measurements	70
Table 6. 1	Conclusion of six movement ranges in dynamic tests	81

List of Symbols and Acronyms

Symbols

b	Specimen width
c	Thickness of honeycomb core
d	Midpoint displacement
h	Specimen height
k	Bending stiffness
l	Distance to the specimen tip
n	Index of refraction
s	Side length of honeycomb cell
t	Thickness of CFRP material
t_c	Thickness of honeycomb cell wall
A_c	Cross-sectional area of honeycomb core
A_s	Cross-sectional area of CFRP skin
A_w	Cross-sectional area of CFRP side wall
E	Flexural modulus
$(EI)_{eq}$	Equivalent flexural rigidity

E_f	Flexural modulus of CFRP material
F	Force
F_f	Force on CFRP side walls
G	In-plane shear modulus
G_l	In-plane shear modulus
G_o	Out-of-plane shear modulus
I	Moment of inertia about bending axis
L	Effective length
Z	Section modulus
γ_c	Shear strain on honeycomb core
γ_f	Shear strain on CFRP side wall
Δ	Specimen tip displacement
\mathcal{E}	Bending stress
Λ	Period of index of refraction variation
λ	Central wavelength
σ	Bending strain
τ_c	Shear stress on honeycomb core
τ_f	Shear stress on CFRP side wall

Acronyms

CFRP	Carbon Fiber Reinforced Plastic
FBG	Fiber Bragg Gratings
FFT	Fast Fourier Transform
GFRP	Glass Fiber Reinforced Plastic
GND	Ground
HUMS	Health and Usage Monitoring
IEEE	Institute of Electrical and Electronic Engineers
MEMS	Micro-electromechanical Systems
NACA	National Advisory Committee for Aeronautics
NDT	Non-Destructive Testing
NI	National Instruments
PC	Personal Computer
PCB	Printed Circuit Board
RPM	Revolutions per minute
RTB	Rotor Track and Balance
SG	Strain Gauge
SHM	Structural Health Monitoring
TDM	Time division multiplexing
UD	Uni-directional
WDM	Wavelength division multiplexing

WPAN	Wireless personal area networks
-------------	---------------------------------

WSN	Wireless Sensor Network
------------	-------------------------

Chapter 1

Introduction

1.1 Background

1.1.1 Structural health monitoring

The state of a structure is designed to remain in a specified domain during its life time, but factors such as usage aging, environmental action and accident of damage may bring some uncertainties in achieving this goal. Structural health monitoring (SHM) is a process of detecting the health state of part or of a whole structure and offering a diagnosis based on history data (1). Applications of SHM in aeronautic and civil domains have emerged in the last 30 years.

In order to achieve the diagnosis function, the concept of SHM involves the possibility of integration of sensors or smart materials, data transmission, acquisition and processing. Furthermore, a SHM system would normally be introduced early in the design phase and would be considered to function during the whole life time of the structure.

1.1.2 SHM on helicopter rotor system

A helicopter is able to take off and land vertically, to hover, and to fly forward and backward. Because of such operating characteristics, helicopters are applied in a wide range of missions such as transportation, military, firefighting, medical service, search and rescue, including some tasks which are impossible for fixed-wing aircraft. The function of the rotor blades of a helicopter is mainly to provide lift, propulsion and control forces, but the helicopter rotor system itself operates in a highly dynamic and unsteady aerodynamic environment. In forward flight, for instance, the effect of an asymmetric loading condition of the flexible rotating blades usually leads to severe vibratory loads.

Even though the rotor system is the principal vibration source in a helicopter, in a strict sense, there is almost no practical SHM system available to directly monitor the health state of main rotor blades (2). Accurate rotor blade monitoring is also excluded from existing monitoring systems whose functions overlap with that of SHM. The main reasons for this awkward situation are the positioning, communicating, and powering issues of sensors on rotor blades during operation. As a consequence, information from lag measurements conducted by optical trackers and vibration measurements specific to the swashplate bearing are processed to support a health state diagnosis of rotor blades.

The most common existing monitoring system on helicopters, a health and usage monitoring system (HUMS), has been established as comprehensive, capable of detecting fault in driven train, engines, oil system, and rotor track and balance (RTB) system. They are currently instrumented on several helicopters such as Sikorsky SH-60B Seahawk, UH-60A Black Hawk, and AH-64D Apache (3).

As an essential part of HUMS, usage monitoring performs an assessment of the residual life of critical structures by detecting the damage exposure. Specifically, this module can register the in-flight threshold exceeding events and corresponding flight parameters such as altitude, airspeed, and temperature when the excess occurs. Another critical part of HUMS is vibration monitoring, in which the vibration signatures are analyzed, and subsequently used as damage indicators or for fault diagnosing. At present, vibration monitoring is normally employed for detecting bearing wear, gear cracks, drive shaft unbalance, and shaft cracks.

A Eurocopter HUMS program involving more than 1000 flight hours concluded that the implementation of HUMS leads to great safety improvement by avoiding structural and systematic failures (4). Another report of the HUMS application on 100 CH-146 Griffin helicopters also mentioned some distinct benefits: the function of fault isolation and prognostics contribute to maintenance directives and life prediction respectively. In spite of various advantages of HUMS, its applicability and reliability on some components such as rotor blades still needs further improvements (5).

1.2 Objective and motivation

1.2.1 Goal

Helicopter rotor blades are recognized as critical structural components that are subjected to severe load and vibration during flight. Loads and vibration, along with other parameters, can be effective health and usage indicators. However, accurate monitoring of rotor blades is limited by the practical restrictions. This thesis establishes a SHM system for helicopter rotor blades on the basis of a wireless sensor network. By measuring and analyzing operational parameters such as vibration, acceleration, strain, load, and temperature, the rotor blade performance can be characterized and damage can be identified.

1.2.2 Motivation

A SHM system offers a knowledge of the structural integrity on a continuous real-time basis. Such immediate information and a full history database containing all the registered data are greatly beneficial for manufacturers, operators and maintainers.

Specifically, SHM helps manufacturers to reconsider the design of the structure and to improve the production process, contributes to an optimal usage with a minimized downtime and reduction in accidents, and allows less maintenance labor and time by drastically changing maintenance services into the condition-based mode and minimizing human involvement. As critical structural components, rotor blades are certainly attractive targets for SHM.

The main objective of developing SHM systems for rotor blades is to improve flight safety. It is shown in a recent report that approximate 3% of civil helicopter accidents were caused by rotor system failure (6). Even though this number does not seem very astonishing, rotor system failure is recognized as one of the most significant accident factors. Considering the structural aging and degradation resulting from environmental factors, updated information from SHM is needed to determine the rotor blade performance and, thus, to establish subsequent programs (7). With regard to operational safety, SHM also allows a rapid screening to re-evaluate the health state of rotor blades, in particular after some spectacular accidents. Additionally, in conjunction with a rational design and accurate production, SHM is capable of detecting the critical load condition and even reducing such loads by using an active feedback upon the rotor system.

Out of economic considerations, there also has been a growing interest in the introduction of SHM to some critical structures of a helicopter such as the rotor system. Directly or indirectly, the economic impact of SHM involvement can be reflected in an increment of mission and equipment reliability, extended life of components, less test flights, reduction in downtime, more flexibility of condition-based maintenance, and better pilot awareness of flight limits. It is reported that, for a helicopter, the maintenance cost takes up approximately 24% of the direct operating cost (8). Therefore, the economic impact of SHM could be considerable via damage growth prediction and the optimization of maintenance actions (9). Furthermore, fabrication cost of SHM system can be largely reduced by taking the existing flight data recorder as a basis. In general, a SHM system integrated in the helicopter rotor system contributes to safety improvement and cost saving.

The slip ring mechanism connects the wiring between a rotating part and a non-rotating part without tangling or interfering with each other. In principle, inside a slip ring, a continuous electrical connection is ensured by a series of sliding brushes and the conductive housing. However, the weight of the slip ring assembly could become a problem with an increasing number of sensors. In addition, distributed wired sensors or fiber optic sensors require a great amount of power for data acquisition. Even though some recently developed technologies such as miniaturization, energy harvesting and local data processing somewhat contribute to the data and wiring reduction, the basic data transmission mode keeps same, especially from the rotor system to the fuselage. Due to such difficulties in the communication with rotating frames, the rotor blades of some civil helicopters remain unmonitored (10).

In contrast to wired sensing, wireless sensor networks (WSNs) can be employed in a complex environment like the one in which the rotor blades are working. This means SHM based on WSNs makes it possible to provide a solution when the wire-based method is limited by practical restrictions on wiring between the rotor system and helicopter body. Other motivations including optimized maintenance, cost saving, and weight reduction also strongly lead to the use of WSNs for real time SHM. Thanks to very little physical intervention, wireless sensors can be replaced with ease and even a whole sensor network can be reorganized during a short on-ground maintenance. Since the data transmission is realized upon a wireless network, the cost of installation and maintenance is significantly lower without involvement of wiring and conduits. As mentioned above, the slip ring becomes a cumbersome part on the main rotor hub when an increasing number of sensors are incorporated in the wire-based network. The reduction in weight achieved by replacing wiring and wire-based connections with wireless data transmission path is certainly attractive to the designer of a helicopter.

1.2.3 Thesis question

The key scientific question addressed in the thesis is how to configure a SHM system based on WSNs. In order to answer this question, work in three aspects is included this thesis. First, the sensor positioning and organization of components is designed and optimized. Second, the data transmission quality is evaluated and phenomena such as signal attenuation and electromagnetic interference are analyzed. Third, several operation parameters are measured and damage-sensitive indicators are identified from these potential candidates.

1.3 Outline

1.3.1 Scope of work

In the thesis work, one rotor blade instead of the whole rotor system is targeted for the laboratory SHM system due to the extreme complexity of experimental model of the complete rotor system. In addition, performing measurements on rotor blades rather than on the rotor hub has always been a significant objective when a SHM system is established. Specimens of single rotor blade were designed and manufactured for subsequent tests of SHM functionality, in which the connection with the rotor hub can be simulated with mechanical structures.

During the experimental phase, static and dynamic tests were carried out to evaluate the applicability of wireless SHM system. A rotor blade operates in an aerodynamic environment, which reacts upon the blade with severe dynamic loads. Attributed to these loads, a rotor blade is subject to flapping, lead-lag motion, and torsion. Among them, flapping has been recognized as the most interesting movement because it is highly related to lift force, which is critical for either the rotor system or the whole helicopter. Therefore, flapping movement is of primary concern when the operation condition is reproduced.

Aiming at analyzing the influence of defects, a comparison is carried out between the defected

specimen and the non-defected specimen. Based on these test results, damage-sensitive indicators can be identified and the effective type or location of sensors in SHM can be determined. Along with the evaluation outcomes of wireless data transmission in SHM, the system structure is then optimized and can be utilized as a basis of the practical SHM applications on rotor blades.

1.3.2 Outline

There are 8 chapters in this thesis, starting from introducing general information of the SHM on helicopters, particularly on the rotor system in this chapter. It has been shown that the attempt to establish a SHM system of rotor blades based on WSNs is motivated by some strong reasons. In addition, the objective and basic thoughts of methodology in this thesis is pinpointed specifically. In the next chapter, theories of composite rotor blade structure, the design and manufacture of the specimens simplified from the R22 rotor blades, and the design of an artificial defect are included. Subsequently, measurement and monitoring hardware including strain gauges, components of a WSN, and other devices are described in detail in chapter 3.

In the following chapters 4 and 5, experimental setup, scheme, results and analysis of stiffness tests, static tests, and slow dynamic tests are covered. The latter two groups of tests are included in chapter 5 since they applied an identical experimental setup. Chapter 6 introduces the experimental setup, scheme of dynamic tests, which was performed to simulate the rotor blade flapping, and present the results obtained from the WSN. These three chapters are experimental chapters, followed by chapter 7 carrying out a discussion based on the measurement results in aspects of the specimens, the WSN, dynamic effects, influence of the defect, noise issue.

In the last chapter, work of this thesis is concluded, significant experimental results are highlighted, limitations are pointed out, and the work for future research is recommended. In addition, a primary design of a SHM system based on a WSN for composite helicopter rotor blades is proposed.

1.4 References

2. Balageas, Daniel, Claus-Peter Fritzen, and Alfredo Güemes, eds. Structural health monitoring. Vol. 493. London: ISTE, 2006.
3. Sanchez Ramirez A, Das K, Loendersloot R, et al. Wireless sensor network for helicopter rotor blade vibration monitoring: Requirements definition and technological aspects. Key Engineering Materials. 2013, 569: 775-782.
4. Pawar PM, Ganguli R. Helicopter rotor health monitoring- a review. Proceedings of the Institution of Mechanical Engineers, Part G: Journal of Aerospace Engineering. 2007 May 1, 2007;221(5):631-47.
5. Pouradier J. TM, editor An assessment of Eurocopter experience in HUMS development and support. In Proceedings of 57th Annual Forum of the American Helicopter Society; 2001; Alexandria,VA,USA.
6. M.J. A, editor Achieving HUMS benefits in the military environment-HUMS developments on the CH-146 Griffon fleet. In Proceedings of 60th Annual Forum of the American Helicopter Society; 2004; Baltimore,Maryland,USA.
7. Iseler L, De Maio J. An analysis of US civil rotorcraft accidents by cost and injury (1990-1996). DTIC Document, 2002.
8. Ikegami R, Haugse ED, editors. Structural health management for aging aircraft. SPIE's 8th Annual International Symposium on Smart Structures and Materials; 2001; Proc. SPIE.
9. Cronkhite JD, editor Practical application of health and usage monitoring (HUMS) to helicopter rotor, engine and drive system. In Proceedings of 49th Annual Forum of the American Helicopter Society; 1993; St Louis,MO,USA.
10. Chang F-K, editor Design of integrated SHM system for commercial aircraft applications. CHANG F K 5th International Workshop on Structural Health Monitoring Stanford: Stanford University Press; 2005.
11. Moore-navair N-MD. Energy Harvesting, Wireless Structural Health Monitoring System for Helicopter Rotors. 2013.

Chapter 2

Composite Specimen

2.1 Theory

2.1.1 Composite rotor blade

The design and manufacture of helicopter rotor blades has been greatly developed and refined recently with an increasing knowledge of materials and aerodynamics. One important factor contributing to this advancement is the introduction of composite materials (1). Thanks to their versatility and desirable properties, composite materials can be found in numerous parts of a helicopter, such as seats, the engine bay door, fuselage, tail, etc. Among these, rotor blades significantly benefit in performance and service-life from the use of composite materials (2).

Helicopter rotor blades were originally constructed of laminated wood and fabric. Then steel and aluminium structures were introduced in 1960s. Although they brought a great improvement on predefined designs and achieved cheapness and ease of manufacture, critical problems such as mass alteration due to moisture absorption, poor fatigue resistance, and low strength-to-density ratios made metal rotor blades gradually become unfavorable and they were replaced by composite blades.

Radical advancements in rotor blade design and performance were allowed by the composite materials and structures. For instance, glass fiber reinforced plastic (GFRP) consists of glass fibers dispersed within a polymeric matrix, which together determine the mechanical properties and characteristics (3). The matrix mainly functions to bind fibers, convey and to distribute external stresses in the whole material to prevent crack propagation between fibers. The fibers possess significantly greater strength than the bulk materials and are commercially available at low price since they are produced by means of drawing. The strength and chemical inertness of fibers allow their desirable applications in rotor blades.

Another popular composite material for rotor blades is carbon fiber reinforced plastic (CFRP),

which overcomes the lack of stiffness occurring in GFRP. Fibers of CFRP are manufactured from polyacrylonitrile, pitch and rayon, hence CFRPs possess the highest specific modulus of all fiber reinforced materials (4). More specifically, carbon fibers have a tensile strength of the order of 2400 N/mm^2 and an elastic modulus of 400 kN/mm^2 . Due to such high modulus, it is estimated that a 12% weight saving can be made by replacing 40% of aluminum alloy structures (5). Sheets of these fiber reinforced materials can be sandwiched together alternately at certain angles in order to display desired properties in specific directions and areas, matching those of the major loads.

However, CFRP is subjected to some disadvantages: CFRP does not yield plastically in the case of stress concentrations; its strength is sensitive to impact damage; and the properties of CFRP suffer from more random variations than those of metals. Therefore, all these factors need to be taken into account in the design phase.

In general, composite materials such as CFRPs offer a number of advantages over metals, which include lightness, fatigue resistance, better strength, etc (6). The strength-to-density ratios of composite materials may be four to six times greater than those of metals. The greater specific modulus of composite materials leads to composite blades that are up to 45% lighter than their equivalents. In the specific case of helicopter rotor blades, better fatigue resistance leads to expanded service life by using CFRP in the fabrication. Another additional advantage lies in substantial aerodynamic improvements since the molding techniques employed for composite structure manufacture allow variations of cross-section along the span. A typical example can be found on the main rotor blades of the GKN Westland Helicopter EH101 (5). Moreover, for composite rotor blades with complex shapes, their assembly processes can be significantly simplified by adhesive joining instead of riveting.

2.1.2 Manufacture

Rotor blades are subjected to extremely harsh conditions, both operational and environmental, such as flapping during flight, rotational tip velocities of approximately 200 m/s, extremes in humidity, and temperature variation from -40°C to 50°C (7). So the composite materials employed are designed and manufactured to fulfill various specific material properties required for effective rotor blades.

The manufacture of composite rotor blades sometimes begins with the ultrasonic profiling of pre-pregs, which are partially cured fiber reinforced plastics. This profiling technique allows the introduction of advanced shaped blades that are virtually impossible to be fabricated economically from metals. The second step is to position the contoured pre-pregs with a predefined lay-up pattern in a mould. The material is crushed into the desired shape by an external hydraulic pressure (8). A computer-controlled process is employed in the curing stage to maintain the pressure applied and to increase the temperature at certain rates. Lastly, adhesive bonding of the honeycomb between two blade layers is implemented to finish the blade construction.

2.1.3 Defects

Helicopter rotor blades exhibit a wide variety of failure modes, which are different not only in locations of the rotor blade, but also in progress rates and effects. For instance, significant vibration levels may be caused by aerodynamic imbalance during operation. Some local cracks such as superficial cracks are possible to develop into structural cracks and even threaten the entire rotor blade. These failure modes can be classified into groups of overall defects and local defects. Aerodynamic imbalance, mass imbalance and wrong pitch control are included in the former while the latter covers the damages in much smaller scale such as cracks, matrix degradation, delamination, etc. (9).

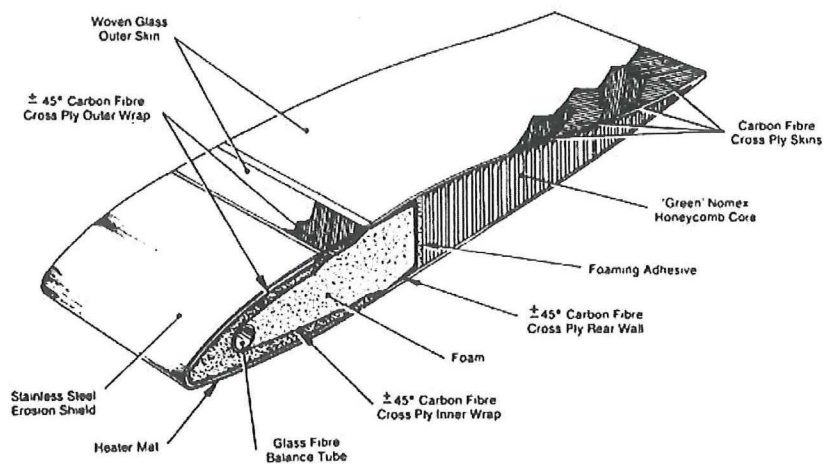


Figure 2.1 Sectional view of a composite Sea King helicopter rotor blade (5)

As shown in figure 2.1, a Sea King helicopter rotor blade is structurally complex, incorporating CFRP, GFRP, stainless steel, a honeycomb core, and foam filling. The foam filled section is responsible for impact resistance and the main body of a composite rotor blade is a sandwich structure, which is composed of a honeycomb core and facing materials. Therefore, common or critical defects in foam and honeycomb sandwich structures of rotor blades need to be considered.

Defects in a sandwich composite structure of rotor blades can be external or internal. Most external defects such as dimensional errors, finish defects and warpage are visually inspectable. On the other hand, internal defects in composites such as delaminations, inclusions, voids, resin-rich and starved areas, fiber misalignments and breakage require NDT techniques to detect damage (10). Composite rotor blades are susceptible to low velocity impact damage and progressive damage accumulation, which is often caused by vibratory loads. Defects such as matrix cracking, debonding, delamination and fiber breakage are strongly related to the damage accumulation (11).

The internal defects of importance, and also frequently observed, are cavities, holes, and cracks in the sealing elements on the interface of the honeycomb core and the border sections. Water may penetrate into these locations and probably damage the surrounding materials after freezing

by the volume expansion of ice. The relatively complex arrangement of composite structures could bring some difficulty to detect such defects. It appears to be less dangerous when the defects are at the border sections. In such situation, water settles in the stiffener cave, which is depicted in figure 2.2, and easily flows out from the crack through the vent gap of the stiffener when the blade is in an operational position (10). But in the other case, severe damages can be caused by water penetrating into the honeycomb core through the adhesive sealing elements.

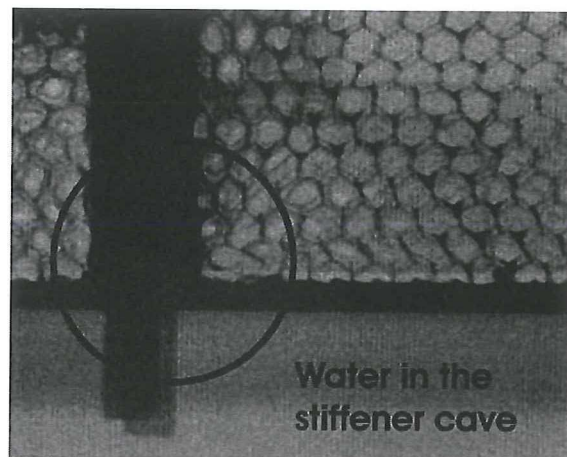


Figure 2. 2 Water percolates between two borders near the stiffener (10)

Considering the sandwich structure that is used for strength members in dynamically loaded rotor blades, debonding or delamination between the center core and outer facings is also a concern. Such defects at critical locations can have a significant impact on loading paths, resulting in a reduction in structural strength. The buckling and collapse strength of the sandwich structure can also be seriously affected since the core structure and facings are partially separated during bending (12). In addition, the combination of cracks introduced by debonding or delamination and the dynamic load leads to a crucial fatigue problem.

Inhomogeneities of the resin materials (resin-rich or starved areas) at the facings are recognized as one common defect type. Fortunately, this type of defect can be detected by using hydrogen containing materials with a high neutron attenuation coefficient (10). For a military helicopter, damages of rotor blades are also possibly from the defects generated during gunnery practice. Although such defects will be mended right after the practice, some small splinters may not be detected and these will thus remain in the blade as inclusions. Other common blade defects include debonds in the adhesive surface between the honeycomb structure and the aluminium spar, corrosion inside the rotor blade tail elements, fiber breakages of tailing edge, and the slicing of the honeycomb structure near to the stiffener.

It can be concluded that the most significant defect of sandwich structure in a composite rotor blade is debonding or delamination between the honeycomb core and facing materials. This defect can be dangerous to blade structural health, especially when it exists near border sections. In such situation, both strength loss and water penetration are involved and can cause severe accidents. Therefore, the applicability of a structural health monitoring (SHM) system to detect these types of defect needs to be evaluated with priority before the establishment of SHM systems on real rotor blades.

2.2 Design

2.2.1 R22

The Robinson R22 helicopter is targeted as a reference helicopter in the design phase, from which an experimental model of a simplified light helicopter rotor blade will be designed. The R22 is a typical example of a civil light helicopter and is popular all over the world. Such a worldwide rich operating experience provides a comprehensive knowledge of R22 operational and environmental conditions. Due to its civil applications, the flight operations and maintenance actions have been developed to be highly standardized. This benefits the model study by reducing uncertainty in the model design. Furthermore, a relatively simple structural design of rotor system is carried by the R22 due to the weight restriction imposed on light helicopters. Therefore, more attention can be paid on the SHM system setup rather than structural investigation. Certainly, the small size of a R22's rotor blade is another critical consideration to select it as the prototype and also makes future work on full scale testing more feasible.

The Robinson R22 is a two seater, light utility helicopter powered by a four-cylinder Textron Lycoming O-360 reciprocating engine. Its reliability, low maintenance, and low operating costs make it ideal for a variety of applications and make it one of most popular light helicopters in market. It has a 145 hp Lycoming O-360 engine, a lightweight steel tube airframe, and aerodynamic shape. The R22 has a cruise speed of up to 96 kts (110 mph) and an average fuel consumption of 7-10 gallons per hour. The applications of R22 ranges from flight training to livestock mustering and patrolling pipelines that require dependability, low operating cost, and performance (13).



Figure 2.3 Robinson R22 (13)

While sharing some common design features with general helicopters, the R22 possesses several innovative and unique designs. For instance, the main rotor system of a R22 utilizes a two-blade, rigid-in-plane design. The rotor blades are connected to the main rotor hub through individual flapping hinges, which are part of a teetering main rotor hub that is hinged to the main rotor

mast. In most general two-bladed semi-rigid systems, the advancing blade flaps up, causing the retreating blade to flap down. However, the R22 main rotor blades are individually hinge-pinned and therefore can flap independently relative to each other. Such flexibility makes it possible to have an effective coning operation, in which two blades both move up until centrifugal force balances lift (14).

Additionally, its tri-hinge main rotor hub eliminates lag hinges, dampers, and hydraulic struts; blades have a stainless steel spar at the leading edge which resists erosion; and droop stops prevent excessive main rotor teetering while stopping or starting under normal operating conditions (15).

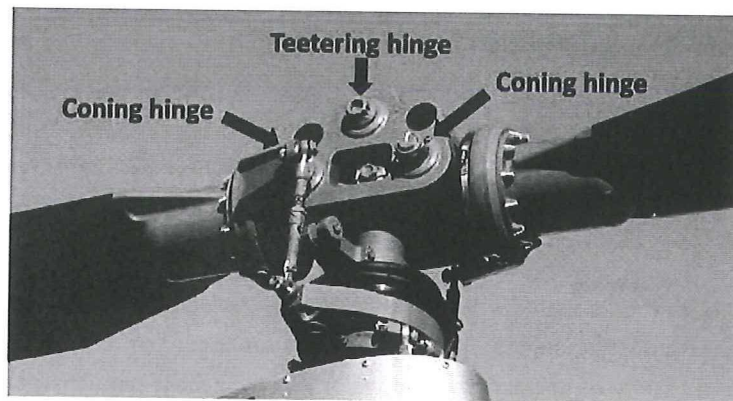


Figure 2. 4 Rotor hub of the R22 (16)

2.2.2 R22 rotor blade

The total diameter of the R22 main rotor disc (two opposite blades connected by the hub) measures 25 feet, 2 inches, and each blade weighs approximately 26 pounds. The R22 uses main rotor blades designed according to National Advisory Committee for Aeronautics (NACA) 63-015 airfoil specifications. The R22 main rotor blades are constructed at the Robinson helicopter company's manufacturing facility with a 7.2-inch chord (width of blade) and are each 12.58 feet long (15).

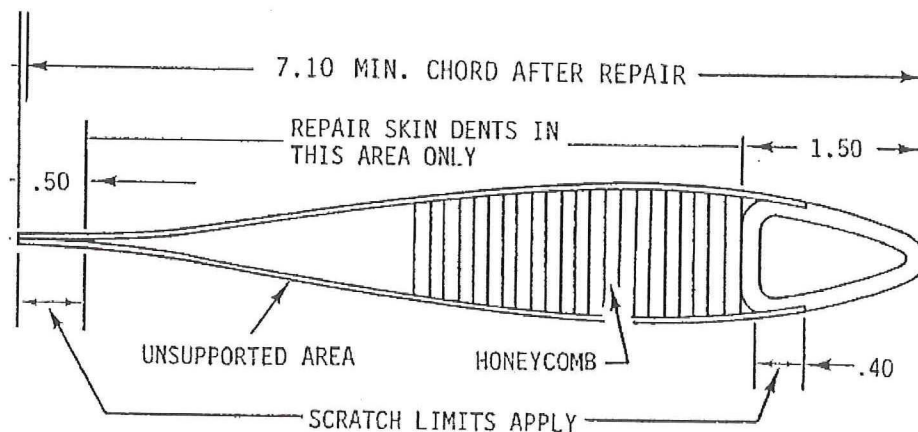


Figure 2. 5 Cross section of R22 rotor blade (17)

It can be seen in figure 2.5 that the R22 main rotor blade is of conventional bonded metal construction, comprising top and bottom skins of aluminium alloy with an aluminium honeycomb core, a hollow 'D' section leading edge spar of stainless steel, and a forged aluminum alloy root-fitting. All dimensions labeled in the figure are in inch. The root fitting includes a short stub section which is bonded inside the blade, and two fingers which extend into the blade. The larger finger is fixed to the rear face of the hollow spar by a combination of adhesive bonding and a series of bolts which engage a strip of captive nuts located inside the spar. The smaller finger at the trailing edge of the root fitting is bonded directly to the skins. Aluminium alloy doublers are bonded externally to the skins in order to provide local stiffening and reinforcement of the skins near their connection to the root fitting. Moreover, an aluminium alloy cap is bonded to cover the end of the hollow spar, and is blended into the root fitting by an adhesive fillet (18).

2.2.3 Specimen design

2.2.3.1 Structure

A rotor blade of the R22 helicopter is introduced as a reference for designing the experimental models. However it is intended to construct the model with composite materials instead of aluminum, as employed by the R22 rotor blade. In order to deal with such a difference in material options, some design attempts and replacement strategies are needed.

In a general composite rotor blade, the hollow stainless steel spar is replaced by a relatively complex composite structure consisting of stainless steel erosion shield, heater mat, carbon fiber cross ply wrap, foam, and carbon fiber cross ply rear wall. These components play different roles during operation: the shield prevents erosion; the outer and inner carbon fiber wrap keeps the aerodynamic shape while separating different materials; the heater mat is arranged for heat insulation; foam filling inside the structure can improve the impact resistance; and the rear wall functions not only as a conventional spar but also as a border between the forward section and the honeycomb structure. Since the factors of impact damage, thermal damage, and erosion damage are not taken into account in this thesis, the whole forward section can be simplified to a CFRP wall, which remains as a strength member.

In addition, for a R22 rotor blade, the length of the hollow spar part takes up only 21% of the chord. Therefore, the rear section, with the honeycomb structure as the core, should become the main consideration when designing the model. The rear part of the R22 rotor blade is constituted of top and bottom skins of aluminium alloy, and an aluminium honeycomb core. For the same reason that a composite solution is called for to conform to the trend of composite applications in rotor blades, the top and bottom skins are designed to be CFRP, with a Nomex honeycomb core sandwiched between them. A Nomex honeycomb is made from aramid fiber paper and is coated with a high modulus phenolic resin.

According to the structure of a common composite rotor blade, there is an additional layer of woven glass skin placed outside the carbon fiber skin. However, it is excluded in the simplified model as it mainly contributes to surface smoothness and protection. Due to the fact that shaping the honeycomb core into an aerodynamic profile is difficult for the existing machines in

the lab, a significant modification of the structure shape needs to be made. Even though some effects on strength and stiffness can be carried, the cross-section of honeycomb structure is simplified to a rectangular shape. In order to close the honeycomb core in the trailing edge, an additional carbon fiber side wall is introduced.

To sum up, an experimental model simplified from a helicopter rotor blade is designed as a composite beam with a rectangular cross-section. The beam is fabricated by sandwiching two layers of CFRP skins with a Nomex honeycomb core and closing up the structure by using front and rear CFRP walls.

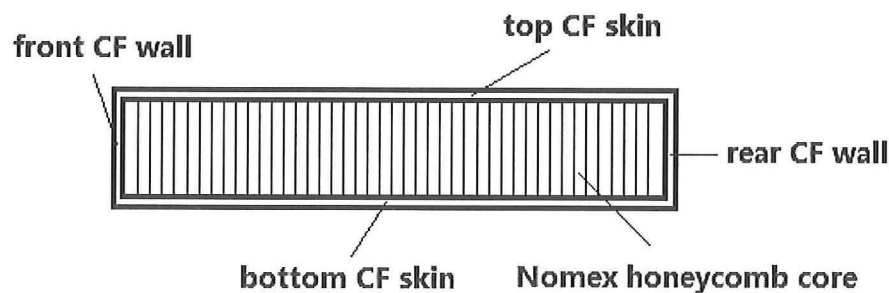


Figure 2.6 Sectional view of experimental model

2.2.3.2 Dimension

The model dimension is determined based on the real size of R22 rotor blades. The R22 rotor blade is 12.58 feet (3.83 m) long with a 7.2 inch (18.29 cm) chord. In the cross-section of the rotor blade, the front section excluded in the design is 1.5 inch long. But part of it (0.5 inch) is covered by skins, which are integrated in the sandwich structure. Hence, the length representing the front section that needs to be deducted is 1 inch, which means the sandwich part is approximately 6.2 inch (15.75 cm) long. The maximum thickness is 15% of the chord for NACA 63-015 airfoil. So the maximum thickness is about 1.08 inch (2.74 cm) and this value will be used as the overall height of sandwich structure. Using maximum thickness instead of average thickness is for partially makes up the strength loss from the design simplification, especially when the spar structure is replaced by a carbon fiber wall.

Given the physical restrictions imposed by the fabrication and test facilities, a scaled-down version of the model is required. The length of the model, a composite beam, is the most critical dimension and a value of 1.2 m is considered suitable, which is within the various limits and ensures other dimensions not too small after scaling down. The dimensions of the experimental model are obtained after scaling down with a factor of 3.2: a length of 1.2 m; a width of 4.92 cm; a height of 0.86 cm. For convenience, the composite beam in the final design is determined to be 1.2 m long, 5 cm wide and 1 cm height (matching with the thickness of commercial core material in the market) and ignoring the thickness of CFRP skin in the design phase.

2.2.3.3 Skins and walls

The skin thickness is about 0.5 mm after scaling down with same factor of 3.2 as the other dimensions. Because a single layer thickness of carbon fiber fabric is 0.42 mm and a little larger thickness may be obtained after resin infusion, only one layer of fabric is laid up for making CFRP plates. In the original design of the R22 rotor blades, multiple layers with $\pm 45^\circ$ orientations are involved in the skin part. Considering that the most critical load for rotor blade is flap bending moment, the orientation of the only carbon fiber fabric is designed along the blade span. In order to avoid introducing extra structural influence from walls, the thickness of walls is set the same as that of skins, by using one layer of fabric as well.

2.2.3.4 Defect

As concluded in section 2.1.3, debonding or delamination between skins and the honeycomb core is one of critical defects for rotor blades since such defect can cause strength loss, along with a large risk of water penetration into honeycomb structure. In recognition of this fact, the defected specimen is designed with a 25cm long debonding between bottom skin and the core located 30cm from root, which can be realized by not applying adhesive films on the chosen area during fabrication.

2.3 Manufacture

The specimens are fabricated in the Structures and Materials Laboratory, TUDelft, where commonly used equipment for composite product manufacturing is available. According to the specimen design described in section 2.2.3, the specimen consists of a honeycomb core, two CFRP skins, and two CFRP walls. A Nomex honeycomb sheet is provided directly, so preparation work of the honeycomb core is mainly to cut and trim it in accurate size. On the other hand, CFRP skins or walls can be cut out from one large CFRP plate, which is fabricated in advance. This approach is convenient and benefits in ensuring consistency of the CFRP members' properties. Therefore, the first step is to fabricate a CFRP plate in large size.

When all structural members are prepared, the specimen can be constructed by bonding them together. There are two common solutions for bonding different composite materials: co-curing and adhesive film bonding. Because the honeycomb core is made of thin foils in a form of hexagonal cells, fluid resin cannot be employed otherwise the resin would flow into the honeycomb structure through the hollow channel and cause weight problems. For the same reason, the CFRP skins and walls need to be completely cured before attaching to the core. Therefore, the latter solution is applied. Adhesive films are placed between skins (walls) and the core to provide a permanent structural bonding, which is able to withstand harsh environments.

After taking factors such as product quality, efficiency, and feasibility into account, a fabrication process, which comprises two main steps: CFRP plate fabrication and adhesive bonding, is established.

2.3.1 CFRP plate fabrication

The fabrication of CFRP plate was implemented by means of vacuum infusion, in which a vacuum pump, a mold and a vacuum bag are involved. In the vacuum infusion approach, there are 6 steps needing to be accomplished in order to obtain a CFRP plate with high quality.

2.3.1.1 Preparation of carbon fiber fabric

One piece of carbon fiber fabric with an area of 1.21 m by 30 cm was cut out with a knife. Specifications of the carbon fiber fabric and its fiber are shown in table 2.1 and table 2.2 respectively. (Note: wearing gloves is required to avoid contaminating the fabric and skin discomfort.)

Product	Manufacturer	Weight per area	Width	Fiber type	Thickness
Udo UD CS 300/300	SGL Group	300 g/m ²	300 mm	STS40 F13 24K 1600tex	0.42 mm

Table 2. 1 Specifications of the carbon fiber fabric

Product	Number of filaments	Linear density	Density	Tensile strength	Tensile modulus
STS40 F13 24K 1600tex	24000	1600 tex	1.77 g/cm ³	4000MPa	240GPa

Table 2. 2 Specifications of the carbon fiber

2.3.1.2 Mold cleaning

First, a flat aluminum mold was cleaned with ethanol. Then, sequential actions including rubbing, cleaning and tape covering were taken in treatment of mold edge. The third step was to coat the mold with the release agent for five times with 10min intervals. After the last time of coating, the tapes on edges were torn off. (Note: coating directions should be different between two adjacent coatings in order to ensure that the whole area is covered by the release agent, which largely contributes to later mold removal.)

2.3.1.3. Placement

This step began with tightly pasting gum tapes on the mold edges. Secondly, the carbon fiber fabric, a piece of flow mesh, and a piece of flow mesh were laid up in order and they were

positioned by taping. Then the outlet path was arranged by placing bleeders next to one fabric edge. Thirdly, small pieces of gum tapes were used around the inlet and outlet pipes as sealants and also to attach pipes to the gum tapes on the edges. Fourthly, a plastic spiral was placed along one edge of the flow mesh by using several pieces of gum tape. This spiral can function as a resin feed line, aiding resin flow in the subsequent infusion process. Lastly, the vacuum bag was placed above the whole setup and four edges were sealed. A picture of final placement version is shown in figure 2.7.

Some gum tape loops were used to deal with extra lengths of bag edges, to ensure a flat bag surface above the fabric. In order to prevent the vacuum bag from rupturing, sharp points of the spiral and pipes were covered by gum tapes. The peel ply should be large enough to cover the whole fabric, so the mesh flow can be easily removed from the CFRP plate after curing. But its size should not be too large since remains of the extra part may stick to the mold and bring additional cleaning work. Such size compromise is important for flow mesh as well. Some spaces should be left between mesh edges and fabric edges to allow resin to flow down through the whole thickness of the fabric before reaching its edges. But this space needs to be small enough otherwise it takes too much time for the resin flow to reach the edges or even that the resin cannot reach them before curing. This space was finally determined depending on experience gained in trial-manufacture. It is also worth to note that the fabric should be laid up with the wired side down. Unfavorable resin channels can be formed along wiring and it is possible for air to be trapped by the resin flow passing by, remaining as small dry spots.

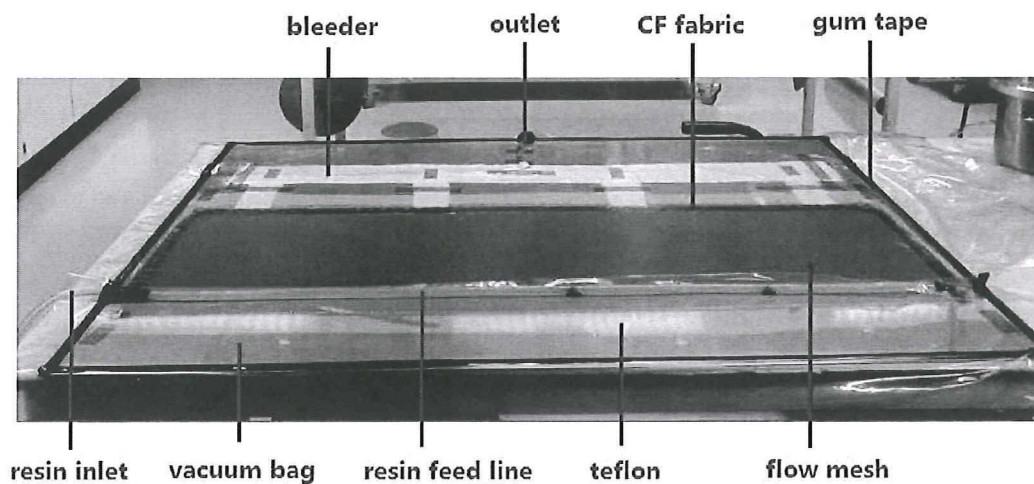


Figure 2. 7 Placement for resin infusion

2.3.1.4. Vacuum connection

Actions were taken in this step to establish a good vacuum condition. Firstly, the outlet pipe was connected with a vacuum can whose other vent hole is connected to a vacuum pump. Secondly, the inlet pipe was clamped and the vacuum pump was turned on. After the air inside the vacuum bag was removed, the vacuum condition was checked by reading a vacuum gauge on the pump. When the reading was stable without becoming larger, a good vacuum condition was ensured.

Potential leakages can be dealt with by means of pressing the gum tapes on edges. When a good sealing was confirmed, the vacuum pump was adjusted to provide a vacuum of 50 mbar to prepare for the infusion process.

(Note: a good sealing is the most critical condition for a successful resin infusion process. In order to achieve that, the inlet pipe needs to be clamped tightly and no detectable leakage is allowed. Vacuum functions as a driver of resin flowing and to prevent the air into CFRP plate as well. So a steady vacuum condition during infusion and curing processes is necessary to allow a satisfactory product.)

2.3.1.5. Resin preparation

The resin preparation started by mixing epoxy resin with hardener with a ratio of 10:3 in a bucket in a fume hood. The mixture was stirred by a wooden stick till it became uniform. The second action was to place a piece of bleeder in the bucket and make sure it was completely immersed into the resin mixture. Then the bucket was sent into an aspirator for degassing for at least half hour. A vacuum about 2 mbar was applied during the degassing process. Once the degassing was finished, the end of the inlet pipe was inserted and fixed in the mixture.

(Note: there are two things in this step needing extra attention. First, the amount of resin mixture consumed in the infusion process needs to be estimated in advance. Basing on previous experimental experience, 0.5 g of mixture is required for 1 cm³ of fabric. Apart from the resin infused into the fabric, a great amount of resin mixture can remain in the inlet pipe, the spiral, and the mesh flow. So the total amount of resin mixture needed for infusion highly depends on the placement and dimensions of each component. As an example, a 910 g mixture containing 700 g resin and 210 g hardener was used in the case of a 121 cm × 30 cm fabric. Secondly, it was tricky to arrange the insertion of the inlet pipe into the mixture, which is closely related to resin feed properties. The inlet pipe needed to be tailored with an appropriate length, and then its flat end cut with an angle of 45 degree and completely immersed into the mixture. In addition, the inlet pipe should be fixed against the bucket wall straightly by tapping.)

2.3.1.6. Resin infusion

When all preparation work was completed, resin infusion was operated using vacuum conditions. First the feeding of the system with the resin mixture was started by loosening the clamp on the inlet pipe. When the fabric was fully covered by the mixture, the inlet pipe was clamped again. It took about 36 hours for the CFRP plate to be completely cured. Then the CFRP fabrication step was finished by removing vacuum connections and taking out the CFRP plate.

(Note: it is worth remembering that the resin flow speed should be kept under control by using the clamp. It took about 10 minutes for the mixture to cover whole area of the fabric and spreading from mesh edge to fabric edge spends most of this time. The curing time of 36 hours can only be used as reference. The curing of CFRP plate can be confirmed by the fact that mixture remaining in bucket becomes solid and the inlet pipe becomes brittle.)

2.3.2 Adhesive bonding

The bonding approach using adhesive films was performed to construct the specimen with made structural members. In the application of adhesive film, a vacuum bag and an autoclave are involved to control the vacuum, temperature and pressure. The process can be divided into 3 steps, each comprising several actions.

2.3.2.1 Preparation

A piece of Nomex honeycomb was first cut out from a sheet product of ECA 3.2-48 using a knife into rough dimensions. The specifications of this product are given in table 2.3, where L stands for the ribbon direction and W stands for the transverse direction. Then, the edges of the honeycomb were peeled off along the ribbon direction, strip by strip, until the desired width of 5 cm was obtained.

Product	ECA 3.2-48 (Aerospace grade)	Cell wall thickness	51 μm
Manufacturer	Euro-Composite	Compressive strength	2.1 N/mm^2
Cell size	3.2 mm	Shear strength (L)	1.32 N/mm^2
Density	48 kg/m^3	Shear strength (W)	0.72 N/mm^2
Dimension (L)	1220 mm	Shear modulus (L)	48 N/mm^2
Dimension (W)	2440 mm	Shear modulus (W)	30 N/mm^2
Thickness	10 mm		

Table 2.3 Specifications of the Nomex honeycomb sheet

Four CFRP pieces were cut out from the plate fabricated in the last step: two skins with a size of 120 cm \times 5cm and two walls with a size of 120 cm \times 1 cm. Besides, adhesive films were taken out from freezer one day in advance and cut into four pieces to have the same sizes as the CFRP skins and walls. Other work in this step includes preparation of four wooden blocks and cleaning an aluminum plate. The wooden blocks were placed around the specimen to provide a side protection in the pressurized environment. Therefore, a slope was made on one side of each block in order to partially transfer a side pressure to a down force. Furthermore, the height of the blocks was little more than 1 cm and all edges that could possibly contact the vacuum bag were rounded off. Finally, a clean plate was ready to be used as a mold and its edges were taped.

(Note: Obtaining the structural members with accurate sizes is the main objective in this step. The honeycomb core after cutting was 120 cm long, 5 cm wide and 1 cm thick. In general, a cutting machine is needed to cut CFRP plates. However, tailoring one layer of CFRP plate along

the fiber direction can still be performed using a knife. Because the transverse dimensions of skins and walls are relatively short compared with that in the fiber direction, a knife was used in this case. Moreover, it is also important to have a precise size match between the sides of the core and the skins or walls.)

2.3.2.2 Placement

The placement for adhesive bonding was relatively simple. First, a piece of Teflon was placed on the aluminum plate and several pieces were used to wrap the wooden blocks to prevent adhesion. Secondly, adhesive films were placed between the honeycomb and CFRP skins/ walls after their protective layers were peeled off. In this way, all structural members can be put on the center of the plate as a complete structure. The four wooden blocks were placed around this structure to support it from four sides. Another piece of Teflon was placed on the top surface of the structure to prevent adhesion since bleeders were subsequently laid on the whole setup. When the layout of the outlet path was implemented by placing bleeders, the three sides of vacuum bag were sealed. The fourth side was temporarily left open for the convenience of installing a vacuum connector on the vacuum bag. At last, the vacuum connector was set at one end of the largest bleeder and the remaining side of vacuum bag was sealed.

(Note: there were three pieces of bleeders contributing to an effective bleeding system: one was right on the top skin and about the same size as the latter; a larger one covered the whole area; the last bleeder was folded to have double layers and was placed under the connector. Due to the difference in thickness induced by the wooden blocks, several loops of gum tape were used on the vacuum bag edges.)

2.3.2.3 Sending to autoclave

The aluminum plate and the whole setup on it were moved to the specialized autoclave platform and were firmly fixed on it with tapes. The vacuum connector was connected to a vacuum system of the autoclave. Then it was possible to check the airtightness of the vacuum bag from vacuum data in autoclave system controller. The most important step was to program the autoclave cycle. In this cycle, three parameters were controlled during the process inside the autoclave. The temperature changed from room temperature to 120 °C with a ramp of 2 °C/min and then was kept at 120 °C for 60 min, which was followed by a drop back to the room temperature with a cooling ramp of -2 °C/min. This temperature variation served to make the adhesive film melt to a certain extent and cure again, resulting in a strong bond between different structural members. With regard to vacuum, full vacuum was used under 80 °C and no vacuum was applied once temperature was above 80 °C. The reason why full vacuum was not kept through the whole system is to prevent a volume expansion of trapped air. The last parameter, pressure, was maintained at 1.5 bar in the cycle. After programming the cycle, the platform was sent into the autoclave and the cycle was started. A final product of the specimen was taken out when the curing was completed.

(Note: when a vacuum was tested, tightly pressing the gum tapes can be helpful in case of leakages. Also, the constant value of pressure was set based on the experience gained from trial

productions. Some deformations of unprotected top skin were observed on first few products after curing process. So it was concluded that the pressure of 2 bar that was used in those trial productions generated a overlarge downward load, causing the deformations of the top CFRP skin.)

2.3.3 Optimized fabrication setup

Although the manufacturing parameters and procedure are consistent through all fabrications, there are still some unexpected variables between fabrication times due to different equipment status and working environment. The solution was to manufacture the two specimens used for comparison in one batch. The motivation of manufacturing two specimens in one batch was to reduce production factors in the comparison results. Other considerations include cost reduction and energy saving.

When fabricating two specimens at once, the material consumption for vacuum system setup was nearly same as for the fabrication of one specimen. In addition, because heating, pressurization and vacuum were applied in the 3-hour cycle inside autoclave, a great deal of energy was required. Therefore, it is well worth fabricating two specimens in one batch in the bonding step even though the placement needs to be modified. The modified placement is depicted in figure 2.8 with specimens are marked in light blue color.

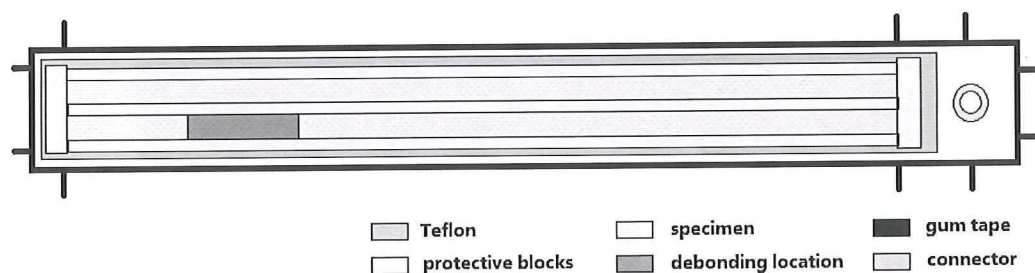


Figure 2. 8 Top view of adhesive film bonding placement for two specimens

To fabricate two composite structures simultaneously, double sets of CFRP plates, adhesive films and honeycomb cores were prepared. Also, one extra long protective wooden block was placed between two structures, and bleeders were tailored based on the new size of setup. As mentioned, these two specimens are designed to be in a comparison group. Therefore, one of them is supposed to be fabricated with an artificial defect, a debonding area between the core and the bottom CFRP skin. This debonding area is marked with dark blue color in figure 2.8.

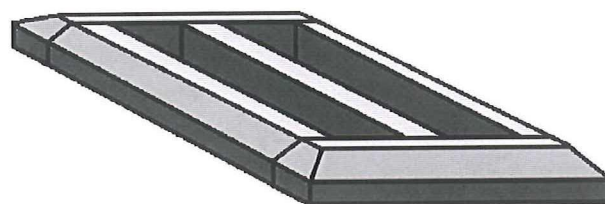


Figure 2. 9 Sketch of protective wooden blocks

Figure 2.9 shows details of the wooden blocks used to protect specimens. A good match between the dimensions of different blocks is required to have proper contacts with two structures and to prevent damaging the vacuum bag. As explained in section 2.3.2.1, each wooden block is made with a slope to relieve the force exerted on structures.

2.3.4 Specimen

Three of the fabricated composite beams are used as experimental specimens. They have same dimensions and structure, but one of them was fabricated with a defect while the other two were not. According to the production sequence, they are named as beam 1, beam 2 and beam 3. After several trial productions were carried out to optimize production parameters and process, beam 1 was made as the first specimen. Subsequently, beam 2 and beam 3 were fabricated in one batch with a debonding area between the skin and the core of beam 3.

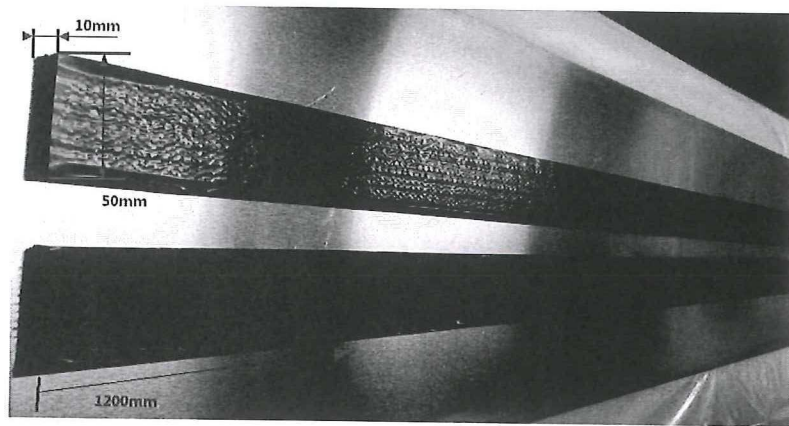


Figure 2.10 Final products of beam 2 and beam 3

A series of tests are planned to perform on beam 1 for the purpose of collecting the structural characteristics of the specimen and to test the applicability of wireless sensor networks and the measurement system. Then, beam 2 and beam 3 will be tested in a dynamic condition, which partially simulates the operating condition of rotor blades. By comparing the data measured from these two specimens, features sensitive to defects can be identified and analyzed, contributing to the establishment of the SHM system parameters.

2.4 Summary

Composite helicopter rotor blades have been developed to improve the performance of rotor blades. Composite materials such as GFRP and CFRP can provide high strength-to-density ratios and composite structures allow flexible and advanced designs of helicopter rotor blades. In applications, composite rotor blades can replace their metal counterparts to be operated on many helicopters. The motives include improving strength properties, allowing advanced aerodynamic design concepts, and improving fatigue resistance. Pre-pregs are often used in the manufacture of composite rotor blades and various techniques such as automatic profiling, curing, and adhesive bonding may be applied in the process. According to a typical design of

composite rotor blade, a foam structure, a spar, and a honeycomb sandwich structure are the most critical elements. Therefore, defects that are possibly introduced in these elements need to be considered. Among them, one of the most significant defects is a debonding or delamination between the honeycomb core and facing materials since it will introduce a strength loss and a risk of water penetration.

The Robinson R22 helicopter was introduced as a reference helicopter for the design of a simplified rotor blade, which is the experimental specimen in this thesis. This type of popular light helicopter has two small-sized rotor blades and a rotor hub with a relatively simple structure. Simplified from the structure of the R22 rotor blades, the specimen is designed as a composite beam with a rectangular cross-section. And its dimensions were determined by scaling-down the size and considering the feasibility for fabrication. Based on an investigation of composite rotor blade defects, which is presented in section 2.1.3, debonding was selected as the an artificial defect on the specimen.

In order to fabricate specimens in accordance with the design, two main steps are taken in a fabrication process: CFRP plate fabrication and adhesive bonding. The first step applies techniques of vacuum infusion to obtain a CFRP plate with high quality. Adhesive films, a vacuum system, and a curing cycle in an autoclave are involved in the second step. In addition, some modifications in fabrication setup were required to produce two specimens in one batch. The reason is to exclude producing factors from a comparison between these two specimens, one of which is defected. In total, three specimens (beam 1, beam 2, and beam 3) were fabricated for use in experiments with a measurement system based on wireless sensor networks.

2.5 References

1. Li L. Structural Design of Composite Rotor Blades with Consideration of Manufacturability, Durability, and Manufacturing Uncertainties: PhD thesis, Georgia Institute of Technology; 2008.
2. Handbook of composite reinforcements. John Wiley & Sons, 1992.
3. Saadatmanesh H, Ehsani M. RC Beams Strengthened with GFRP Plates. I: Experimental Study. *Journal of Structural Engineering*. 1991;117(11):3417-33.
4. Meier U, Kaiser H, editors. Strengthening of structures with CFRP laminates. *Advanced composites materials in civil engineering structures*; 1991: ASCE.
5. Megson T H G. *Aircraft structures for engineering students*. Elsevier, 2012.
6. Antonio Miravete, editor. ICCM/9: Composites properties and applications. University of Zaragoza, Woodhead publishing limited, 1993.
7. Airbus Helicopters. Aircraft Finder, civil range, overview [cited 2015 January 26th]. Available from: http://www.airbushelicopters.com/rsite/en/ref/Overview_56.html.
8. Astrom B T. *Manufacturing of polymer composites*. CRC Press, 1997.
9. Sanchez Ramirez A, Das K, Loendersloot R, et al. Wireless sensor network for helicopter rotor blade vibration monitoring: requirements definition and technological aspects[J]. *Key Engineering Materials*, 2013, 569: 775-782.
10. Balaskó M, Sváb E, Molnár G, Veres I. Classification of defects in honeycomb composite structure of helicopter rotor blades. *Nuclear Instruments and Methods in Physics Research Section A: Accelerators, Spectrometers, Detectors and Associated Equipment*. 2005 4/21;/542(1-3):45-51.
11. Pawar PM, Ganguli R. Helicopter rotor health monitoring- a review. *Proceedings of the Institution of Mechanical Engineers, Part G: Journal of Aerospace Engineering*. 2007 May 1, 2007;221(5):631-47.
12. Kee Paik J, Thayamballi A K, Sung Kim G. The strength characteristics of aluminum honeycomb sandwich panels[J]. *Thin-walled structures*, 1999, 35(3): 205-231.
13. Company RH. R22 Beta Helicopter 2014 [cited 2014 April 11th]. Available from: http://www.robinsonheli.com/rhc_r22_beta_ii.html.
14. Paul Cantrell. Semi-rigid main rotors [cited 2015 January 26th]. Available from: http://www.copters.com/mech/mr_semi.html.
15. Transportation USN. Robinson Helicopter Company R22 Loss of Main Rotor Control Accidents: General Books; 2011.
16. Tim McAdams. Robinson's coning hinge [cited 2015 January 26th]. Available from: <http://blog.aopa.org/helicopter/?p=420>.
17. Company RH. Robinson R22 Maintenance Manual 2014 [cited 2014 April 11th]. Available from: http://www.robinsonheli.com/r22_mm.html.
18. Investigation AF. Robinson R22 Beta, G-IORG. 2003.

Chapter 3

Measurement and Monitoring Hardware

3.1 Introduction

The structural health monitoring (SHM) system that is intended to be established in this thesis monitors the structural health of specimens by collecting and analyzing their real-time parameters. Therefore, the measurement system plays an important role in providing accurate data in this SHM system. Data transmission is fulfilled by applying a wireless sensor network (WSN) and strain gauges function as sensors to provide the WSN with real-time strains at different locations on the specimens. These two main elements of the monitoring system, the strain gauge and the WSN, are introduced in detail in this chapter.

3.2 Strain gauge

3.2.1 Theory

Strain monitoring is a method of detecting changes in length at specific points on an object, but does not directly detect damage in a structure. After data processing, changes in length or deformations can be related to stress and load. Strain sensors are utilized to obtain material strain levels at specific positions. In order to mount these sensors in critical areas, prior knowledge of expected strain and stress distributions is required. The most frequently applied sensors for strain measurements are electrical sensors and fiber optic sensors (1).

3.2.1.1 Electrical strain gauge

Electrical strain gauges have emerged as the most common sensors in the toolbox of strain monitoring. Basically, they are small, precise resistors mounted on a carrier, which is bonded to the structure. Because of this configuration, even small production defects of the foil and carrier

material may negatively affect the measurement sensitivity and stability of electrical strain gauges. However, their low cost and great applicability in various conditions still lead to a domination of the strain gauge market.

Based on the sensitivities of different electrical parameters to a strain, several types of electrical sensors including resistance, capacitance, inductance and semiconductor sensors have been developed. Using resistance strain gauges is considered as the most popular approach for strain measurements, by relating the change in resistance of an electrical conductive wire to displacement. Typically, a Wheatstone bridge circuit is integrated to measure changes of resistance accurately, and sometimes a rosette comprising of three these strain gauges can be applied to measure strain and determine principal directions as well (2). A typical example of a rosette strain gauge is shown in figure 3.1.

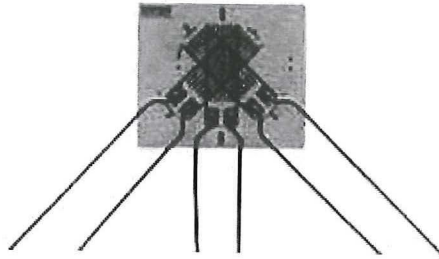


Figure 3. 1 Three-element stacked rosette strain gauge (3)

Although electrical strain sensing is already a well-established technology with inexpensive sensors, it suffers from some disadvantages. First, it is limited to indirect and surface strain measurements, which make it possibly not suitable for some complex structures. Secondly, electrical strain sensors are susceptible to electromagnetic interference and fatigue loading to some extent (4).

3.2.1.2 Fiber optic sensor

Along with the growth of fiber optics applications in the telecommunications industry, fiber optic sensors have been introduced into strain monitoring area with commercial availability and increasingly competitive costs. Among the many new fiber sensor architectures and applications, three techniques have most been often employed in fiber optic sensing: intensity based sensors, phase modulated interferometers and wavelength based sensors (5). The last type, also known as Fiber Bragg Gratings (FBG), has become the most popular fiber optic sensor since it was developed. FBG sensors are capable of detecting a narrowband of reflected light whose frequency changes with deflection. The central wavelength of the reflected component satisfies the Bragg relation:

$$\lambda = 2n\Lambda \quad (3.1)$$

where n is the index of refraction and Λ denotes the period of the index of refraction variation of the FBG sensor. Therefore, when a Bragg grating is subjected to an uniform strain, the wavelength of the spectrum reflected by it shifts and this shift is recorded and related to the strain level (6). Figure 3.2 illustrates the principle of strain sensing by the FBG sensor, in which the

wavelengths of reflected and transmitted light change due to a strain imposed on the optical fiber.

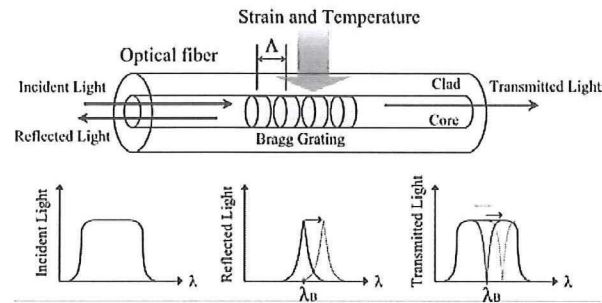


Figure 3. 2 Principle of FBG sensor operation (7)

Multiplexing by engraving several sensors on a single fiber is an outstanding advantage of FBG sensors. At present, there are two methods of multiplexing: wavelength division multiplexing (WDM) and time division multiplexing (TDM). The former requires the sensors on one fiber to have different grating spacings while the latter has all sensors written at same wavelength and discriminated by the arrival time of reflected signals (8). FBG sensors suffer from temperature effects due to changes induced in refractive index and thermal expansions of the grating and correction with respect to temperature factors is required for an accurate strain measurement. However, FBG sensors offer some favorable characteristics: multiple sensors sharing a transmission line; great operational stability in extreme environments; no concern on electro-magnetic interference; no need for recalibration. In addition, FBG sensors can be embedded within composite materials without creating voids or raising stress due to their minute size.

3.2.1.3 Selection

In this thesis, resistance strain gauges are employed to perform strain measurement primarily from the considerations of cost and applicability. Also, specimen fabrication needs extra work if embedded FBG sensors are used for strain measurements. Compared with FBG sensors, the placement of resistance strain gauges bring less influence on a structure due to their small size. Since the CFRP skins undertakes most of the bending moment, strain on their surfaces are vital parameters for evaluating the structure's condition. In general, resistance strain gauges can provide effective and accurate measurements for the experiments performed in this thesis. These experiments are described in chapter 4, chapter 5, and chapter 6 according to different test setups. When using resistance strain gauges, influence of environment on strain gauge stability is worth noting, even though the experimental environment is neither with severe electromagnetic interference nor under long-time fatigue load.

3.2.2 Placement

The type of strain gauges employed in experiments is KFG-5-120-C1-23 (produced by KYOWA company), whose gage length and resistance are 5 mm and 120 Ω respectively. They can be

operated with a strain limit of approximately 5% at room temperature and have self temperature-compensation in the range 10 °C to 100 °C. These two properties make this type of strain gauges a good candidate for strain measurement in this thesis. Also, the last number in this product name stands for an applicable linear expansion coefficient of $23 \times 10^{-6}/^{\circ}\text{C}$, which is suitable for application on aluminum materials and composite materials (9). Among all specifications, the gage resistance of 120 Ω is additionally of importance because it needs to be taken into account when the Wheatstone bridge circuits are configured.

Because the strain gauges were permanently bonded on the specimens, their positioning and the bridge circuits they connected into were identical across all experiments in this thesis. Then, it is possible to introduce the strain gauge layouts and the bridge circuit configurations ahead of the chapters describing experiments.

3.2.2.1 Strain gauge layout

As described in the section 2.3.4, three specimens are named beam 1, beam 2, and beam 3. Among them, beam 3 is the only specimen with an artificial defect, a debonding area between its bottom CFRP skin and its core. Because of different testing objectives, beam 1 has a layout of strain gauges different from those of beam 2 and beam 3. For comparison, beam 2 and beam 3 share same strain gauge layout. In figure 3.3, the free end of a specimen is labeled as tip while the fixed end is labeled as root. Each strain gauge is denoted by SG and the bracketed SG stands for a strain gauge that is attached on the bottom skin surface. As shown in figure 3.3 (a), beam 1 has ten strain gauges mounted on it. In order to allow an accurate measurement capable of achieving temperature compensation itself, two full bridge circuits and one half bridge circuit are made for these ten strain gauges. The first full bridge circuit (SG1-SG4) measures bending strain at 1 m location; the second full bridge (SG5-SG8) measures shear strain at 22 cm location; the half bridge measures bending strain at 90 cm location. In the layout of beam 2 and beam 3, which is depicted in figure 3.3 (b), six strain gauges are mounted and each strain gauge is operated in a quarter bridge circuit. In these six quarter bridge circuits, four are used for measuring bending strain and two measure shear strain. The locations of strain gauges are determined depending on the location of the debonding area, which is located from 65 cm to 90 cm. Therefore, the influence of debonding can be investigated by analyzing the strain data obtained from both sides of the debonding area.

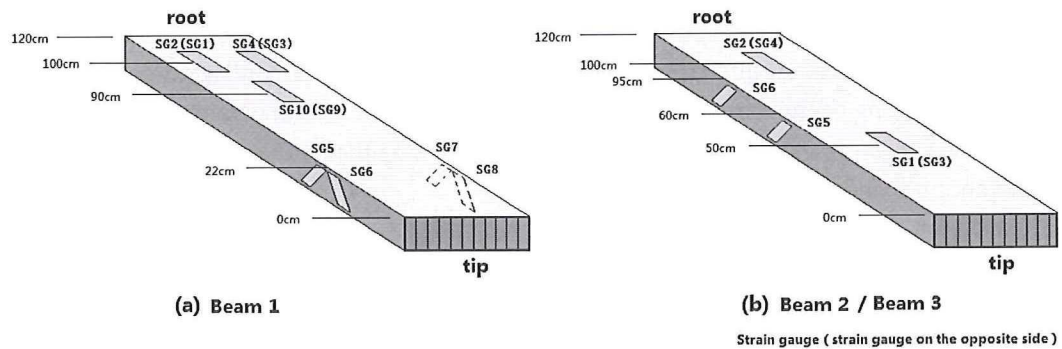


Figure 3. 3 Strain gauge layouts on (a) beam 1 and (b) beam 2/ beam 3

3.2.2.2 Bridge circuit configuration

In a full-bridge circuit, four strain gauges form the bridge, and for a half-bridge circuit or a quarter-bridge circuit, external resistors are needed to complete the circuit. All bridge circuit configurations are shown in figure 3.4, in which figure 3.4 (a), (b), and (c) are for beam 1 and figure 3.4 (d) is for beam 2 and beam 3. Bridge circuits are connected to sensor nodes of the wireless sensor network to provide real-time strain data. Specifically, a bridge circuit is connected to a differential input channel of the sensor node through four node pins (SP+, S+, S-, GND). The pin of SP+ is a sensor excitation output pin and powers the strain gauges in the circuit, pins of S+ and S- are positive and negative input to the node programmable gain amplifier while GND pin is for power return. The connections with these node pins are marked as red dot in figure 3.3. Circuit boards were made for carrying external resistors employed in the half-bridge circuit and quarter-bridge circuits.

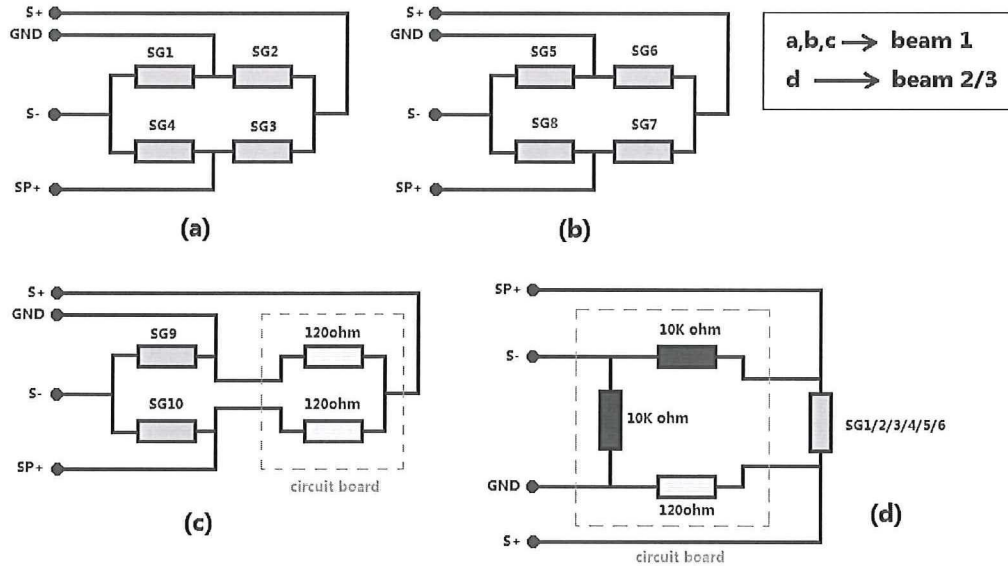


Figure 3.4 Bridge circuits for strain measurement: (a) and (b) are the full-bridge configurations; (c) is the half-bridge configuration; (d) is the quarter-bridge configuration

Six quarter-bridge circuits share same configuration, which is shown in figure 3.4 (d). It can be seen that the configuration includes electrical resistors with two resistances : 120Ω and $10 \text{ k}\Omega$. In a standard quarter bridge, all three resistors are supposed to be 120Ω , which is same resistance as the strain gauge.

In experiments, two sensor nodes can be used to wirelessly transmit data from six strain gauges and one temperature sensor simultaneously, so each sensor node needs to be connected with three quarter bridge circuits. However, a maximum of two standard quarter-bridge circuits are allowed for one sensor node due to a current limit of sensor node of 50 mA. So resistors with much higher resistance ($10 \text{ k}\Omega$), which use almost no current, are used to complete half of the quarter-bridge circuit. Compared with other solutions such as replacing internal resistors of

sensor nodes and making a printed circuit board (PCB) for each bridge circuit, this external modification solution is much more simple and feasible since those two solutions would require extra time and the cost of delivery back to the manufacturer and modification.

3.3 Wireless sensor networks

3.3.1 Theory

A wireless sensor network (WSN) consists of three main components: nodes, gateways, and a host system. Spatially distributed measurement nodes interface with sensors to measure targeted parameters. The acquired data is then transmitted wirelessly to the gateway. The gateway is capable of operating independently or connecting to a host system. The measured data is collected, processed, analyzed, and transferred by software in the host system. In addition, a special type of measurement node, known as a router, can be utilized to extend the distance and improve reliability of WSN (10).

With a battery and a protective enclosure, sensor nodes are applicable for long-term outdoor deployment. Some sensor nodes also can be programmed to have customized behavior and realize intelligent local analysis (11). Therefore, transmitting data after local analysis can be an option to prolong the battery life of nodes. It is worth mentioning that sensor nodes generally provide analog or thermocouple input channels. In a WSN, a gateway collects measured data from distributed wireless nodes and links up with the host system. A gateway also functions as a network coordinator for node authentication and information buffering. It is possible to have multiple gateways in a WSN communicating through non-overlapping wireless channels. In practical applications, a PC usually plays the role of a host system in the WSN. Software employed in a PC is commercially available and able to accomplish functions of network management, analysis, and control with user interfaces. Based on these functions, software can be developed for various applications such as data logging, event detection, alarming, service notification, and data visualization.

IEEE 802.15.4 is a standard basis of protocols for wireless personal area networks (WPAN) and specifies protocols in aspects of physical layer and media access control (12). The physical layer is responsible for data transmission, channel selection and radio frequency transceiver management. Primary functions of the medium access control are providing management interface and access to the physical channel. Base on IEEE 802.15.4, protocols such as ZigBee, ISA 100.11a, WirelessHART, and MiWi have been developed (13). ZigBee is one of the most popular protocols for WPAN as it allows applications of low cost, low power consumptive and highly flexible wireless technologies. ZigBee operates in three frequency bands: 868 MHz in Europe, 915 MHz in the USA and Australia, and 2.4 GHz in rest of the world (14). In order to ensure network security, 128 bit keys are used throughout the wireless network. And the transmission range of a ZigBee wireless network often varies between 10 m and 75 m depending on power output and environmental factors (15).

3.3.2 Application

In this thesis, a WSN provided by LORD MicroStrain is employed to perform measurement and establish a SHM system and its configuration is shown in figure 3.5. The sensor nodes of this WSN allow data acquisition from multiple sensors such as strain gauges, accelerometers, and temperature sensors. Also, it is possible to operate these sensor nodes with a flexible configuration. Other two components in a typical WSN, a gateway and a host system, are also included in this WSN using commercial products from the company. The host system is a PC and the software on it performs functions of managing data acquisition, controlling sampling process and so on (16).

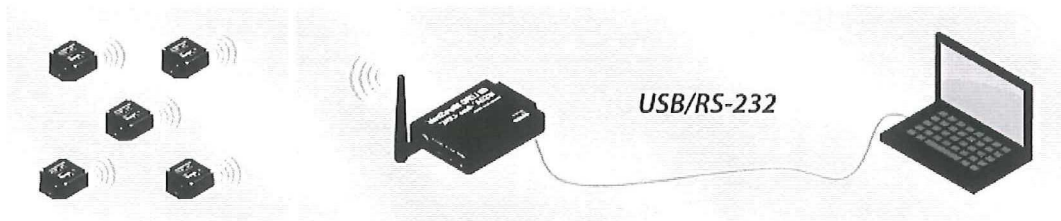


Figure 3. 5 Configuration of the wireless sensor network (16)

3.3.2.1 LXRS protocol

LXRS wireless protocol is used in this WSN. It is based on IEEE 802.15.4 communication standard and operates at 2.4 GHz. Data transmission of LXRS wireless protocol has been developed to be lossless, synchronized, and with extended range. Because the LXRS protocol supports a bi-directional radio communication in the network, data that are not acknowledged by the gateway can remain in the node's memory for next transmission package. In addition, as part of work to ensure a reliable data transmission, all data are converted to be digital and time-stamped at the same time in sensor nodes. The LXRS protocol allows a communication range up to 2 km and programmable depending on requirements of power consumption and security. In the experiments carried out in this thesis, communication range is limited within 10 m by laboratory space and electromagnetism environment. Another important feature of this protocol is that sensor nodes are synchronized with an accuracy of ± 32 microseconds and re-synchronized every 20 seconds. Although the gateway supported by the LXRS protocol can be wirelessly connected with thousands of sensor nodes, there is a trade-off between the total number of sensor channels and the sampling rate. For instance, the sampling rate can reach 512 Hz with only 3 utilized sensor channels but the value may fall to 128 Hz when 31 sensor channels are involved (17). By applying the LXRS wireless protocol, two V-Link-LXRS sensor nodes, one G-Link-LXRS sensor node, and a base station are integrated in the WSN in this thesis. They are described in the following sections.

3.3.2.2 V-Link-LXRS sensor node

A V-Link-LXRS wireless sensor node (LORD Microstrain) features 4 different input channels with optional bridge completion, 3 single ended input channels with 0-3 volt excitation, and an internal temperature sensor channel. The analog input channels are operated with a resolution of 16 bits and 0.1% accuracy. They support different Wheatstone bridges and a wide range of analog sensors. The internal temperature sensor performs a temperature measurement in a range from -40 °C to 85 °C with an accuracy of 2 °C. Power supply of this type of sensor node is from a 3.7 Volts of direct current (V dc), 650 mAh lithium ion rechargeable internal battery or a 3.2 to 9.0 V dc external power connection. A V-Link-LXRS sensor node has a data storage capacity of 4 megabytes and four sampling modes including synchronized, armed data-logging, streaming and low duty cycle modes (18). A V-Link-LXRS sensor node weighs 141 g and its picture is shown in figure 3.6.

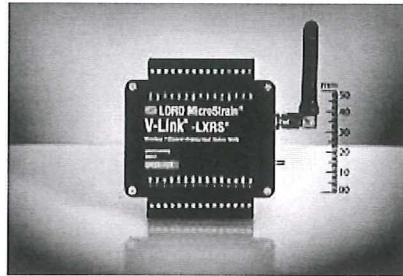


Figure 3. 6 V-Link-LXRS sensor node (18)

3.3.2.3 G-Link-LXRS sensor node

A G-Link-LXRS sensor node is a wireless accelerometer node and features on-board tri-axial MEMS accelerometers and an internal temperature sensor. Accelerometers integrated inside the sensor node measure acceleration in a range of ± 10 g and with a measurement accuracy of 10 mg. The internal temperature sensor has similar measuring capability with its counterpart in a V-Link-LXRS sensor node but with a slightly smaller measurement range (-40 °C to 70 °C). The G-Link-LXRS sensor node allows remote, long term deployment with lossless data throughput and low power consumption. Simultaneous operations of data logging to internal memory and data transmitting to a gateway can be implemented by this sensor node. Its specifications in the power supply, sampling modes are specified similar with those of the V-Link-LXRS sensor node. However, compared with the V-Link-LXRS sensor node, the G-Link-LXRS sensor node has a lower resolution of analog channels (12 bit), a smaller data storage capacity (2 megabytes), and a smaller weight (40 g) (19). Figure 3.7 presents a picture of a G-Link-LXRS sensor node.

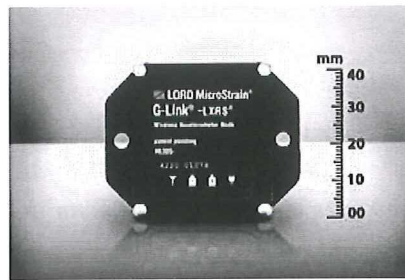


Figure 3. 7 G-Link-LXRS sensor node (19)

3.3.2.4 Base Station

A base station, LORD Microstrain WSDA-Base-102-LXRS Wireless RS-232 Base Station, functions as a gateway in the WSN and is shown in figure 3.8. It is compatible with all 2.4 GHz wireless nodes including two types of sensor nodes described above and provides seamless communication between these wireless sensor nodes and a host PC. The radio frequency utilized varies from 2.405 GHz to 2.470 GHz, which is license free worldwide. Its quick deployment with the host PC is supported by a RS-232 connection at a data rate of 11520 bps or 921600 bps. A cost effective measurement can be achieved by using a single base station to manage a great amount of wireless sensor nodes. The base station can be simply powered by PC as they are connected by a cable. Its power consumption is, for instance, 65.6 mA when 8 active node channels operate at 256 Hz and 45.7 mA in idle condition (20).



Figure 3. 8 WSDA-Base-102-LXRS base station (20)

3.3.2.5 Node Commander

Node Commander is a software provided by LORD Microstrain and operates the LXRS wireless sensor nodes and the base station. It can accomplish multiple tasks including configuring all wireless devices in the WSN, operating data acquisition in various sampling modes, displaying real-time data, and producing data files. Node Commander is capable of discovering wireless nodes within range and setting up the sensors that are attached to wireless nodes. During simultaneous data acquisition from multiple sensor nodes, a flexible management of data rates and sensor node batteries is allowed by using this software. Also, the written data files, which have time stamping, data separators, and numeric decimators, can be imported into data analysis programs for further processing (21).

3.4 Other hardware

In addition to the primary monitoring integrating strain gauges and a wireless sensor network, some hardware such as load cells, a dial gauge, and a ZABER actuator performed real-time data measurement as well. There were two load cells employed in experiments: a compressive load cell integrated in stiffness test rig and the other one monitoring the end load on the specimen during static tests and dynamic tests. The compressive load cell measured a vertical force that is exerted on the specimen for reaching certain bending curvature. Its measurement capability is up to 980 N. The second has a smaller measurement range with a maximum limit of 50 N. It was calibrated under tensile and compressive loads in advance to acquire factors of the voltage-to-force conversion. During tests, the real-time force can be read by sending data from this load cell to an amplifier or be written in files by a further connection to a PC. The dial gauge was installed on the stiffness test rig same as the compressive load cell and performed a curvature measurement while the specimen was bent with an accuracy of 0.01 mm. In order to generate required displacements of the specimen tip, a ZABER linear actuator was mounted to support the specimen tip and used to lift it in static tests and slow dynamic tests. The actuator also performed a position sensing to determine the displacement of the specimen tip and sent the real-time data back to a PC via a controller. Therefore, it played an important role in the measurement and monitoring system in this thesis. Further information of the hardware mentioned in this section will be given in detail when introducing test setups in later corresponding chapters.

3.5 Summary

Strain measurement and a wireless sensor network are the two basic elements of the monitoring system in this thesis. Strain measurements can be performed by applying electrical sensors or fiber optic sensors. In the former group, resistance strain gauges are most often used, while FBG sensors are significantly developed among fiber optic sensors. Taking factors of cost, applicability, and manufacture into account, resistance strain gauges were selected for this thesis. In experiments, two strain gauge layouts are determined for beam 1 and beam 2/ beam 3, serving for different testing objectives. According to the strain gauge layouts, different bridge circuits are configured to provide accurate strain data to the WSN.

Sensor nodes, gateways, and a host system compose a WSN, and protocols based on IEEE 802.15.4 standard allow an effective wireless data transmission throughout the network. In this thesis, the WSN employed is configured by the LXRS protocol, two V-Link-LXRS sensor nodes, a G-Link-LXRS sensor node, a base station, and control software on a PC. Among them, V-Link-LXRS sensor nodes can offer access for various sensors including strain gauges and the G-Link-LXRS sensor node is used as an accelerometer to monitor the acceleration and vibration during experiments. The base station functions as a network coordinator, which collects measured data from sensor nodes and sends to the PC. And the software is used to manage the whole WSN and process data for further analysis.

Other hardware utilized to measure real-time data during experiments in this thesis include two load cells, a dial gauge, and a ZABER actuator. They performed measurements of force,

displacement, and position respectively and these measurement results provided direct conclusion of specimen properties or be used as supporting information for the results obtained from the WSN to investigate the structural response of specimens.

3.6 References

1. Dally J W, Riley W F. Experimental stress analysis. McGraw-Hill New York; 1965.
2. Schubel PJ, Crossley RJ, Boateng EKG, Hutchinson JR. Review of structural health and cure monitoring techniques for large wind turbine blades. *Renewable Energy*. 2013; 51(0):113-23.
3. National Instruments. Identify and characterize damaging PCB assembly and test processes using strain gage testing [cited 2015 January 28th]. Available from: <http://www.ni.com/white-paper/6534/en/>
4. Edwards A T. Comparison of strain gage and fiber optic sensors on a sting balance in a supersonic wind tunnel. Virginia Polytechnic Institute and State University, 2000.
5. Todd MD, Nichols JM, Trickey ST, Seaver M, Nichols CJ, Virgin LN. Bragg grating-based fibre optic sensors in structural health monitoring. *Philosophical Transactions of the Royal Society A: Mathematical, Physical and Engineering Sciences*. 2007; 365(1851):317-43.
6. Balageas D, Fritzen C-P, Güemes A. Structural health monitoring: Wiley Online Library; 2006.
7. Technology LS. Fiber Bragg Grating Sensor 2014 [cited 2014 April 9th]. Available from: <http://www.lazoc.jp/english/technical/principle/000101.html>.
8. Gangopadhyay TK. Prospects for fibre Bragg gratings and Fabry-Perot interferometers in fibre-optic vibration sensing. *Sensors and Actuators A: Physical*. 2004; 113(1):20-38.
9. Kyowa. KFG series General-purpose foil strain gages [cited 2015 January 29th]. Available from: http://www.kyowa-ei.com/eng/product/category/strain_gages/kfg/index.html.
10. National Instruments. Understanding the WSN architecture 2014 [cited 2014 April 11th]. Available from: <http://www.ni.com/wsn/whatis/#architectures>.
11. National Instruments. NI WSN-3214 (Programmable) [cited 2014 April 11th]. Available from: <http://sine.ni.com/nips/cds/view/p/lang/en/nid/210012>.
12. Gutierrez JA, Naeve M, Callaway E, Bourgeois M, Mitter V, Heile B. IEEE 802.15. 4: a developing standard for low-power low-cost wireless personal area networks. *Network, IEEE*. 2001;15(5):12-9.
13. Lacono L. wireless sensor networks protocols 2011 [cited 2014 April 11th]. Available from: <http://www.sase.com.ar/2011/files/2010/11/SASE2011-Protocolos para Redes de Sensores Inalambricos.pdf>.
14. IEEE 802.15. IEEE 802.15 WPAN Task Group 4 2014 [cited 2014 April 11th]. Available from: <http://www.ieee802.org/15/pub/TG4.html>.
15. ZigBee Alliance. ZigBee Specification FAQ. 2013.
16. LORD MicroStrain. Wireless Overview 2013 [cited 2014 April 11th]. Available from: <http://www.microstrain.com/wireless>
17. LORD MicroStrain. LXRS PROTOCOL 2013 [cited 2014 April 11th]. Available from: <http://www.microstrain.com/wireless/lxrs-protocol>.
18. LORD MicroStrain. V-Link-LXRS 2013 [cited 2014 April 11th]. Available from: <http://www.microstrain.com/wireless/v-link>.
19. LORD MicroStrain. G-Link-LXRS 2013 [cited 2014 April 11th]. Available from: <http://www.microstrain.com/wireless/g-link>.
20. LORD MicroStrain. WSDA-Base-102-LXRS 2013 [cited 2014 April 11th]. Available from: <http://www.microstrain.com/wireless/wdda-base-serial>.

21. LORD MicroStrain. Node Commander Software 2013 [cited 2014 April 11th]. Available from: <http://www.microstrain.com/wireless/software>.

Chapter 4

Stiffness Test

4.1 Introduction

Bending stiffness of a specimen is an important parameter associated with its rigidity. In order to measure these parameters for the three specimens, stiffness tests were performed on a test rig shown in figure 4.1. In addition, the elastic flexural modulus of specimens can be calculated from results of the stiffness tests, which contributes to obtaining a basic understanding of the structure of the specimen. This chapter presents the stiffness tests, which is the first experiments chapter in the thesis. It describes the test setup, introduces testing procedures, the display measured results, the calculation and analysis procedure.

4.2 Test setup

The test setup for stiffness tests is shown as figure 4.1 and comprises a rigid frame, a load cell, a lead screw, a display, a square frame and a dial gauge.

The test rig allows a specimen to be simply supported at two points 0.93 m apart, which is less than the total length of the specimen 1.2 m. This distance between supporting points is limited by the dimension of the test rig in this direction. However, test results of stiffness and flexural modulus are not influenced as long as the actual tested length of specimens is substituted. A square frame is placed at middle of the specimen and used for connecting it with a loading system. A lead screw driven by manual rotation via hand wheel is fixed below the frame with a tensile load cell between. So a downward pull force exerted at the middle of the specimen can be generated by operating the hand wheel and will be measured by the load cell. A digital indicator, labeled as display in figure 4.1, is wired with the load cell and performs a conversion from a voltage signal to a force reading. In order to obtain the real-time curvature of the loaded part, a dial gauge is positioned with its needle measuring the vertical displacement.

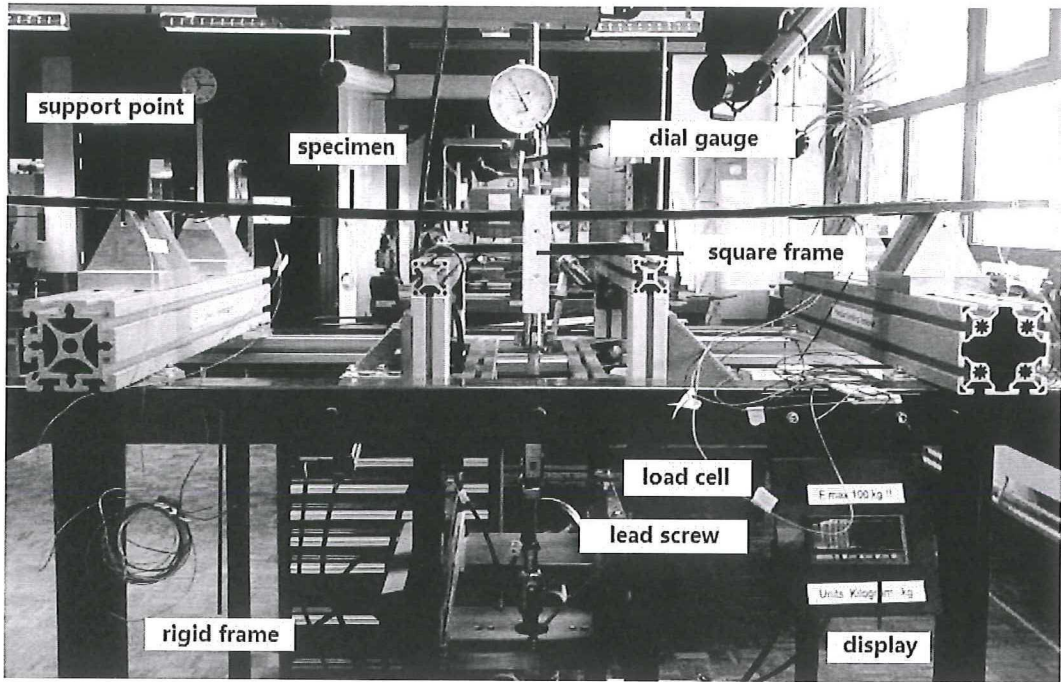


Figure 4. 1 Stiffness test rig

Care must be taken that the zero displacement position corresponds with the zero load cell reading at the start of the test. During a measurement, force is increased step by step by operating the hand wheel, applying an increasing curvature to the loaded specimen. Force and displacement at middle of the specimen for each step are recorded. The maximum force applied to the specimen is about 69 N, which is not too severe to damage the structure of the specimen. It is determined by performing measurements for 20 steps.

4.3 Theory

Because stiffness is defined as $k = F/d$, where F refers to force and d refers to displacement, experimental stiffness of the specimens can be obtained by using the measurement results. Also, flexural elastic modulus can be calculated basing on the specimen performance during stiffness tests. In the case of a simply supported beam with a center load, the relation between deflection and force is given (1):

$$d = \frac{FL^3}{48EI} \quad (4.1)$$

In the formula above, L, E and I denotes total length, flexural modulus, and section modulus respectively. The distance between two supporting points is known: $L = 0.927\text{m}$. So,

$$EI = \frac{0.927^3}{48} \frac{F}{d} \quad (4.2)$$

If assuming the beam as a structure made of a homogeneous material, the modulus of this material can be calculated because the section modulus for a rectangular cross section is known:

$$I = \frac{bh^3}{12} = \frac{0.05 \times 0.01^3}{12} (m^4) \quad (4.3)$$

where b denotes the width of the cross section and h denotes the height. So, the flexural elastic modulus can be acquired: $E = 3982989.915 \frac{F}{d}$. This value allows an estimation of the whole beam's resistance to being deformed elastically in both downward and upward directions.

This is a simplified method usually employed for analyzing the bending behavior of a sandwich structures since it assumes that CFRP skins and walls carry all bending stresses. Based on such assumption, it is worth excluding the factors of material core when bending resistance is concerned. The section modulus, thus, becomes:

$$I = \frac{bh^3 - (b-2t)(h-2t)^3}{12} = \frac{0.05 \times 0.01^3 - 0.04916 \times 0.00916^3}{12} (m^4) \quad (4.4)$$

where t refers to the thickness of the CFRP material. In this case, flexural modulus of the CFRP skins and walls can be calculated. Due to the honeycomb core also making a small contribution to the bending resistance, the actual values of skin modulus are expected to be smaller.

There is another method estimating the flexural modulus of the CFRP material by considering the composite beam as a sandwich structure. For a sandwich structure, it is known that the equivalent flexural rigidity is

$$(EI)_{eq} = \frac{E_f b t^3}{6} + \frac{E_f b t d^2}{2} + \frac{E_c b c^3}{12} \approx \frac{E_f b t d^2}{2} \quad (4.5)$$

where $d = c + t$, c and t denotes the thickness of the core material and CFRP material (2). Therefore,

$$E_f = \frac{2(EI)_{eq}}{b t (h-t)^2} \quad (4.6)$$

4.4 Experiment

Stiffness tests descriptions are divided into two sections according to the specimen. The first section of tests was performed on beam 1 and the second section of test was performed on beams 2 and 3.

4.4.1 Beam 1

The purpose of the stiffness test on beam 1 is to acquire a basic understanding of the structural properties of a fabricated composite specimen. In total, four tests were included in this stiffness testing section. The first test was implemented with beam 1 placed in the designed way, in which the bottom CFRP skin was in bottom side. And in the second test, beam 1 was upside down with the bottom CFRP skin in top side for acquiring the knowledge of bending stiffness in another direction. Therefore, test 1 measured the stiffness of bending downward while test 2 measured the stiffness of bending upward. In addition, the third and the forth were repeated tests of the first two tests respectively. The placement of beam 1 in these four tests is shown in figure 4.2.





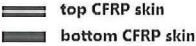
test 1	test 2	test 3	test 4
			
			

Figure 4. 2 Placement of beam 1 in the four consecutive stiffness tests

4.4.2 Beam 2 and beam 3

Stiffness tests were carried out on beam 2 and beam 3 as well. Basing on their performance in the stiffness test, the effect on structural stiffness due to the debonding area can be investigated. It needs to be reminded that beam 2 is same as beam 1 in structure and that beam 3 was fabricated with an artificial debonding area between its bottom CFRP skin and its core.

Four tests with same positioning of the specimen as those in stiffness tests on beam 1 were conducted on beam 2. Beam 3 was planned to have four tests as well. However the two repeat tests (test 3 and test 4) were cancelled due to cracking sound heard during the first two tests. Normally the stiffness test itself should not bring any change to the specimen structure. For the same reason, the second test on beam 3 was limited to small displacements when a clear separation started to appear in the debonding area.

4.5 Results and analysis

Following the format of section 4.3, results of stiffness tests are presented in two sections: results of beam 1; and results of beam 2 and beam 3. And a synthetic analysis section 4.5.3 combines the results of these two sections and describes further calculations and analysis.

4.5.1 Beam 1

The measurement results of four stiffness tests were recorded in pairs of force and displacement. In figure 4.3, the stiffness results of the first two tests, which have different placements of beam

1, are plotted and compared. T1 and T2 denote to test 1 and test 2 respectively.

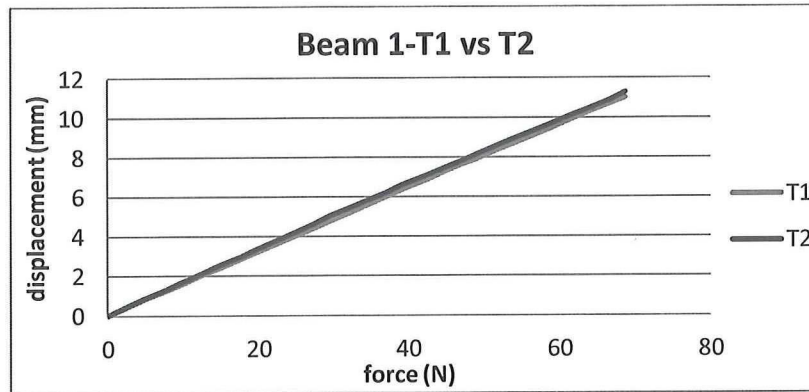


Figure 4.3 Comparison of stiffness in two directions

It is clear in the figure that the lines connecting data points of test 1 and test 2 are highly overlaps, meaning that the stiffness of beam 1 in the two directions are very close. The largest relative difference between displacement results of these two tests is 6.3% and the average difference is 3.6%. The accuracy is 0.01 mm for displacement measurement and is 0.1 N for force measurement. The average error is limited within 2% and the error allowance corresponding to the largest difference is about 4%. Therefore, the difference between results of test 1 and test 2 is not only due to measurement error.

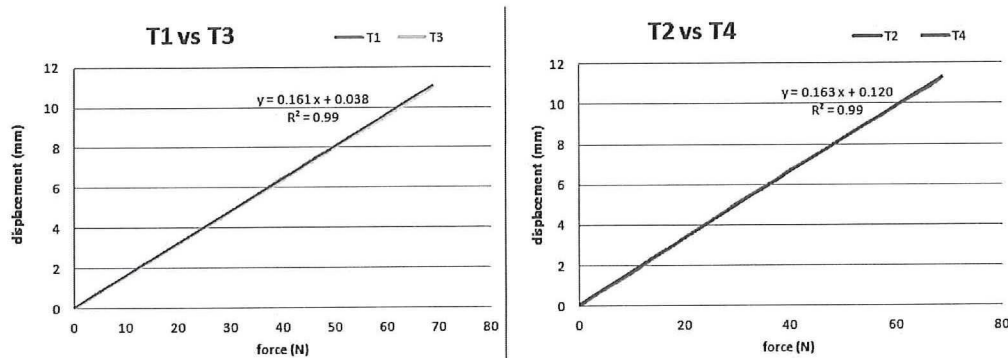


Figure 4.4 Stiffness measurements of beam 1 in two directions

Similarly, T3 and T4 in figure 4.4 denote the third test and fourth test on beam 1 respectively. Comparisons between test 1 and test 3, and between test 2 and test 4 show a high level of repeatability as the data lines almost coincide. The average relative differences in these two comparisons are 0.8% and 0.6%, which are both within the measurement error 2%. Meanwhile the coefficient of determination approaching 1 reflects a high linearity in the result of test 1. This is also true for test 2. Such linearity can be expected due to the fact that deflection of material is proportional with the load within its elastic limit.

Bending stiffness of beam 1 in both the downward and upward directions can be obtained using the slopes in figure 4.4. Furthermore, flexural rigidity and flexural modulus are calculated by substituting measurement results into formulas presented in section 4.3. These calculation results are collected in table 4.1. As shown, the calculation results of the bending stiffness are accurate to 1 N/m. The values of flexural rigidity and flexural modulus can be given to nine

decimal places and one decimal place respectively. Therefore, all flexural modulus values are shown down to two decimal places in a unit of GPa in the table. Flexural moduli of the CFRP material calculated using first method are slightly smaller than those in second method. They are expected more accurate due to a consideration of the contribution from the CFRP side walls, which is excluded from calculations in second method.

	Bending stiffness, k (N/m)	Flexural rigidity, EI (Pa·m ⁴)	Flexural modulus, E (GPa)	CFRP flexural modulus, E _f (GPa)	
				Method 1	Method 2
Test 1	6228	103.36	24.81	101.53	107.26
Test 2	6130	101.74	24.42	99.93	105.58

Table 4. 1 Summary of calculation results for beam 1

4.5.2 Beam 2 and beam 3

Stiffness tests on beam 2 followed same schedule as of beam 1. In figure 4.5, T1, T2, T3, and T4 refer to the four tests on beam 2 in this schedule.

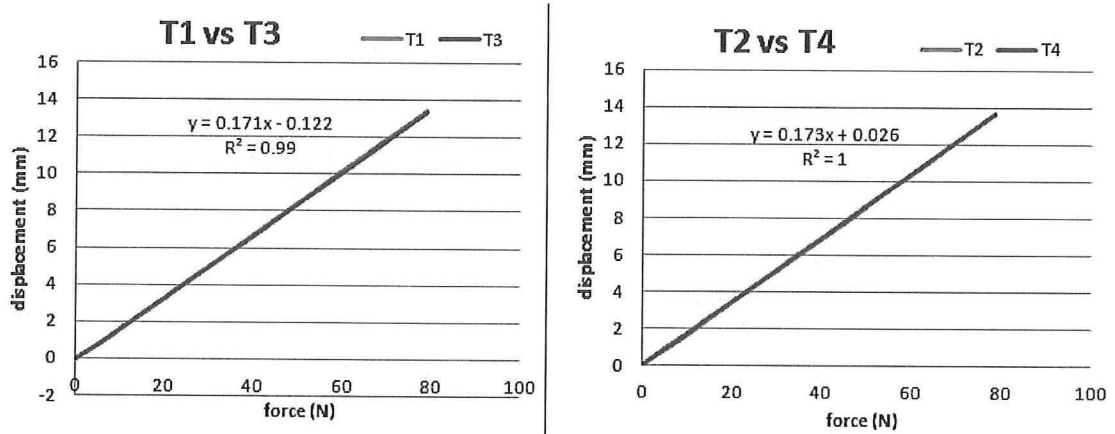


Figure 4. 5 Stiffness measurements of beam 2 in two directions

Lines representing results of repeated tests (test 3 and test 4) strongly overlap with the lines of primary test in both directions. Therefore, measurement results related to structural stiffness can be considered repeatable due to such consistency. Following the same calculation process as used for beam 1, the corresponding values of stiffness, flexural rigidity, and flexural modulus are obtained and shown in table 4.2.

	Bending stiffness, k (N/m)	Flexural rigidity, EI (Pa·m ⁴)	Flexural modulus, E (GPa)	CFRP flexural modulus, E _f (GPa)	
				Method 1	Method 2
Test 1	5852	97.13	23.31	95.41	100.79
Test 2	5777	95.88	23.01	94.18	99.50

Table 4.2 Summary of calculation results for beam 2

A small difference of 1.3% in bending stiffness shows that beam 2 behaves similarly in two directions. Furthermore, in both directions, beam 2 possesses stiffness approximately 6% less than that of beam 1. According to their design, beam 1 and beam 2 are supposed to have identical structure, so this difference in stiffness is caused by manufacturing variations.

No repeated tests are performed on beam 3 in order to avoid growing the debonding area before the experiments with the WSN. So there were only two tests on beam 3 and results of them are displayed in figure 4.6. Test 1 was performed with beam 3 placed with the debonding area beneath the honeycomb core. In test 2, the debonding was located between the upper skin and the core by placing beam 3 on the test rig another way. As shown in figure 4.6, the displacement of the central part of beam 3 was limited within 3 mm in test 2 because a cracking sound was heard when a larger displacement was imposed.

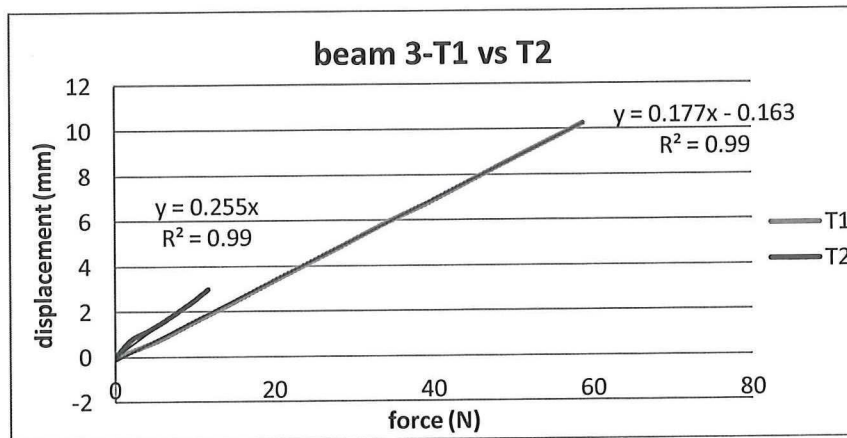


Figure 4.6 Performance of beam 2 in stiffness tests

The stiffness in two bending directions can be calculated from the slopes of the linear regression and their results are presented in table 4.3. In this table, other calculation results such as flexural rigidity and flexural modulus are presented as well.

	Bending stiffness, k (N/m)	Flexural rigidity, EI (Pa·m ⁴)	Flexural modulus, E (GPa)	CFRP flexural modulus, E_f (GPa)	
				Method 1	Method 2
Test 1	5665	94.02	22.56	92.35	97.57
Test 2	3925	65.13	15.63	63.97	67.59

Table 4.3 Summary of calculation results for beam 3

Compared with beam 2, which was produced in the same batch with beam 3, beam 3 has a 3% smaller stiffness of downward bending and a 32% smaller stiffness of upward bending. The loss in stiffness caused by a debonding between the core and the skin is much more severe in the upward bending.

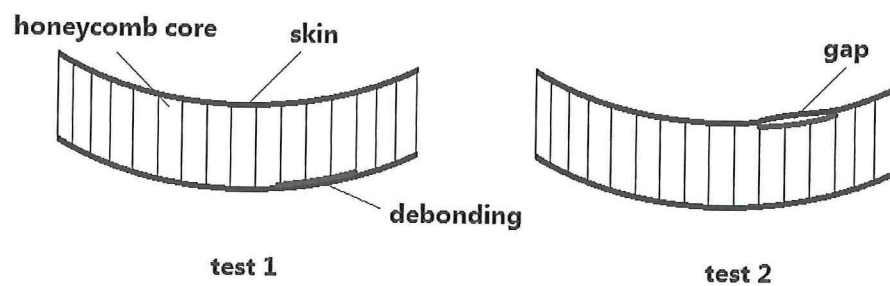


Figure 4.7 Structural behavior at the debonding area in two stiffness tests on beam 3

The schematic plots in figure 4.7 explain this difference in stiffness reduction in two directions. When the debonding was placed beneath the honeycomb core, debonding zone was in tension during downward bending. In the test, the beam was setup upside down to have the debonding on top of the core. With downward bending, the CFRP skin was in compression and separated from the core. The skin buckled at the debonding area with a visible gap present. More significantly, the CFRP skin became partially separated from the two side walls at the same time, damaging the integrity of the CFRP frame, which provided the main bending stiffness. As a result, there was a great loss in stiffness of 32%. In addition, the bending strength of the whole structure was also markedly reduced. This strength reduction is visualized in figure 4.6 by the much smaller load that the complete structure can bear before damage growth was heard.

It is notable that the line of test 2 shows less linearity with a slight variation, in spite of the limited displacement range. As is known, the slope is related to the beam stiffness, so a non-constant stiffness is therefore obtained. The fact that the stiffness changed during bending can possibly be attributed to the local distinct deformation pattern of the CFRP skin and energy consumption of tiny crack growth starting from the debonding ends. However, the average slope still allows an estimation of stiffness due to the coefficient of determination approaching 1.

4.5.3 Analysis

By performing tests with different specimen positioning, the stiffness of specimens in two bending directions was obtained and is listed in table 4.4. The bending stiffness differences in the two directions are 1.6%, 1.3%, and 44.3% for beam 1, beam 2, and beam 3 respectively. The first two values are small enough to consider that beam 1 and beam 2 both possess nearly identical stiffness in the two bending directions. This affirms the fabrication qualities of these two batches. However, with the presence of a debonding area between the honeycomb core and the bottom CFRP skin, beam 3 has a bending stiffness which differs significantly in different directions. As explained in section 4.5.2, this is caused by the different structural behavior at the debonding area.

In comparison of the stiffness between three specimens, though beam 1 and beam 2 are identical in design, stiffness of beam 2 is 6% smaller than of beam 1. This is attributed to manufacturing variations since these two specimens were fabricated in two batches. Stiffness of beam 2 and beam 3 are compared in order to evaluate the influence of debonding. Debonding was found to bring a 3% reduction in downward bending and a 32.1% reduction in upward bending.

	Beam 1		Beam 2		Beam 3	
	Stiffness (N/m)	CFRP modulus(GPa)	Stiffness (N/m)	CFRP modulus(GPa)	Stiffness (N/m)	CFRP modulus(GPa)
Downward bending	6228	101.53	5853	95.41	5665	92.35
Upward bending	6130	99.93	5778	94.18	3925	63.97

Table 4. 4 Collection of stiffness test results

The flexural modulus of the CFRP material for each specimen is obtained by following an approximate calculation process described as method 1 in section 4.3. By only considering a downward bending, results for beam 1, beam 2 and beam 3 are 101.53 GPa, 95.41 GPa, and 92.35 GPa respectively. They are all smaller than the reference value of 125 GPa for similar materials (3). The factors of fiber properties, fiber volume, and cure temperature are possibly the reason for such a difference. It is obvious that beam 2 and beam 3 possess similar flexural modulus of skins since they were fabricated in one batch. It is important to note that the flexural modulus is only related to the material. Therefore, modulus should be identical no matter in which direction the bending was imposed. This seems not to be true for beam 3. It is because in the calculation, structural factors were converted into a material degradation by assuming the structural integrity was retained. For the same reason, the downward bending modulus slightly differs on beam 2 and beam 3. However, it is still reasonable to use these calculated moduli of beam 1 and beam 2 to evaluate the actual properties of CFRP material.

4.5 Summary

Stiffness measurements were performed to acquire an understanding of the specimens' basic properties by using a stiffness test setup, in which a spiral elevator generated curvature, a load cell measured imposed forces, and a dial comparator detected the curvatures. Tests of beam 1 and beam 2 consisted of four sections with two different specimen placements. Considering factors due to the debonding area, beam 3 was tested according to a simplified schedule without repeated tests.

Based on measured results, calculations were carried out to obtain the stiffness of the three specimens. Manufacturing variations between the two batches resulted in a 6% difference in stiffness between beam 1 and beam 2. And it was found that the debonding brought about a 3% reduction in downward bending stiffness when comparing the stiffness of beam 2 and beam 3. Due to different local structural behaviors, stiffness loss in the opposite bending direction was much more significant. The flexural moduli of the CFRP material of specimens were calculated as well. Because the calculations were based on some assumptions, which are completely true in experiments, values of flexural modulus can be used as a reference to roughly evaluate the material properties.

4.6 References

1. Chen W F. Handbook of structural engineering. Crc Press, 1997.
2. Deshpande. The design of sandwich panels with foam cores. Cambridge University, 2002.
3. Toray. Standard modulus carbon fibers [cited 2015 January 30th]. Available from: <http://www.toraycfa.com/standardmodulus.html>

Chapter 5

Static Test and Slow Dynamic Test

5.1 Introduction

A series of static tests were performed on three specimens to prove the validity of the WSN and to further characterize the specimens. The static test involved elevating the specimen tip to certain height and holding it at this position to perform a measurement of target parameters such as strain, force and displacement. During the slow dynamic tests, the same parameters were measured when specimens were driven in slow speed motion, which are at frequencies lower than 1 Hz. It is possible to investigate dynamic effects on the structural performance in the slow dynamic tests. These two experimental sections are combined in this chapter because they were applied using an identical test setup and performed in same test environments.

5.2 Test setup

In the static and slow dynamic tests, the specimen was positioned horizontally with its tip fixed to a strain gauge load cell with sticky tape and its root part tightly clamped by the mounting structure. A motion command given by software on PC was transmitted by a controller to a linear actuator, which is shown in figure 5.1, generating the specified displacement of the specimen tip. The displacement can be acquired via a reverse transmission from an integrated sensor in the actuator back to PC. As mentioned, the load cell was placed between the tip of the actuator and the specimen tip to measure the load exerted on the specimen. The load cell converted the strain to a voltage, which can be read from an amplifier.

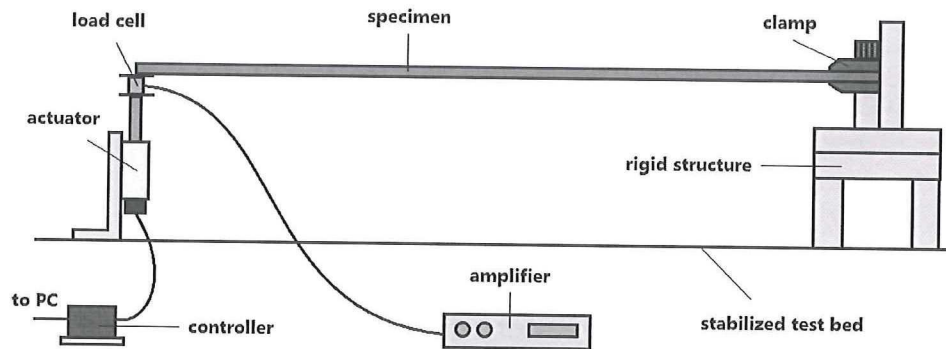


Figure 5. 1 Schematic diagram of test setup for static tests and slow dynamic tests

As the main composition of the measurement system, a wireless sensor network (WSN) was established for measuring real-time local strains, accelerations, and the temperature. The mounted strain gauges were integrated into bridge circuits and the circuits were connected to wireless sensor nodes, two V-Link-LXRS sensor nodes, which also have integral temperature sensors inside. Subsequently, the sensor nodes operated a continuous wireless data transmission to the base station, which is connected to a PC. In addition, a G-Link-LXRS sensor node was attached on the specimen tip and functioned as a wireless accelerometer.

The linear actuator NA23C60-T4 was used to accurately position the specimen tip with the required displacements or dynamic motion. This actuator from ZABER possesses a 60 mm travel range and a continuous thrust up to 950 N. Its motor type is a 2-phase stepper with a micro-step size about 0.2 μm . Operating with a maximum speed of 50 mm/s and an accuracy of 36 μm , the linear actuator is able to provide a precise positioning and motion speed in static tests and dynamic tests which involve relatively slow motions. An A-MCA stepper motor controller (ZABER) was connected to the actuator to transmit the motion command to desired position and speed. Also, the real-time position and the real time condition of actuator were reported to PC by the controller. A convenient manual control is also possible by using an indexed knob on the controller: speed and position can be adjusted with increment of the knob and a stop command can be executed when the knob is depressed.

To mount the actuator, a specially designed frame was made using Alufix components. This allows a rigid mounting to the optical table and makes the motion axis perpendicular to the table surface. The mounting frame and the connection means are shown in figure 5.2 (a). And the mounting structure for the other end of specimen was built on the optical table. Because of the clamping device being integrated in the structure, the root part of the specimen was firmly fixed to the structure. The clamping fixation can be loosened and retightened easily when replacing specimens. The mounting structure and the clamping mechanism are shown in a picture in figure 5.2 (b).

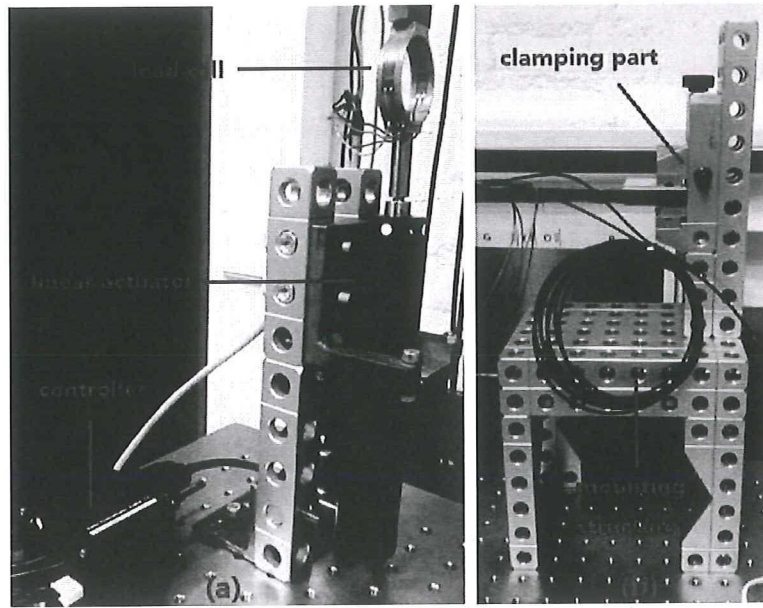


Figure 5.2 Actuator setup (a) and mounting structure (b)

5.3 Experiment

The experiment descriptions are divided into two sections according to the two groups of tests: static tests and slow dynamic tests. Static tests were performed on all three specimens while the slow dynamic tests were only performed on beam 1.

5.3.1 Static test

The static test was defined as having the specimen tip displaced in steps from height of 0 mm, to 45 mm and then driven back to 0 mm. During this one cycle, the tip stopped at heights of 5 mm, 10 mm, 15 mm, etc. and data were measured at these heights. Including the 0 mm and 45 mm, there were ten height positions involved in the static test. The measurement system performed during the whole process of one cycle by means of the WSN, the actuator sensor, and the load cell. By extracting valid data from measurement recordings in PC and conducting analysis, valuable conclusions can be obtained as described below. The section of static tests is described in two sub-sections according to different specimens and experimental procedures.

5.3.1.1 Beam 1

There are several parts of the static tests on beam 1: the pre-tests and the main tests. And they are described here in detail due to differences in test objectives and experiment setups. A summary of these tests is given in table 5.1 and each test will be described below in detail.

	Pre-test 1	Pre-test 2	Pre-test 3	Main test	Additional test
Target	Measurement system	Accelerometer attachment	Holding time	Strain, force	Multiple motion cycles

Table 5.1 Summary of static tests for beam 1

Firstly, in order to verify the functionality of the wireless sensor network, a wired system incorporating a multi-channel National Instrument strain gauge card NI9219 and a LabVIEW control program was operated to obtain reference data under an identical condition. Acquired strain data through these two different transmission means were then compared.

Secondly, since the wireless accelerometer was mounted on the specimen tip and its mass was not negligibly small, the structural responses with and without this accelerometer needed to be compared and analyzed. For such a purpose, comparative trials were carried out and the influence of the wireless accelerometer attachment was evaluated.

The third pre-test aimed at investigating the effects of holding time at each height. The dynamic disturbance caused by actuator motion was excluded by holding the specimen tip at each height for a period of time before recording data. Because the holding time was supposed to be sufficient for accurate measurements but not excessive in order to maintain a high efficiency, there was a need to investigate the influence of holding time on the measurement outputs. Therefore, two testing cycles were undertaken with the holding time (1.5min and 5min) as the only variable.

For the main part of static tests, the relationship between force and displacement and the relationship between strain and displacement were studied by recording data while changing tip height. Theoretically, the bending strain should be proportional to the distance between tip and the measuring point: $\varepsilon = \frac{FL}{EZ}$, where ε , F , L , E , and Z denotes bending stress, force, distance to the tip, flexural modulus and section modulus respectively. In order to verify this, the strain values were measured by the strain gauges at 0.9 m and 1 m location respectively. By multiplying the strain at the 1 m location by a factor of 0.9, the theoretical value can be obtained, which was compared with the actual measurement value at 0.9 m location. In addition, shear strains are expected to be same along the specimen length when a vertical force is exerted on one end. So similar to the case of bending strain, the verification can be accomplished by measuring shear strains at two points. The shear strain at 0.22m from the tip was obtained by using mounted strain gauges. By placing beam 1 with its tip clamped and its root attached to the load cell, shear strain at 0.98 m can be measured during one cycle as well. With such test it was possible to further verify the measurement systems, especially the WSN, which is the fundamental part in the proposed wireless SHM system.

In addition, the effect of multiple motion cycles was considered by operating a four-cycle-test and looking into differences compared to the one cycle test. The parameters involved in this comparison were strain and force. As mentioned in section 3.3.2.2, a temperature sensor was integrated inside a V-Link-LXRS sensor node. This data channel was activated in all tests to collect

environment temperature data during the testing process. Since temperature variations can have an influence on the grid length of a strain gauge, which is supposed to be changed only by material deformation, the range of environment temperature needed to be well known. The strain measurement can be regarded as reliable only when the temperature range is limited. Temperature data also allows a check whether strain gauges stay within the required range for the automatic temperature compensation (10 °C to 100 °C).

5.3.1.2 Beam 2 and beam 3

Basically, static tests on beam 2 and beam 3 both shared same setup with the main part of the static tests on beam 1. As described above, in the setup, ten different height positions of specimen tip were controlled by the actuator. Motion commands given by PC, passed through controller, were implemented by the actuator to allow the tip move from one height to the next. The holding time at each height was determined by results of the third part of beam 1 static tests. Parameters of strain, acceleration, temperature, force and displacement were measured by the WSN and other measuring devices during one cycle, in which the specimen tip was elevated to 45 mm and dropped back to 0 mm. Two groups of transverse comparisons can be undertaken: the repeatability of the static test was evaluated by looking the results from beam 1 and beam 2; the way the debonding effecting structure health was also explored to some extent. In addition, recordings of the specimen performance in the static tests allowed a more reliable discussion later when the dynamic factors were involved.

5.3.2 Slow dynamic test

As proposed in chapter 1, the main method adopted in this thesis is simulating the flapping conditions of the blade by offering the specimen a dynamic motion and then evaluating the WSN. Flapping is a movement in which a helicopter rotor blade climbs upwards and tilts downwards. During forward flight, the advancing blade meets a higher airspeed because of the addition of flight velocity to the rotational speed of the rotor blade. According to the knowledge of aerodynamics, the increase of airspeed produces more lift and the advancing blade, hence, flaps upwards. The opposite condition occurs on the retreating blade which experiences a downward movement while rotating. It is worth mentioning that such lift imbalance is solved by a change in the angle of attack, which is related with blade torsion. However, it was not possible to include torsion movement in the experiments performed.

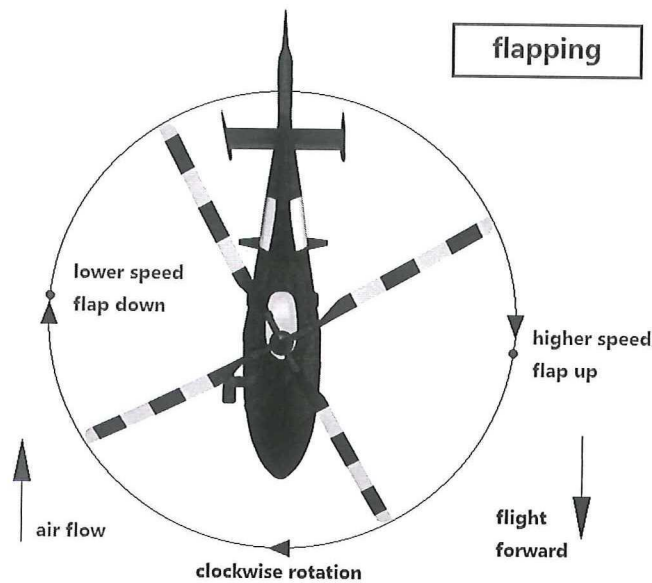


Figure 5.3 Dissymmetry of lift causes blade flapping

Given the flapping mechanism, it is also known that the rotor blade flaps upward and downward once in one rotation, as shown in figure 5.3. Therefore, the flapping frequency can be determined by the rotor rotation frequency. When the R22 helicopter is in normal operation, the rotor speed is kept in a range from 495 revolutions per minute (RPM) to 530 RPM. This speed range corresponds to a flapping frequency range from 8.25 Hz to 8.83 Hz. So a frequency of 8 Hz becomes a critical indicator in the effort of simulating flapping. Limited by the maximum speed of the actuator of about 50 mm/s, dynamic motion at a frequency of 8 Hz could not possible to be achieved with this linear actuator. However, a series of dynamic tests on beam 1 with relatively slow motion were conducted for the purpose of getting a preliminary understanding of dynamic response of the specimens.

There were two main sections in slow dynamic tests. First a section of tests were performed with the designed setup the same as the one used in static tests. In the second section, beam 1 was placed in the other way around with tip and root reversed. By simply changing the way of mounting beam 1, acquired data ready for analysis was doubled without changing the strain gauge layout. In each section, tests performed at five different frequencies: 0.1 Hz, 0.3 Hz, 0.5 Hz, 0.8 Hz, and 1 Hz. Due to the speed and acceleration restrictions of the actuator, the latter two groups had a travel range of 20 mm instead of 45 mm. In order to obtain a reliable measurement, programs with ten cycles at each given frequency were run and implemented by the actuator. Combining measurement results from these two test sections, it was possible to obtain bending strains at four locations and shear strains at two locations during slow cyclic motion. In each section, a standard static test was conducted again to exclude the impact of different initial conditions in the comparative analysis. In these slow dynamic tests, a sampling rate of 32 Hz, which was higher than the 4 Hz for static tests, was employed for wireless data transmission.

5.4 Results and analysis

5.4.1 Static test

Static test results are presented in testing order. Therefore, measurement results of the static tests on beam 1 are shown in first section and results from beam 2 and beam 3 are given in the second section. In addition to the standard static part, measurements in comparative trials targeted to measurement system, sensor attachment, and holding time are also included in first section since they were performed on beam 1.

5.4.1.1 Beam 1

Since the static test on beam 1 comprised several parts, the experimental results are shown depending on the measuring sequence. First, the WSN was tested by comparing its output with that of a wired system incorporating a multi-channel strain gauge card and a LabVIEW control platform.

In figure 5.4, measurements of (a) bending strains and (b) shear strains obtained from two measurement systems are compared. NI stands for the wired system supported by National Instrument strain cards and WSN is the abbreviation for the wireless sensor network. In these two comparison groups, correlation coefficients between two data sets are both very close to 1, meaning that the relation between displacement and strain is the same with the WSN and the wired system. The maximum relative differences for bending strain and shear strain are 5.2% and 4.1% respectively, which are small enough to conclude that wireless sensor network functions as accurate as wired system in strain measuring. It is important for latter experiments to ensure the wireless sensor network's capability of implementing the reliable real-time measurement.

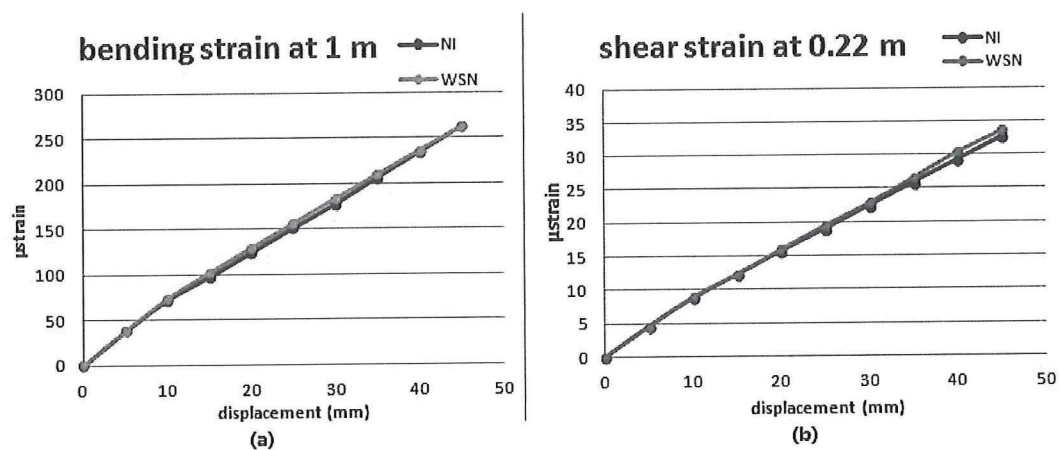


Figure 5.4 Comparison of (a) bending strain and (b) shear strain measured by two measurement systems for beam 1 in pre-test 1

Secondly, the influence of sensor node attachment on structural response was estimated by a

group of comparison tests. In some tests, especially the dynamic ones, a G-Link-LXRS sensor node with a 40 g mass was fixed on the specimen tip during measurements. Therefore, the parameters measured with and without the sensor node attachment needed to be compared. These are shown in figure 5.5, where a red line and a blue line refer to the measurements with and without the sensor node attachment, respectively.

As in the first sub-section, relative difference was calculated to evaluate the influence of sensor node weight on specimen. The values for bending strain and shear strain are 6.0% and 7.6%, which can be considered to be small. It is shown that the strain has small increment when a sensor node is placed above the specimen. This can be explained by misalignment between the loading line and the gravity line of the sensor node or by the fact that the size of sensor node is not small enough to be considered as a mass point exerting force above the specimen. However, sensor node attachment on specimen tip nearly has no influence on the strain measurement and this factor can be ignored in the latter tests.

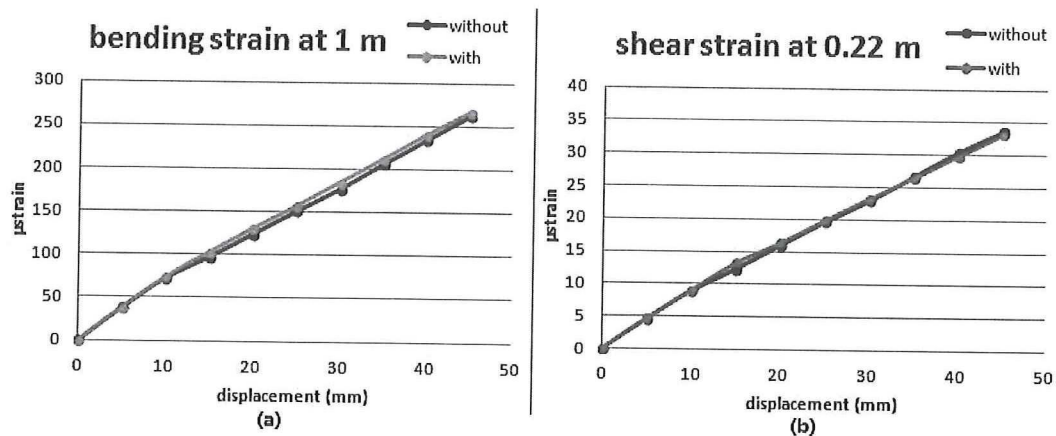


Figure 5.5 Comparison between conditions with and without sensor node attachment for (a) bending strain and (b) shear strain for beam 1 in pre-test 2

Thirdly, measurements were undertaken with 1.5 min holding time and 5 min holding time at each height in order to determine an optimized holding time for the standard tests. Recordings of these two measurements with different holding times are plotted in one graph in figure 5.6. It is shown that at each height, strain values fell with a small amount when the position was hold for a longer time. This phenomenon can be explained by following the factors: dynamic effects of actuator movements, clamp loosing, and certain slow changes in CFRP material behavior. However, actuator movements were supposed to bring an influence only when the specimen tip has just reached the height. Although the decreasing strains can neither be included in stress relaxation nor creep, it was still possibly caused by the material behavior. A minor change in clamp is also a possible reason. In addition, the stiffness of the composite specimen is not perfectly consistent along the span and a balanced stress distribution may not be reached in a very short time. Because of clamping factors or material and structural behavior or both, a larger strain drop is observed at a larger height in figure 5.6. The second finding is that the strain became nearly constant after holding the specimen tip for a certain time. Only taking the recording line of 5 min holding time into account, no obvious strain change was found after 1 min. Therefore, the strain measurement results turned out to be similar even though the holding time

was different.

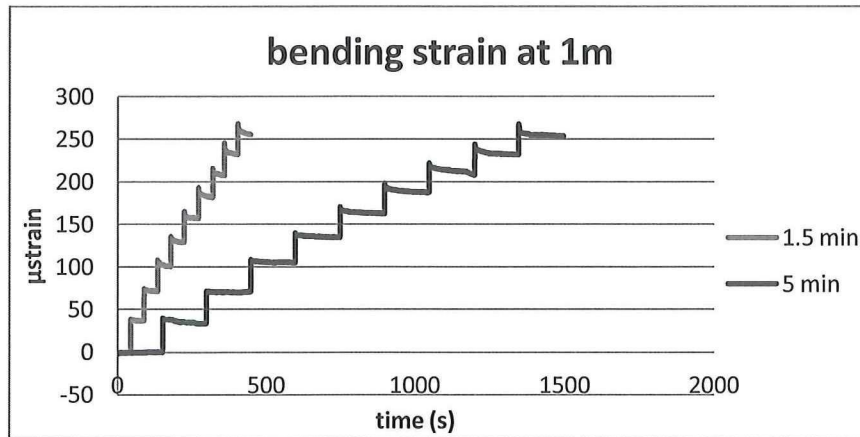


Figure 5.6 Recordings of bending strain with different holding time

By extracting and processing the valid data, the last ten stable data, lines presenting the relationship between the tip displacement and the strain value were plotted and compared in figure 5.7. As shown in the figure, compared with the results obtained from measurements with a 5 min holding time, the lines representing the holding time of 1.5 min is closer to a straight line, which can be proved by their higher correlation coefficient to a linear trend line. The line crossing in figure 5.7 shows a worse linearity for the line of 5 min holding time. For strains at a few heights, measurements with longer holding time had higher values. This was due to the fact that variations in experimental condition can be introduced in repeating a test, even though they were performed sequentially. In addition, the maximum relative differences between measurements with two different holding times for bending strain and shear strain are 10.4% and 15.4% respectively. Considering all the factors mentioned above, it can be concluded that extending the holding time to 5 min has negligible effect about and 1.5 min is sufficient as a standard holding time.

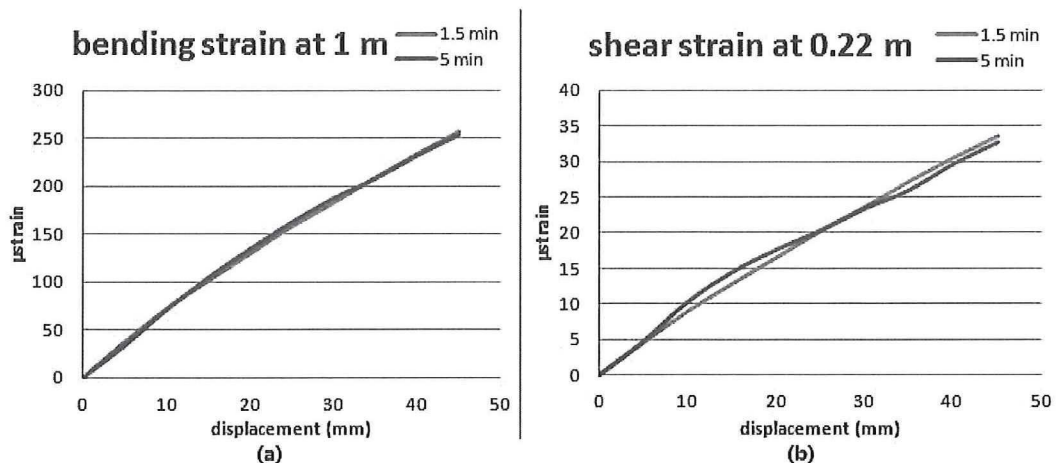


Figure 5.7 Comparison of (a) bending strain and (b) shear strain measurements with different holding times

The main part of the static tests on beam 1 was carried out to acquire actual strain levels for the beam and to investigate the relationship between strains at different locations along the

specimen. In theory, the bending strain is proportional to the distance to the beam tip. Therefore, measured bending strain at 1 m can be multiplied by a factor of 0.9 and compared with the strain measured at 0.9 m. In figure 5.8, the blue line denotes the theoretical value and the red line represents the measured value. The relative difference for these two set of data is within 3%, which is small enough to reach the conclusion that there is no difference between them. As a result, the proportional relationship between strain and distance along the beam is proved.

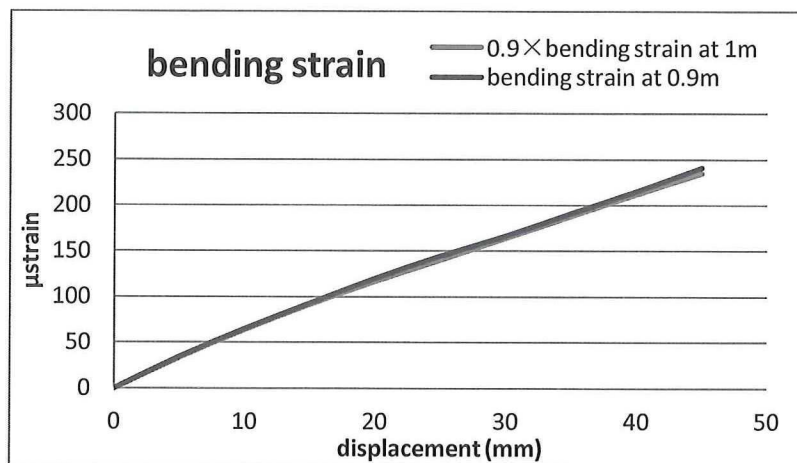


Figure 5.8 Relation between bending strains at different locations

In addition, shear strains are supposed to be identical along the specimen in the static test conditions, in which a vertical force is imposed on the specimen tip. This theory can be verified again by measuring shear strains at two locations: 0.22 m and 0.98 m from tip. As for the situation of bending strain, in figure 5.9, two lines representing shear strain measurement at two locations almost overlap, which also can be confirmed by a variation of 3%. The small difference may be mainly attributed to different setup conditions in these two measurements since the measurement at 0.98 m was performed by swapping the tip and root ends of the beam. Such a change in test setup has more influence for shear strain measurements, which involve relatively small absolute values.

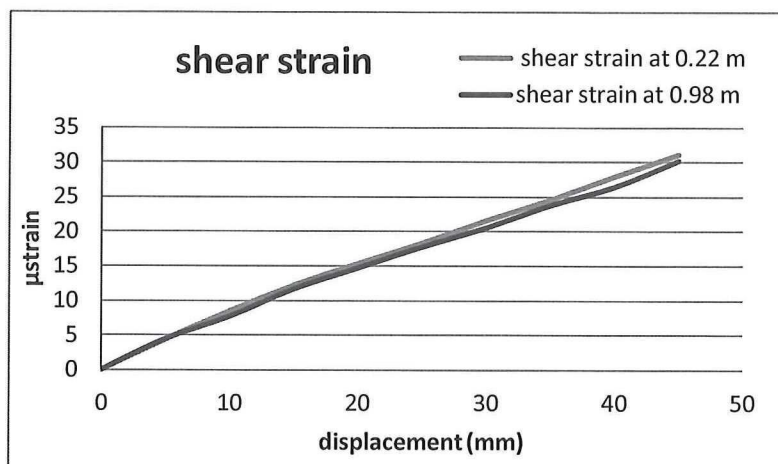


Figure 5.9 Comparison of shear strains at different locations

In the standard static tests, the specimen tip was displaced from its initial position to its highest

position step by step and then moved back passing same height steps. This was defined as one cycle of static test. The specimen performance in multiple cycles is required to be evaluated as well and this was realized by analyzing the data recorded during a four-cycle test. It can be seen in figure 5.10 that one 'loop' is formed by the strain recording in first cycle and the other one loop represents the overlap of data from the next three cycles. The first one can be regarded as one part of a typical hysteresis loop since the final strain is smaller than its initial strain. This shift is due to the fact that the deformation was not completely elastic. But this phenomenon cannot be seen so clear in the following cycles. It is also shown in the figure that strains measured at the same height but in latter cycle had lower values, which could be the result of lower initial strain levels. It suggests that hysteresis phenomenon still existed in last three cycles although it became indistinct. However, the difference in measurement results between first cycle and last cycle was small and negligible, especially when the peak value of strain was targeted for further analysis.

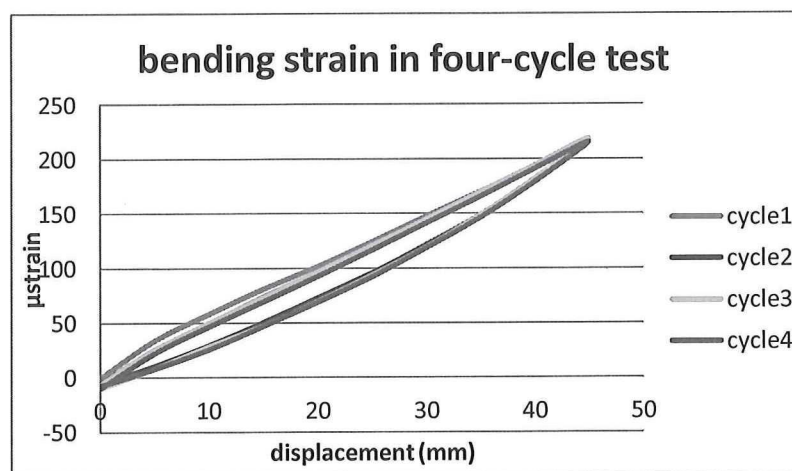


Figure 5.10 Strain recording during a test with multiple cycles

The hysteresis effect is more evident in the force recording during the four cycles, which shows a classic hysteresis shape in each cycle. Again, starting from the second cycle, the shift after one cycle movement became much smaller. Therefore, based on both of the strain and force data, it can be considered that four cycles are sufficient and that further cycles would have limited effects on the measurement.

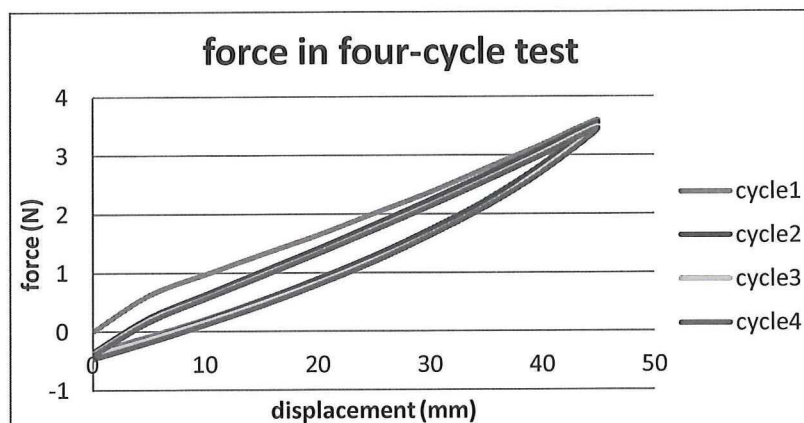


Figure 5.11 Force recording during a test with multiple cycles

The channel connecting with integrated temperature sensor inside the V-Link-LXRS sensor node was activated to perform a temperature recording throughout the static test. It was found that there was only little variation of temperature with a range from 24.6°C to 24.9°C. This proves that the strain gauges were operated in a well controlled environment, which is critical to ensure an accurate strain measurement.

5.4.1.2 Beam 2 and beam 3

Similar to the beam 1 tests, beams 2 and 3 were mounted in the static test setup and connected with the WSN to perform measurements. Because the verification of measurement system and basic understanding of the structural response of the manufactured beam were achieved by the test on beam 1, data processing and analysis in this section was focused on identifying differences induced by the artificial defect, which is a debonding between the bottom CFRP skin and the core structure.

5.4.1.2.1 WSN noise signal

There were obvious noise peaks in the data collected from the WSN when static tests were carried out on beam 2 and beam 3. Noise frequencies and their relative intensity was obtained by Fast Fourier Transform (FFT) analysis of the signals. When the sampling rate of the measurement system was set to 64 Hz, two clear noise frequencies were found about 6 Hz and 14 Hz. In figure 5.12, these two noise peaks are displayed as two peaks in frequency domain. The main noise at 14 Hz was as four times severe as the secondary noise at 6 Hz. So the comments below refer to the main noise peak at 14Hz. The average magnitude of the main noise peak is close to 40 μ strain and did not appear in the previous static tests for beam 1. Although employing the same test setup, the static tests performed on beam 2 and beam 3 had one difference in the bridge circuits containing the strain gauges.

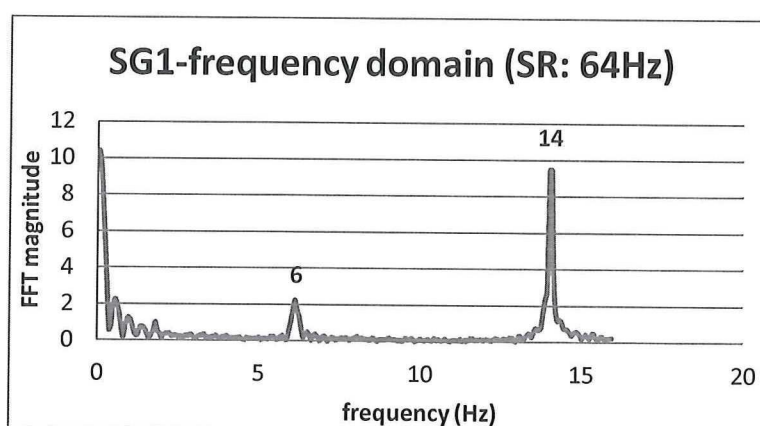


Figure 5. 12 Data of strain gauge 1 in frequency domain with 64 Hz sampling rate

As described in section 3.2.2.2, ten strain gauges on beam 1 were integrated into two full bridges and one half bridge before connecting to the WSN in order to achieve temperature compensation. Differently, the placement of strain gauges on beam 2 and beam 3 was specially designed for

detecting the influence of debonding. Six quarter bridges were needed to integrate the strain gauges into the WSN. Different from a standard quarter bridge, each bridge configuration included two kinds of electrical resistors. Due to a current limitation in wireless sensor node, two $10\text{ k}\Omega$ resistors were used to complete half of a bridge, which then used almost no current. Because of different electrical bridges, the noise is firstly identified as an electrical noise. In addition, the noise was present in all data from channels of strain gauges but not from the one of the temperature sensor, which also supports this judgment. Considering the static condition, the sampling rate was then set to 8 Hz in the formal tests. Nevertheless, a noise at 2 Hz instead of the 14 Hz peak existed in the strain data transmitted to PC and is shown as the only peak in figure 5.13.

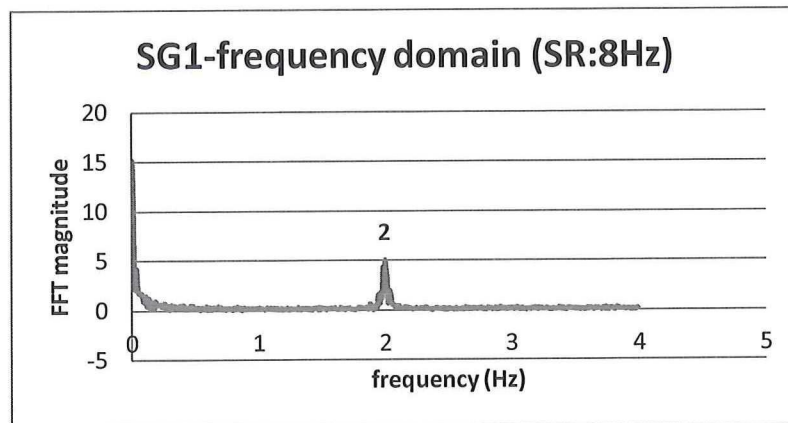


Figure 5. 13 Data of strain gauge 1 in frequency domain with 8 Hz sampling rate

Actually, this noise at 2 Hz is an aliase of the real noise at 14 Hz and it appears because of the reduction of sampling rate. The aliasing phenomenon can be observed when the sampling rate is smaller than twice of the frequency of target signals. In this case, the sampling rate was even smaller than the noise frequency, so aliasing occurred and resulted in a 2 Hz signal. It can be explicitly explained by figure 5.14, in which the noise at 14 Hz was sampled with a sampling rate at 8 Hz and was identified as a noise at 2 Hz. To clarify, figure 5.14 is provided for illustrating aliasing and all data involved except frequencies are fictitious. In the figure, a blue solid line represents the original signal and a red dashed line represents the aliase at 2 Hz. Yellow points are measured points, from which the aliased signal was obtained. Therefore, the actual noise at 14 Hz can be confirmed and will affect the measurement with 8 Hz sampling rate by aliasing. In addition, the secondary noise at 6 Hz was also turned out to be an aliased signal at 2 Hz when it was sampled at 8 Hz, which contributed to the noise intensity at 2 Hz.

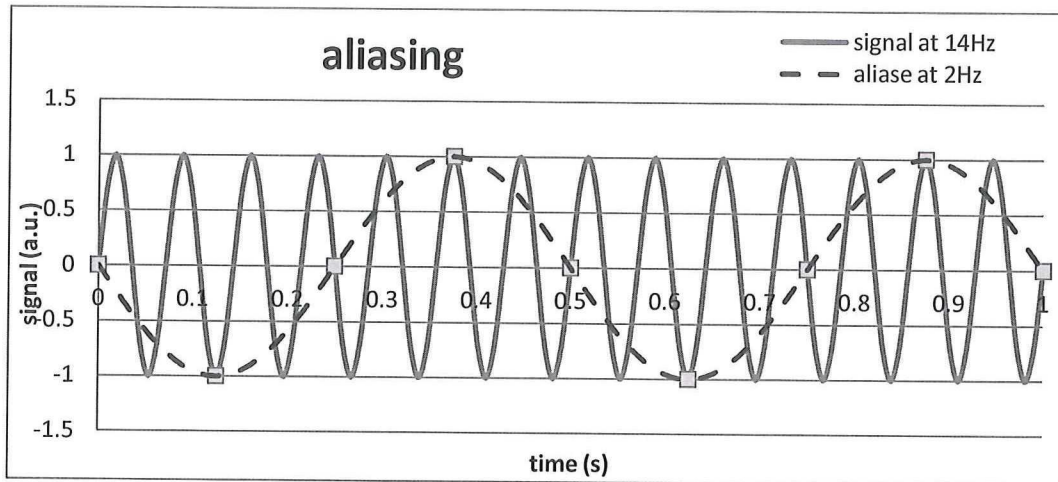


Figure 5.14 Aliasing of noise signal

Several methods including shortening wiring in the system as much as possible, ensuring good connections, and integrating bypass capacitor over the resistor of $120\ \Omega$ were employed to improve the signal-to-noise ratio. For certain strain gauges, the noise level can be brought down to $20\ \mu\text{strain}$, which is still unacceptable, especially for shear strains. According to experience, noise at such a low frequency can be caused by mechanical resonances. However, this assumption can be denied in this case by the high stability of the optical table test platform and the reference tests on beam 1. This noise should not be considered part of the structural response since measurements of beams 2 and 3 were similarly subjected to this noise in spite of the artificial difference in their structures.

5.4.1.2.2 Strain

Theoretically, beam 2 has same stress distribution during static test as beam 1. Some variation may exist in measured data due to manufacturing differences. Because such variation is supposed to stay within acceptable limits, data from beam 1 can be used as a reference in this analysis phase. Most significantly, measurement of beam 3 provided some understanding of change in stress distribution induced by the debonding.

Similar to the static tests performed on beam 1, data measured by strain gauges at each height were recorded for beams 2 and 3. For instance, the data of bending strain measured by strain gauge 1 on beam 3 in a complete cycle are shown in figure 5.15. For both cases of beam 2 and beam 3, the bending strains measured by all four strain gauges changed with the changing displacement in a predictable way. It can be seen that bending strain was highly proportional to tip displacement even though the debonding area existed as a defect on beam 3. Note strains for strain gauge 1 on beam 3 were negative as the top of the beam is under compression during loading.

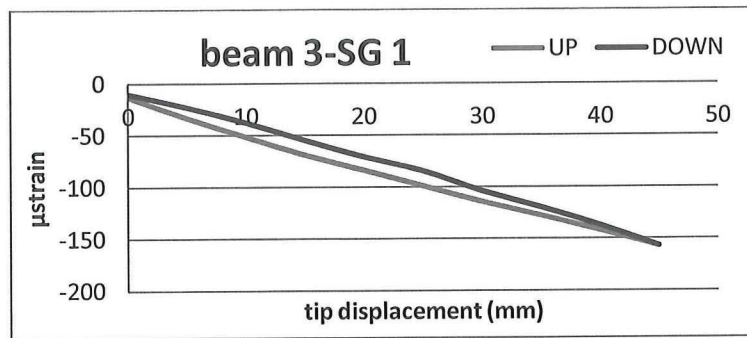


Figure 5.15 Bending strain recording of strain gauge 1 on beam 3

After following the previously described data processing scheme, lines of shear strain here show less linearity, which probably was due to the noise effect for relatively low strain levels. The plotted lines in figure 5.16 fluctuate around the expected straight line. This fluctuation was also possibly induced by the existence of debonding area, but this conclusion remains controversial because similar but milder waves were observed on beam 2. Since there were no special findings in changing trends of strain for each strain gauge, further analysis focused on relations between different local strains.

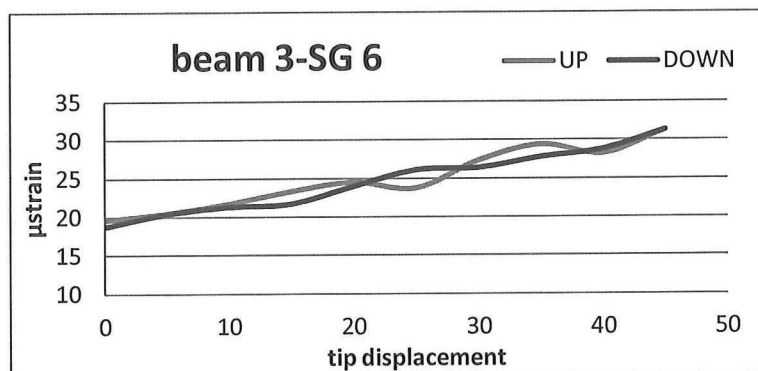


Figure 5.16 Shear strain recording of strain gauge 6 on beam 3

It is worthwhile to be reminded of the placement of strain gauges on beams 2 and 3, which is shown in figure 5.17. Strain gauge 1 was placed on the top surface at a location 50 cm from tip, while strain gauge 3 was at same location but on the opposite surface. Another two strain gauges for measuring bending strains, strain gauge 2 and strain gauge 4, were located 1 m from tip. Similarly, their positions were on top skin and bottom skin respectively. The last two strain gauges were both attached to the CFRP side walls, acquiring data of shear strains, but at two different locations.

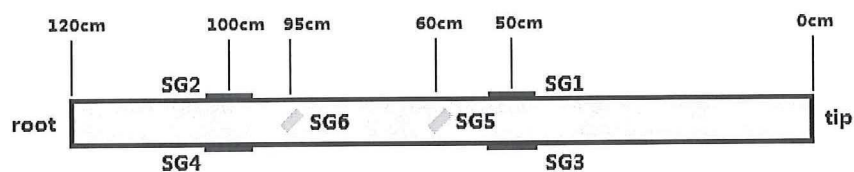


Figure 5.17 Strain gauge layout on beams 2 and 3

The ratio labeled as the unit of vertical axis in figure 5.18 is a result of dividing data from corresponding strain gauge by that of strain gauge 1. Data for this calculation were measured when the specimen tip was at height of 45 mm. As setup variation, especially the replacement of specimen may bring influence on the overall strain levels, relative values were used instead of absolute values. Therefore, ratio is specially defined was used to reveal the relationship between local strains and to represent changes in measurements of two beams at same location, excluding factors of test setup.

It is shown in figure 5.18 that ratio values for strain gauge 2 on both beams are about 2. This is supported by the theory that bending strains have a proportional relation with distance to tip. Because this double relation between strains at 50 cm and 1 m was also true for beam 3, any influence of the debonding on bending strains can hardly be recognized. The same situation can be seen from strain gauges 3 and 4. It is worth noting that strain gauges positioned on the bottom surface measure lower strains than the strains on top surface although they supposed to be same according to theory. This may be explained by different flatness of top and bottom surface, which was caused by production constraints. The top surface was under high pressure from one side during bonding, and had a worse flatness than the bottom one. As a consequence, the stress was not distributed as well as on the bottom surface and stress in the middle position where the strain gauge was placed was higher than the rest. On the bottom surface, the measured strain in the middle was roughly equal to the average strain and was found to be little less than that measured on the top surface.

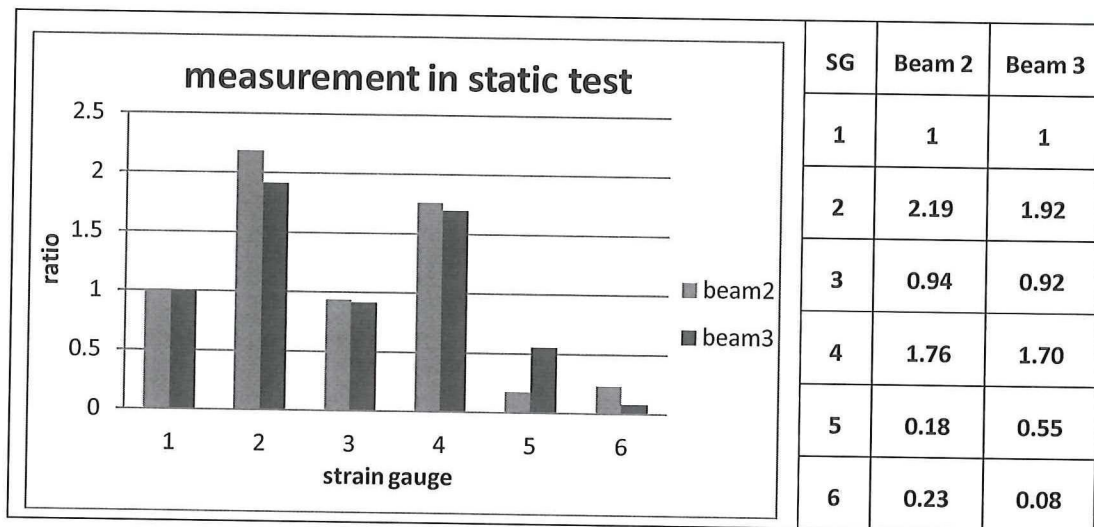


Figure 5. 18 Comparison of strain ratios between beam 2 and beam 3

In comparison between the two specimens, it was found that the ratio of strain gauge 2 on beam 3 is slightly smaller than that on beam 2. If the ratio between data of strain gauge 4 and strain gauge 3 is calculated, this ratio is also slightly smaller. The effects of debonding may be the reason for such a reduction since the existence of the debonding area interfered with the distribution of bending stress and strain. However, the difference is not evident enough to be considered as an indicator of the debonding, especially for the group of strain gauges 3 and 4. Fortunately, the influence of debonding was clear for the measurement of shear strains. It is shown in the last two groups of columns in the figure that strain gauges 5 and 6 have similar ratios on beam 2 while for beam 3, the ratio of strain gauge 5 is remarkably higher than the one

of strain gauge 6. The theory that shear strains are same along the beam is once again confirmed by the result of beam 2. On beam 3, compared with shear strain of strain gauge 5, strain gauge 6 measured an 85% less strain. It is reasonable to attribute this 85% reduction to the debonding ahead of strain gauge 6. This inference was supported by obvious differences between shear strains of strain gauges 5 and 6 when repeating the tests on beam 3. As a result, the approach of comparing shear strains measured at the two sides of the debonding area makes it highly possible to provide valuable information regarding to the debonding.

5.4.1.2.3 Load

With the specimen tip positioned at each height, the force between the actuator and the specimen was recorded by a load cell and can be read from an amplifier. Therefore, the force history in one cycle was obtained for beams 2 and 3. For each specimen, two sets of data were recorded to check measurement accuracy. The load histories for both specimens are included in figure 5.19.

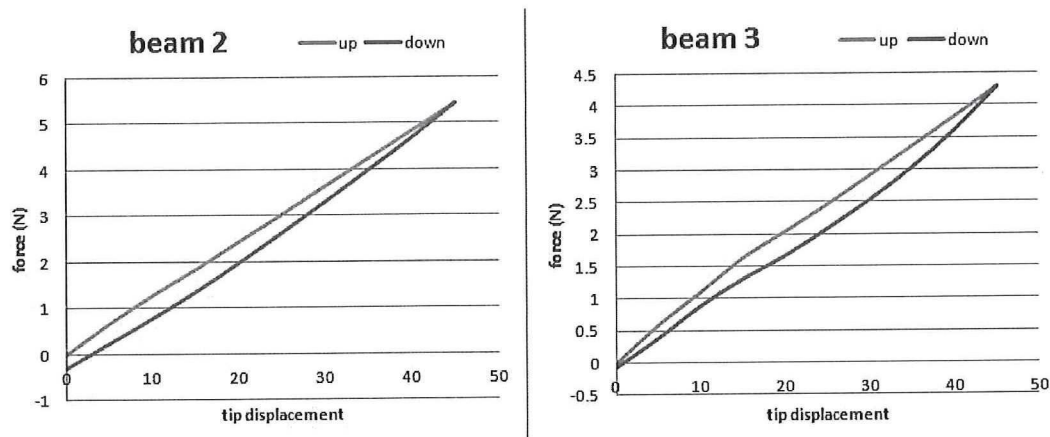


Figure 5. 19 Load history for beam 2 and beam 3 in static test

Compared with the load history path of beam 2, the plot of beam 3 clearly shows a change in gradient near the height of 15 mm. Such a difference was confirmed by the second set of data and can be ascribed to structural changes during loading. When the tip of beam 3 was elevated near 15 mm height, a structural change occurred in debonding area, bringing a sudden loss of stiffness. When a higher displacement was reached, the slope decreased. With a worse linearity, it can be considered that plastic deformation took place in some part of beam 3. In addition, the peak force in the case of beam 3 is approximately 1 N smaller than the peak value on beam 2, which directly reflects the stiffness loss. But as shown in the figure, this slope change is not so clear and is hard to quantify for further analysis.

5.4.1.3 Analysis

5.4.1.3.1 Bending strain

The bending stiffness of beam 1 and the product of flexural modulus and moment of inertia, flexural rigidity EI , were obtained from the stiffness test. The latter ($EI = 103.36(Pa \cdot m^4)$) is valuable when calculating a theoretical value of supporting force in the static tests. In a case of cantilever beam loaded at free end, the relation between the force and end deflection is given by (1):

$$F = \frac{3EI}{L^3} \Delta \quad (5.1)$$

where F , L , and Δ denote force, length, and displacement respectively. Therefore, it can be predicted that the supporting force is 8 N when the beam tip reaches 45 mm in height. However, the actual force measured by a load cell was about 5 N. The difference compared with the theoretical value can be possibly attributed to the fact that a perfect clamping is not allowed as the integrity of the composite beam needs to be ensured.

In further calculations, the flexural modulus of the carbon fiber skin can be estimated by assuming all bending stress was carried by CFRP skins: $E_f = 101.53 GPa$. Based on the knowledge of flexural modulus and force, local bending strains on skin surface are able to be calculated in two methods.

First, general formulas involving section modulus for a cantilever beam which is loaded at the free end are used.

$$I = \frac{bh^3 - (b-2t)(h-2t)^3}{12} = \frac{0.05 \times 0.01^3 - 0.04916 \times 0.00916^3}{12} = 1.02 \times 10^{-9} m^4 \quad (5.2)$$

$$Z = \frac{2I}{h} \quad (5.3)$$

$$\varepsilon = \frac{Fl}{E_f Z} = \frac{Flh}{2E_f I} \quad (5.4)$$

In formulas above, dimensional symbols b , h , and t refers to the width, the height, and the CFRP skin thickness of the beam. In addition, Z and l denote section modulus and the distance to the tip respectively. The proportional relation between bending strain and the distance from the tip is clearly shown in the last formula. The next step is to substitute F and l by the actual force value measured at 45 mm height and the location distance from the tip respectively. Then, the bending strain at the location 1 m from the tip can be estimated:

$$\varepsilon = \frac{5 \times 1 \times 0.01}{2 \times 101.53 \times 10^9 \times 1.02 \times 10^{-9}} = 241.4 \mu strain \quad (5.5)$$

The second method is based on a free body diagram for bending moment, which is shown in figure 5.20. In the case depicted in figure 5.20, the stress in a cross section located 1 m from the tip is investigated. Since the overall moment is supposed to equal to zero in a balanced condition:

$$Fl = \sigma A_s h \quad (5.6)$$

In this equation, σ refers to the local stress in the carbon fiber skin and A_s refers to the cross-sectional area of the upper skin or the bottom skin.

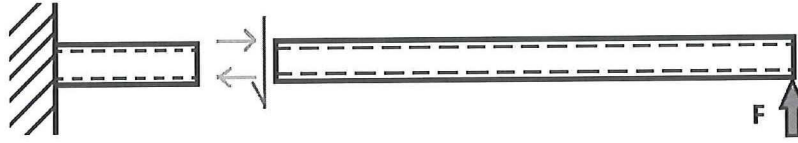


Figure 5.20 Free body diagram analysis of bending strain

By substituting the values into the equation, theoretical values of local stress and strain at 1 m location are obtained:

$$\sigma = \frac{Fl}{A_s h} = \frac{5 \times 1}{0.05 \times 0.00042 \times 0.01} = 238.1 \times 10^5 \text{ Pa} \quad (5.7)$$

$$\varepsilon = \frac{\sigma}{E_f} = \frac{238.1 \times 10^5}{101.53 \times 10^9} = 234.5 \mu\text{strain} \quad (5.8)$$

These two methods share the same assumption that all bending stress is carried by the CFRP skins and walls which enclose the honeycomb core structure. This assumption was made in the design concept of the specimen, the honeycomb core mainly bears shear stress due to its special anisotropic strength properties. In addition, the calculation results from these two methods are similar: 241.4 μstrain and 234.5 μstrain . In most of static tests performed on beam 1, when a 45 mm deflection was made, the local strains measured by strain gauges 1 m from the tip fall between 250 μstrain and 260 μstrain . So the relative difference between theoretical and experimental values of strain is limited to within 6%, which is acceptable for ensuring the applicability of the wireless sensor network. In real situation, there is a variation of bending stress through the skin thickness direction, which means the outer surface has a higher stress value than the average. This may explain the slightly lower theoretical strain obtained as an average value in the calculation.

Similarly, the theoretical values of forces and local strain in static condition are calculated for the cases of beams 2 and 3. Beam 2 has a flawless structure, but its structural properties are not exactly same as those of beam 1 because of different manufacturing batches. Beam 3 was manufactured with an artificial defect, a debonding area between the core and the bottom skin. Experimental and calculated strain values at the location 1 m from the tip for the three specimens are summarized in table 5.1.

Bending strain (μstrain)	Beam 1	Beam 2	Beam 3
Measurement	255.0	303.8	240.6
Calculation method 1	241.4	278.0	228.7
Calculation method 2	234.5	270.0	222.1

Table 5.2 Comparison of bending strain between theoretical values and measurements

Bending strain calculated with first method has larger value then that obtained in second method and is closer to the actual bending strain measured by strain gauges. This is mainly because the variation of bending strain through the thickness is ignored in second method, which results in a lower value. So in table 5.1, which concludes the bending strain comparison, the calculation results from first method are used as theoretical values.

It can be seen that for all three specimens, local strains measured by strain gauges show slightly larger values in the comparison with theoretical strains. For beam 2, the strain at this location was measured as 303.8 μstrain, which is 9% greater than the theoretical value. Similarly, the experimental strain for beam 3 is 5% larger than the theoretical value. These slight differences are expected because strains were measured at middle of top skin surface, which has better flatness than the place near edges. However, the differences between the theoretical values of bending strain and measured data are less than 10%, which demonstrates the reliability of the WSN.

5.4.1.3.2 Shear strain

There are three structural members (the core and two CFRP side walls) carrying shear stress, which is induced by the vertical load. Since the thickness of side walls is very small, it is assumed that all shear stress is taken by the honeycomb core. Due to the accessibility issue, the shear strain on the skin instead of on the surface of the core was measured. As shown in section 5.4.1.1, for beam 1, the strain measured at a 45 ° angle just reaches 30 μstrain. So the actual shear strain can be determined as 60 μstrain. According to an online general database, the in-plane shear modulus of standard UD carbon fiber composites is about 70 Mpa, which is also confirmed by the source providing standard data of flexural modulus (2). Therefore, the shear stress and the force carried by the side walls can be roughly estimated:

$$\tau_f = G\gamma_f = 70 \times 10^6 \times 60 \times 10^{-6} = 4200 Pa \quad (5.9)$$

$$F_f = 2A_w\tau_f = 2 \times (0.01 \times 0.00042) \times 4200 = 0.04 N \quad (5.10)$$

where G , γ_f , and A_w denote in-plane shear modulus, shear strain, and cross-sectional area of CFRP side wall respectively. It is known from this calculation that the force carried by two side skins only takes a small portion of the overall vertical load (5 N) due to their small thickness. So the assumption that honeycomb core bears almost the whole vertical load can be demonstrated and this fact is used in further calculations. The honeycomb core used in the specimen has a 3.2

mm cell size and a 0.05 mm cell wall thickness. Because of its regular hexagonal cell shape, the side length of the cell is 1.85 mm. These parameters are critical to determine the out-of-plane shear modulus of the honeycomb core, which is not included in the datasheet provided by the manufacturer. In general, the out-of-plane shear modulus of a honeycomb structure is greater than that in plane by a factor of $(s/t_c)^2$, where t_c and s denote cell wall thickness and side length of one cell (3). The in-plane shear modulus itself also varies in different directions in the plane with a maximum value in the ribbon direction and a minimum value in the transverse direction. In order to make a conservative estimate, the minimum in-plane shear modulus of 24 MPa is substituted in following calculation of out-of-plane shear modulus.

$$G_o = G_I \left(\frac{s}{t_c} \right)^2 = 24 \times 10^6 \times 37^2 = 32.86 \text{ GPa} \quad (5.11)$$

$$\gamma_c = \frac{F}{A_c G_o} = \frac{5}{0.05 \times 0.01 \times 32.86 \times 10^9} = 0.3 \mu\text{strain} \quad (5.12)$$

G_o , G_I , γ_c and A_c refer to the out-of-plane and the in-plane shear modulus of the honeycomb structure, shear strain, and cross-sectional area of the honeycomb core. The shear strain of a honeycomb core calculated from the formula shows a rather small value, especially knowing the skin shear strain reaching 60 μstrain . This is in conflict with the assumption that carbon fiber skins and honeycomb core are bonded together and are supposed to share similar strains. The problem may lie in the determination of the out-of-plane modulus, whose exact value needs to be obtained from experiment. So a better approach is to perform the calculation in reverse.

$$\tau_c = \frac{F}{A_c} = \frac{5}{0.05 \times 0.01} = 10^4 \text{ Pa} \quad (5.13)$$

$$G_o = \frac{\tau_c}{\gamma_f} = \frac{10^4}{60 \times 10^{-6}} = 166.7 \text{ MPa} \quad (5.14)$$

As mentioned, this calculation result needs further confirmation. But the measurement results of shear strain fully confirm the assumption that the honeycomb core carried almost all the vertical load although its local shear stress is smaller than that of CFRP walls.

5.4.2 Slow dynamic test

Slow dynamic tests on beam 1 at frequencies lower than 1 Hz were performed by programming the displacement and speed of the linear actuator. As mentioned in section 5.3.2, after a series of tests with standard mounting of the specimen, tests were repeated with another mounting type. As an result, bending strains at four locations (1 m, 0.9 m, 0.3 m, 0.2 m) and shear strains at two locations (0.98 m, 0.22 m) were measured during tip slow motions at five frequencies. Because the bending strain at 1 m has the largest absolute value, it was least influenced by random factors and the measurement result at 1 m is considered a good candidate for analysis. In addition, shear strain at 0.22 m is also included in the comparison between the chosen frequencies.

Due to restrictions in maximum acceleration and the speed of actuator, the largest frequency of tip movement traveling between 0 mm and 45 mm was 0.5 Hz. For the cyclic movement from 0 to 20 mm, a maximum frequency of 1 Hz was reached. Therefore, bending strains measured when the specimen tip reaches 45 mm and 20 mm were recorded and compared for several frequencies. As shown in figure 5.21, the peak values of bending strain in the slow dynamic tests are all larger than the reference value obtained in static condition. For the group of 45 mm, the largest increment is 24 μ strain, 10.5% of the static value. The bending strain in the 20 mm group is increased by at most 15.5%.

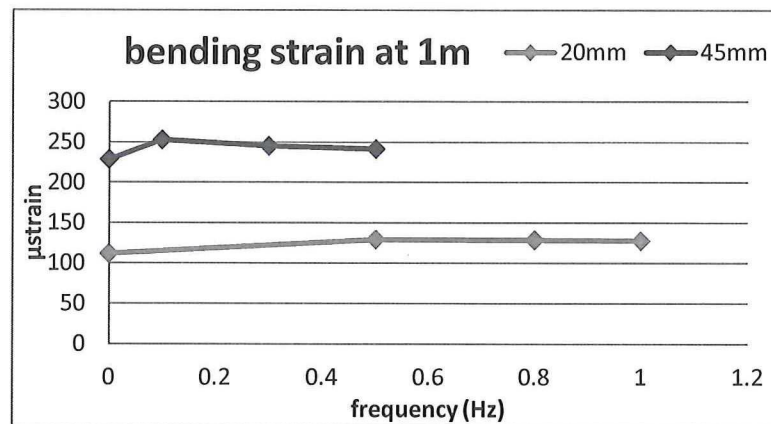


Figure 5. 21 Recordings of bending strain at different frequencies

Probably due to the relatively small absolute values, greater increments of shear strain were recorded: 20.1% and 46.1% for 45 mm and 20 mm displacement respectively. It is shown clearly in figure 5.21 and figure 5.22 that strain values in slow movement were higher for all frequencies than those measured in static tests. For instance, at 45 mm height, bending strain rose by 7.8% on average while the corresponding rise at 20 mm height was 14.8%. Shear strains increased by an average of 19.5% at 45 mm and 44% at 20 mm.

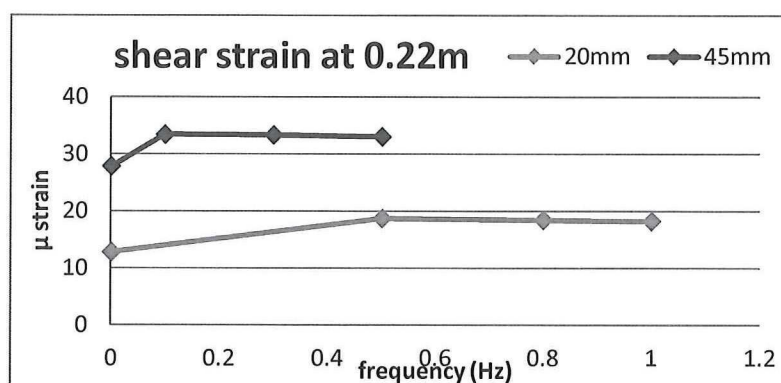


Figure 5. 22 Recordings of shear strain at different frequencies

This increment was believed caused by dynamic effects, which implies that the known strain level at static condition should not directly be taken as reference for a dynamic test at high frequency. It is probably because the stable value measured in static tests at each step indicates that the strain after stress is fully distributed over the whole structure and even partially to the clamp. However, the measurements in the slow dynamic tests acquire instantaneous strain values during

motion and, consequently, higher local strains were obtained.

In addition to the overall rise, it needs to be mentioned that the maximum strain value was recorded for motion at the lowest frequency in all groups. Even though it is difficult to identify the reason for this tendency, the difference of strain level between motions at different frequencies is negligibly small, which allows an assumption that the change in strain along with increasing frequency is limited. When considering the maximum frequency involved in the slow dynamic test was only 1 Hz, structural behavior may differ at higher frequency. In addition, the factors relating to the measurement system should be considered as well, especially in an extremely fast dynamic test. Specifically, accurately recording the instantaneous strain value is highly related with the interaction between the WSN and the specimen in motion. Therefore, the question about the relationship between strain level and frequency in the field of relatively high frequency is reserved with the next section.

5.5 Summary

Static tests and slow dynamic tests shared the same test setup, so they are presented in this chapter together. The setup consisted of a linear actuator, a controller, a PC, a mounting structure, a load cell, and an amplifier. During tests, the root part of the specimen was fixed on the mounting structure by a clamp and its tip was driven by the actuator to desired heights. Measurements of strains, force, acceleration, and temperature were realized by applying a measurement system based on WSN and the load cell.

During trial static tests on beam 1, the reliability of the WSN was proved by comparing with a wired measurement system. It was also known from the trial tests that the influence of accelerometer attachment on the specimen tip can be ignored and that measured strain values slightly decreased when the specimen tip was hold at a certain height for a longer time. In addition, the effects of multiple cycles of the tip motion was found role limited although hysteresis phenomenon existed. In accordance with theory, measured bending strain was found to be proportional to the distance to the specimen tip and the shear strain had an identical value along the specimen. When the static tests were performed on beams 2 and 3, measured data were analyzed in aspects of noise, strain values, and force. During these measurements, electrical noise was introduced by bridge circuits incorporating strain gauges and resistors. With regard to strains, the influence of debonding on beam 3 was mainly reflected by shear strains, which showed a worse proportional relationship to tip displacement and had a large difference in value between two measured locations. According to the load history, a sudden stiffness loss was caused by the existence of the debonding area.

For all three specimens, peak bending strains obtained at maximum height were compared with theoretical values. As a result, their differences are less than 10%, which demonstrates the applicability of the measurement system based on a WSN and the quality of specimen fabrication. And in further calculation in respect with shear strains, it is confirmed that almost all shear stresses were distributed in the honeycomb core. Also importantly, strains and forces acquired in the static tests can be used as references in the latter dynamic tests.

In the slow dynamic tests, the specimen tip was moved continuously and measurements were

performed at the same time. With five frequencies of no more than 1 Hz involved, the slow dynamic tests provided strain data for a comparison among different frequencies. It was found that strain values jump to higher level when the measurement was taken for a slow moving beam instead of a static condition. This was more obvious in the comparison of the shear strains. However, in frequencies under 1 Hz, strains did not rise with an increasing frequency of the tip motion but kept at a stable level. In conclusion, the dynamic condition indeed has an influence on the strain measurement while a frequency change within 1 Hz makes no difference. Since the flapping frequency of a rotor blade is about 8 Hz, which cannot be reached by the actuator, further dynamic tests with higher frequencies are required to implement a simulation and measurement. These are described in the next chapter.

5.6 References

1. Chen W F. Handbook of structural engineering. Crc Press, 1997.
2. Performance composites. Mechanical properties of carbon fiber composite material [cited 2015 January 26th]. Available from:
http://www.performance-composites.com/carbonfibre/mechanicalproperties_2.asp
3. Ali I, Jun Y J. Mathematical Models for in-Plane Moduli of Honeycomb Structures-A Review. 2014.

Chapter 6

Dynamic Test

6.1 Introduction

In order to establish an SHM system based on WSNs for a helicopter rotor blade, a simulation of rotor blade movement is required to investigate the structural response and to conduct the analysis. Flapping is one of main rotor blade movements and it is relatively severe in operation. In addition, its repetitive movements strongly contribute to defect growth. Therefore, simulating the rotor blade flapping movement was set as a major target in the experiments and a series of dynamic tests were made with a test setup that realized such a simulation. Repetitive movement of the specimen tip at frequencies similar to that of an actual rotor blade flapping was driven by a fatigue machine. A WSN measurement system recorded real-time data of the specimen at the same time. Dynamic effects, especially those relating to high frequency motion, were analyzed by comparing this data with those collected in the static tests. More importantly, influences brought by the debonding area on the structural response of the specimen were investigated in this highly dynamic condition.

6.2 Test setup

Since the ZABER actuator used in Chapter 5 is not capable of supporting the required motion of the specimen tip with the needed relatively high frequencies and large displacement range, a hydraulic fatigue machine was employed in the dynamic tests. It is a MTS testing machine which is able to provide a load of up to 10 kN, a motion speed up to 1200 mm/s, a frequency of up to 500 Hz and a displacement of up to 50 mm. The motion of the fatigue machine can be programmed, started, and terminated by using software on a control PC. A metal frame used to mount the root of specimen was fixed to the cylindrical pillars of the fatigue machine in order to form a rigid test frame. Figure 6.1 shows a picture of the fatigue machine and a schematic diagram of the frame. Four horizontal arms were connected with four red plates, as shown in the figure. By adjusting the height of each plate, the beam used for holding the specimen was

adjusted to have a perfectly horizontal top surface. Then the fixation of the specimen root was completed by tightening bolts.

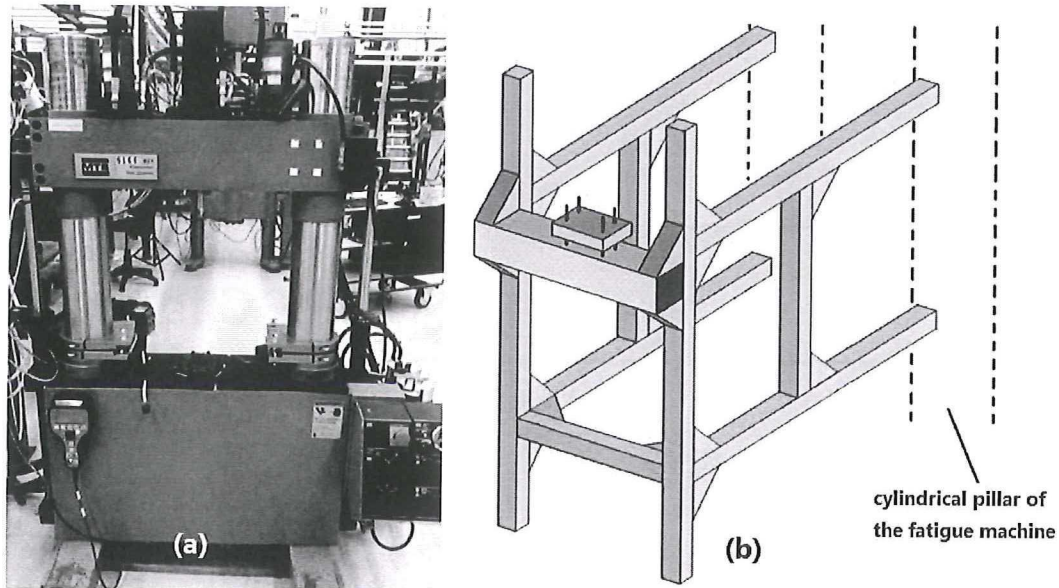


Figure 6.1 Fatigue machine (a) and metal frame fixed to the fatigue machine (b)

Special connecting parts were produced in a workshop and attached to the tip of specimens with epoxy adhesive. Thus a tight connection between the specimen and the moving part of the machine can be obtained by using a combination of screw, bolt and the attached connecting parts. As shown in figure 6.2, the bolt was put through a ball in the connector of fatigue machine to allow limited amount of rotation and tightened to the connecting part attached on the specimen. Such a precise connection allowed an accurate transfer of forces, displacements and speeds, which was strictly required in the experiments. As used in the setup for static tests, a load cell calibrated for both tensile and compressive loading condition in advance was mounted between the machine and the specimen. Technicians in the Structures and Materials Laboratory, TU Delft supported the design and construction of the test setup.

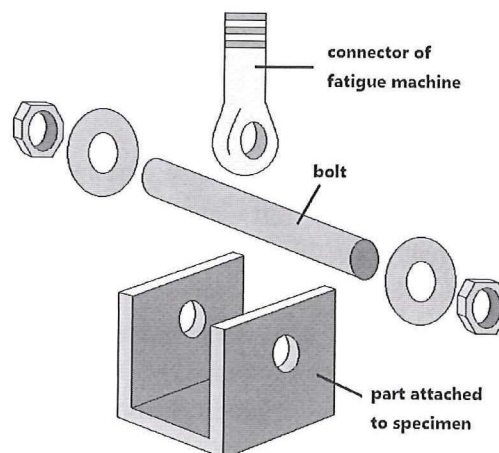


Figure 6.2 Connection between the fatigue machine and the specimen

Extra care was taken to calibrate the initial position of specimen tip, so that no force was imposed

between the machine and the specimen. The specific steps to determine such a position are: adjusting the height of the clamping part of rigid frame to achieve the appropriate position; making minor adjustments to the bolted connection without lifting or pressing down the specimen tip; screwing the bolt tightly to fasten the joint securely.

A WSN and a wired measurement system were applied in the dynamic tests with various electronic components involved as described in Chapter 5. Combined with the mechanical hardware introduced above, they were configured to a relatively complex experimental setup, which is shown in figure 6.3. With regard to the measurement systems used, more information is proved in the next section because there were changes for different test runs.

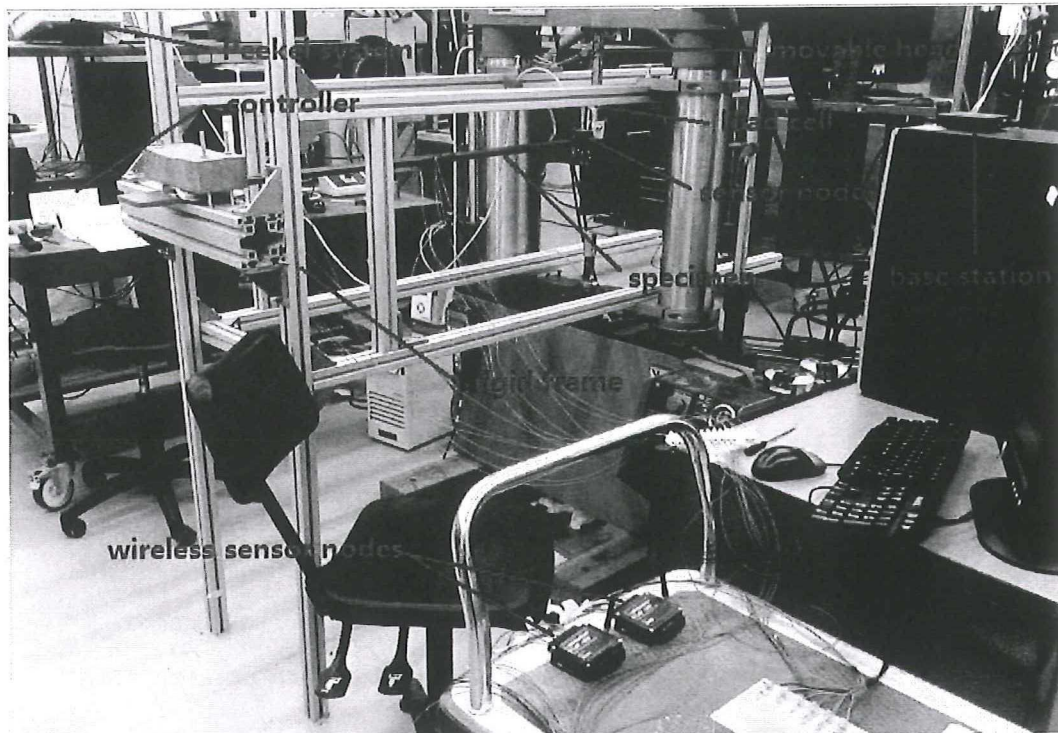


Figure 6.3 Physical layout of the experimental apparatus during a dynamic test

6.3 Experiment

Since the dynamic test is the main part of experiment presented in this thesis, its experimental procedure was relatively complex. The dynamic test for beams 2 and 3 consisted of three sections. These three sections followed the same motion schedule but differed in specimens and measuring methods. Firstly, the WSN played the role of measuring the structural response of beam 2 which had its tip in a dynamic motion. As described in section 3.2.2.1, beam 2 has six strain gauges attached on different locations. They were connected to two V-Link-LXRS sensor nodes to access the WSN. At same time, a G-Link-LXRS sensor node functioning as an accelerometer also provided real-time data. Therefore, a wireless base station received data from these two sensor nodes, collecting real-time information through ten channels: six for strains, three for acceleration (three directions), and one for temperature. After changing the specimen, the same test was performed on beam 3 with an identical setup. By comparing the measured

parameters from the first two sections, of beam 2 and beam 3 respectively, debonding influences on the structural response of a motion simulating flapping can be analyzed.

In general, the measurement results were obtained from the following sources: a load cell positioned between the specimen tip and the fatigue machine; a position sensor integrated in the moving head of the fatigue machine; strain gauges placed on the specimen; a wireless accelerometer mounted near the beam tip; and a temperature sensor integrated in the accelerometer sensor nodes. Among them, the load cell needed extra calibration work in tensile loading since the conversion factor between force and output voltage was determined in a compression test. Then the factor provided by the new calibration was used to further process the data from the load cell. The real-time data from all these sensors were finally collected from two monitoring PCs and analyzed together. The whole testing system for dynamic tests with a WSN measurement system involved is presented in a schematic plot in figure 6.4.

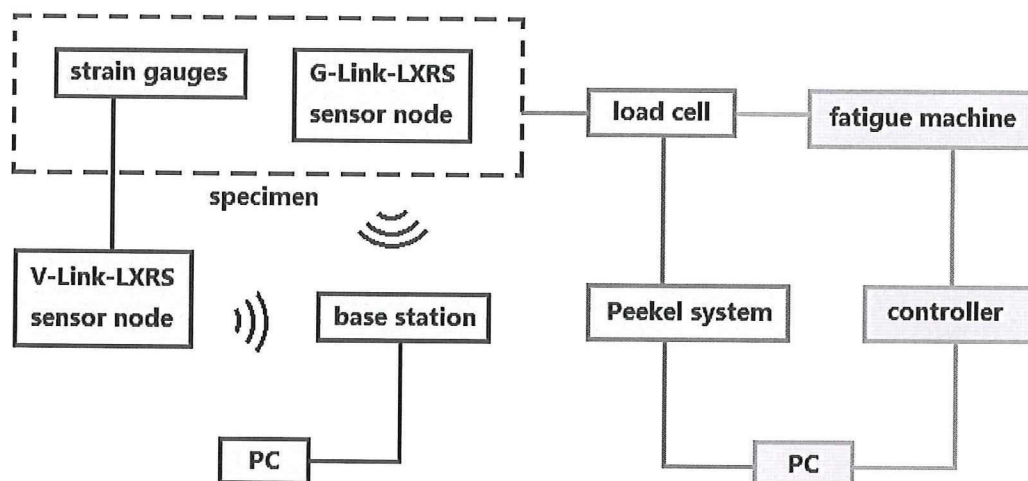


Figure 6. 4 Schematic plot of dynamic testing system incorporating a WSN

In the last section, a wired measurement system supported by a PEEKEL PICAS amplifier was used to provide the reference data of beam 3. This wired system is capable of processing data at a high sampling rate of 1024 Hz and is competent in collecting data from a dynamic environment. To test the performance of the WSN under dynamic conditions, the strain gauges were disconnected from the wireless sensor nodes and wired to the PEEKEL amplifier, which only processed the signal from the load cell in the first two sections. So real-time strain data from beam 3 were sent to PC through six channels and recorded in an output file. In addition, it is possible to confirm potential conclusion from the comparison between beam 2 and beam 3.

Combinations of different frequencies and various travel ranges of tip movement were realized by programming the fatigue machine controller. In each section, motion of specimen tip at three frequencies (8 Hz, 12 Hz, and 16 Hz) was made. Because 8 Hz is the typical frequency of an R22 rotor blade flapping during normal operation, it was set as a critical value in these dynamic tests. The reason to apply other two frequencies higher than 8 Hz is to evaluate the performance of specimen structure and the WSN in more severe dynamic conditions. At each frequency, the specimen tip is displaced by the movable head of fatigue machine traveled in six different ranges. The motion ranges are numbered in the order of testing and shown in table 6.1.

Motion range	1	2	3	4	5	6
lowest (mm)	-5	0	-10	0	-15	-20
highest (mm)	5	10	10	20	15	20

Table 6.1 Conclusion of six movement ranges in dynamic tests

Due to the large sampling rate (256 Hz) employed and restrictions of receiving bandwidth in a base station, all data from the ten channels was gathered by operating the 500-cycle test three times. In each test, the tip started the movement from an initial position and stopped at the same position at the end of the test. As mentioned above, six groups of test with different motion range was included at each frequency. However, when it came to 16 Hz, twice of the normal frequency, the last two groups with two largest ranges were not performed because of violent shaking of the connecting part.

6.4 Results and analysis

The results of the dynamic tests on beams 2 and 3 were presented and analyzed in aspects of load, strain, and acceleration. In the strain part, in addition to conclusion about strain values, the noise that occurred in the strain data obtained from the WSN was analyzed and calculations of strain ratio were made to find out the difference in strain distribution between beam 2 and beam 3.

6.4.1 Load

Due to the complexity of specimen mounting and the subtle interactions between rigid frame and the fatigue machine, it was hard to maintain consistent mounting situation after specimen replacement. In the dynamic test, no clear result was obtained from the comparison of forces that were applied on beam 2 and beam 3 to support them to required position. To be specific, the force on beam 2 was smaller than that on beam 3 at 16 Hz, but became the larger one at 8 Hz or 12 Hz. This inconclusive result may be because of the difference in manual clamping and connection. It is also possible that the load cell mounting condition is affected by the highly dynamic movement, which remained as an insoluble problem with limited load cell options available. Therefore, the force data was mainly used for exploring the relation between global structural response and movement parameters such as amplitude and frequency.

The force data on beam 3 was used for the analysis because the measurements from the load cell in the second and third section can offer a mutual corroboration to ensure reliability of analysis results. In one sense, the amplitude, defined as half of the tip displacement range, can characterize the deformation of the specimen. As confirmed in the static test, the relation between force and displacement is expected to be proportional. However, the result from the dynamic test showed a different changing trend of force along with increasing amplitude. Since data with high amplitudes at 12 Hz and 16 Hz were beyond the measuring limit of the PEEKEL amplifier, 40 N, data set at 8 Hz was investigated to analyze this trend. As shown in figure 6.5, an approximate linear increasing trend can be observed in the low amplitude field. But when the amplitude was set above 15 mm amplitude, a much higher force was needed to elevate the tip to

the required position. The potential reasons for such a significant force increment for high amplitude are: acceleration played a bigger role when higher speed was required in these tests; a horizontal force component cannot be ignored once the specimen tip tended to deviate from the movement axis. It is also shown in figure 6.5 that movement at higher frequencies resulted in an overall rise of maximum forces, which is thought to be caused by acceleration.

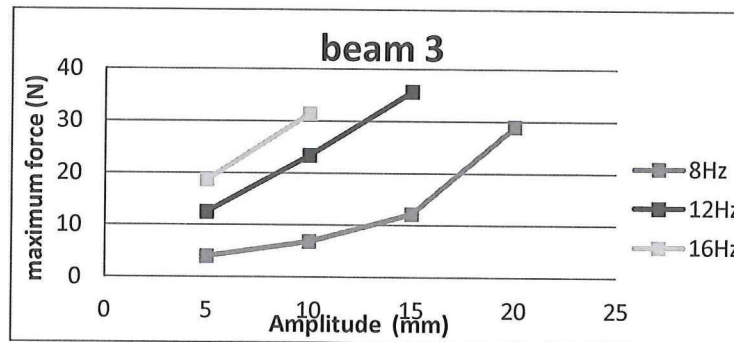


Figure 6.5 Collection of maximum forces with various movement parameters for beam 3

As mentioned, there were two supplemental movement patterns with amplitudes of 5 mm (0 to 10 mm) and 10 mm (0 to 20 mm). Due to the limitation of maximum mechanical stroke, similar supplemental patterns with higher amplitudes were not allowed. The maximum force measured in a supplemental movement pattern on beam 2 was found to be close to the force in the original symmetrical movement pattern in both cases. This was mainly because the bending stiffness in the upward direction and the downward direction are similar, which had already been determined by static tests. For beam 3, which has an upward bending stiffness larger than its downward bending stiffness, maximum forces recorded in asymmetrical movement patterns were higher than those of symmetric patterns. An example is shown in figure 6.6, where the maximum force can be obtained by calculating the difference between the peak value and valley value. In figure 6.6 (a), the maximum force is about 23 N, and for an asymmetrical pattern as shown in figure 6.6 (b), the maximum force is 29 N. The introduction of a larger horizontal force component with the specimen tip driven further from the initial point may be considered as another reason for such a force increment.

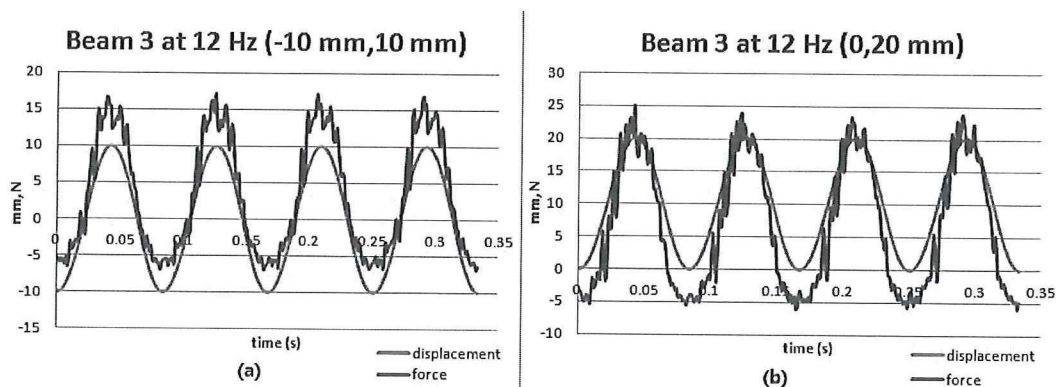


Figure 6.6 Comparison between (a) symmetrical and (b) asymmetrical movement patterns with the same amplitude for beam 3

In each test, the specimen tip was driven in a repetitive movement with a certain amplitude and at certain frequency, which reveals the changing trend of force along with changing tip displacement. For instance, in the test of beam 3 with tip movement between -10 mm and 10 mm at 16 Hz, recordings of force in four cycles and corresponding displacements are plotted together in the time domain in figure 6.7. It can be seen that a sinusoidal waveform represents the change in displacement along with time and a more steep change can be observed in the loading cycles which are plotted with a red line. This large slope is supposed to be attributed to acceleration involvement in the process of rising and falling. Similar to the result from the static test, the peak values of force were recorded near by the maximum displacement positions. However, if a closer look is taken, the peak values do not occur exactly at those positions but somewhere a little earlier. At the moment the specimen tip reached the highest position, it was subjected to a downward acceleration to make it stop and start to fall. Therefore, an obvious sudden drop of force can be seen nearby the maximum displacement position. Then the occurrence of peak force before reaching highest position can be explained as well. In addition, real-time force measured in movements at high frequencies was several times larger than the force measured at the same height in the static test. So it is rational to believe that dynamic factors can bring a significant influence on structural response and such influence possibly results in magnified difference between the different specimens' performance.

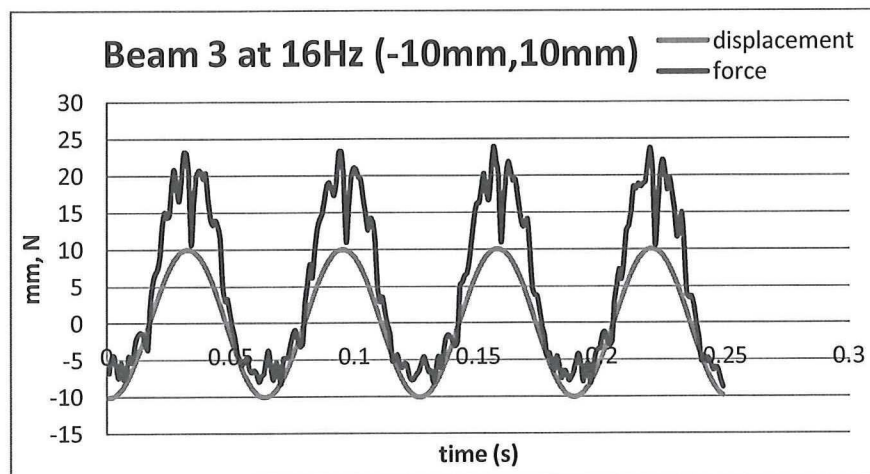


Figure 6. 7 Load history and displacement recording in movement (-10 mm, 10 mm) at 16 Hz for beam 3

Since some fluctuations in addition to the main waveform can be observed in figure 6.7, a noise analysis based on Fast Fourier Transform (FFT) was carried out. Because of the ubiquity of small fluctuations in dynamic tests, the noise analysis was performed on every test, in which a movement was made with certain amplitude at certain frequency. The analysis results were similar for all tests and can be shown in similar diagram in frequency domain. The noise analysis of the test, in which tip of beam 3 moved between -5 mm and 5 mm at 16Hz, is displayed in figure 6.8.

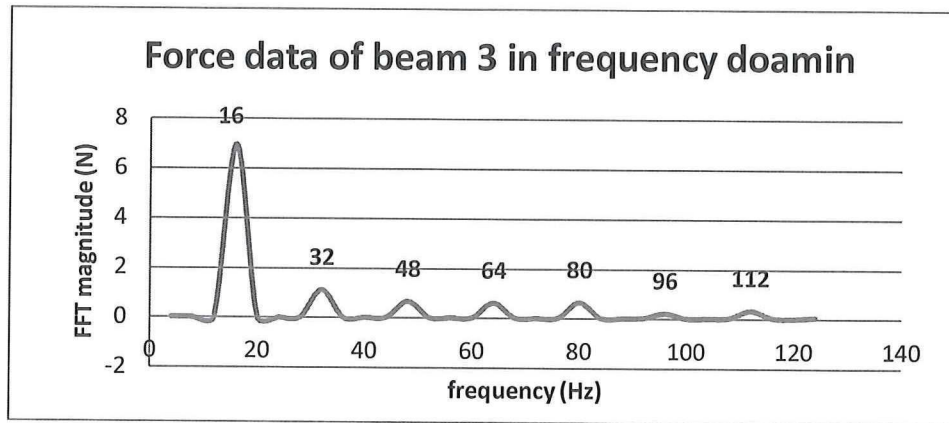


Figure 6.8 Force data in the frequency domain in movement (-5 mm, 5 mm) at 16 Hz for beam 3

As known, the movement frequency was 16Hz, which is also reflected as the most prominent peak in frequency domain. It is worth noting that other peaks with lower intensity all appear at the frequencies multiples of 16Hz and that peaks located closer to 16Hz have larger values. According to the force data in frequency domain, vibration harmonics are confirmed to be the causes of the noises observed. 32 Hz was the frequency of second harmonic and was twice of the fundamental frequency. The intensity of the vibration harmonic at 32 Hz is 14% of the intensity of the fundamental movement. The rest can be explained in the same manner and the low energy of high order harmonics is understandable as well.

6.4.2 Strain

6.4.2.1 Strain measurement

In order to accurately monitor strains and accelerations of the specimen in dynamic movement, the WSN performed with a sampling rate of 256 Hz. This is the maximum rate that can be reached within the bandwidth limits. Considerable amounts of data were measured and recorded for each specimen movement of a 500-cycle repetitive movement. Before investigating the influence on strains brought about by the different amplitude or frequency, the recording of strains at six locations in the measurement between -20 mm and 20 mm at 8 Hz was analyzed to possess a preliminary understanding of specimen performance in the highly dynamic condition. This measurement has been selected due to its movement pattern that matched most close to the static condition in both of amplitude and frequency compared to the rest of the movement patterns in the dynamic test.

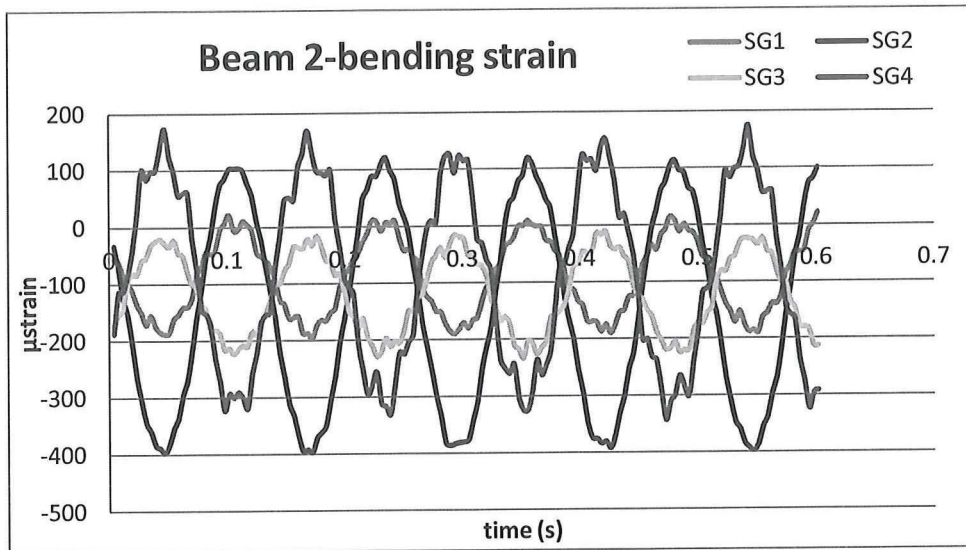


Figure 6.9 Bending strain recording of beam 2 in movement (-20 mm, 20 mm) at 8 Hz

In figure 6.9, data from the four strain gauges are plotted together. Strain gauge 1 (SG1) and strain gauge 2 (SG2) were both mounted on the top skin and the other two were mounted on the bottom surface. That is the reason why the waveforms of the first two strain gauges are exactly opposite in phase to those of the other two. For instance, the top skin sustained a compression and the bottom one underwent a tension when the specimen was bent upwards. With regard to strain level, the relative value of peak strain is included in consideration instead of its absolute value since even a small variation in the mounting conditions may result in an overall shift of strain values. The relative value is defined as the difference between peak strain and valley strain and was calculated in units of microstrain for each strain gauge: 217 μstrain for SG1; 519 μstrain for SG2; 223 μstrain for SG3; and 518 μstrain for SG4. It can be seen that the strain values for SG1 and SG3 were similar and this was also true for SG2 and SG4. Therefore, the structural integrity of beam 2 was verified to be perfectly symmetrical as it was designed.

Compared with the results obtained in static test, the strain level in the fast repetitive movement was found to be much larger. In the example shown in figure 6.9, the maximum relative strain measured by SG1 was at least 25% greater than the strain measured when the specimen tip was held statically at 40 mm height. Additionally, it was already proved in section 6.4.1 that with same amplitude, the specimen was subjected to larger load in an asymmetrical movement pattern than in a symmetrical movement pattern. So it can be concluded that the introduction of fast repetitive movement to specimen tip resulted in an overall strain increase in the specimen. Other valuable information is contained in the ratio between SG2 and SG1, the ratio between SG3 and SG4, or the comparison between these two ratios. The ratios are 2.3 and 2.4 respectively, which means the strain distribution was not strictly proportional to the distance to tip as in the static tests.

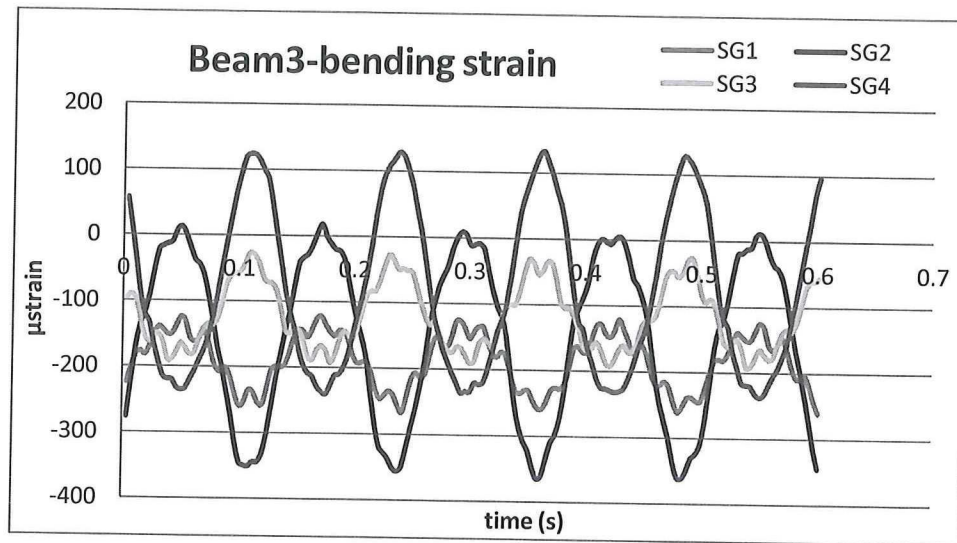


Figure 6. 10 Bending strain recording of beam 3 in movement (-20 mm, 20 mm) at 8 Hz

When same movement pattern (between -20mm and 20mm, 8Hz) was operated on beam 3, a similar trend can be observed in the strain measurement. The relative values corresponding to four strain gauges were 146, 383, 166, and 374 in units of microstrain, which showed a certain difference in strains between two opposite strain gauges. However, such differences were not large enough to be regarded as structural responses to the existence of a debonding area. Strain levels were lower than that of beam 2 in same movement pattern mainly because of different loading conditions, instead of structural defects. The ratios defined above are equal to 2.6 and 2.3 in this case and they will be included in later analysis focusing on strain ratios.

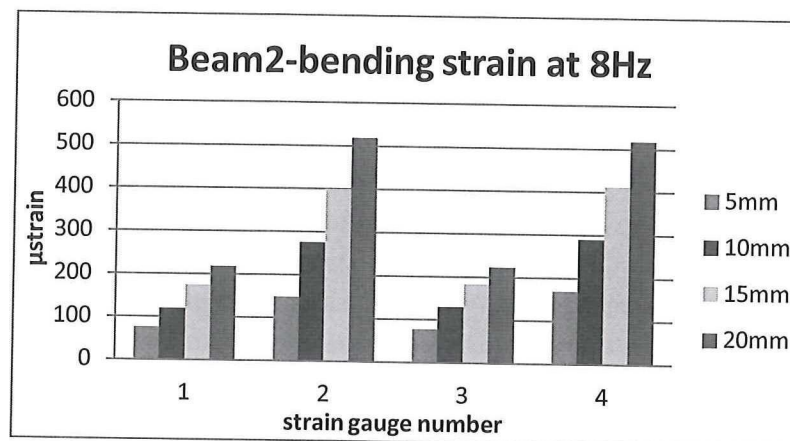


Figure 6. 11 Collection of bending strains measured on beam 2 at 8Hz

Regarding the bending strains measured by the four strain gauges, in total ten symmetrical movement patterns with combinations of amplitude and frequency were included in the analysis process. As shown in figure 6.11, at 8 Hz, bending strains increased with larger amplitude, which conformed well with expectations. This relation between strain value and amplitude was true for all movement patterns at three frequencies, so the ones at 8Hz are taken as examples. More importantly, the variation of trends of bending strains was investigated by comparing the two

specimens to analyze debonding effects, since a comparison of strain level was impeded by poor control of loading.

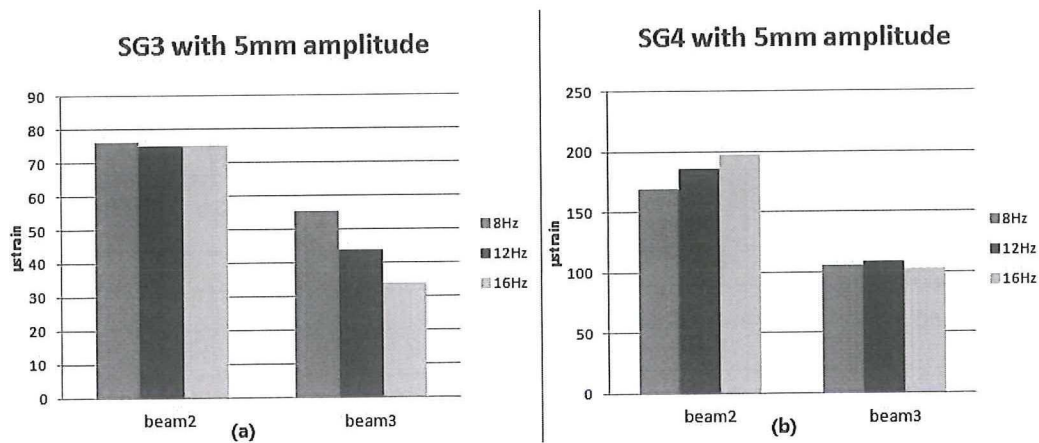


Figure 6.12 Comparison in the variation trend of bending strains from (a) SG3 and (b) SG4 with frequency between beam 2 and beam 3

It is interesting to find out that the variation in trends of bending strain for increasing frequency were completely different on beam 2 and beam 3, which can be proved by measurement results of SG3 and SG4 which are shown in figure 6.12 (a) and (b). SG3 was placed in the middle of the beam with 50 cm distance from the tip and measured a nearly constant strain on beam 2, but a reducing strain value when movements became faster. It can be seen in figure 6.12 (b) that the bending strain of beam 2 measured by SG4 increased with larger frequencies while the strain at same location on beam 3 kept stable. The same observations were also true for movements with 10 mm amplitude. When a larger amplitude was programmed, the frequency of 16Hz was not allowed to reach this displacement for safety reasons. Therefore, there was not enough data to verify this observation for amplitudes larger than 10 mm. The potential reason for this difference in variation trend of bending strain between two specimens may be the interaction between debonding effects in strain distribution and the dynamic factors. It can possibly be explained when further analysis is carried out.

The noise effect was rather severe in all shear strain measurements because of their relatively low strain values. For instance, the shear strain in a movement pattern (between -20mm and 20mm, 8Hz) can only be roughly estimated instead of being accurately calculated as in the static tests. As shown in figure 6.13, the estimated value is about 100 μstrain, which is more than three times the shear strain when the tip was statically held at 45 mm height. However, these measurements can only provide a general range of shear strain but not exact values that are valid for further calculation.

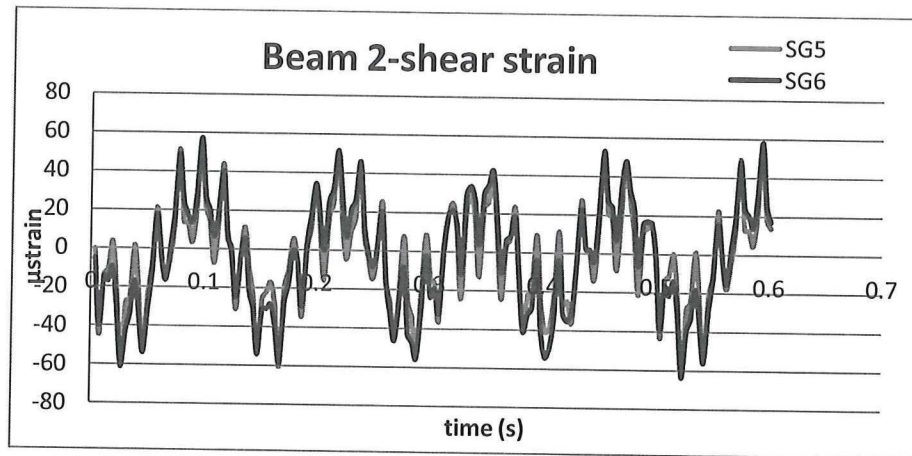


Figure 6.13 Shear strain recording of beam 2 in movement (-20 mm, 20 mm) at 8 Hz

6.4.2.2 Shear strain noise

Due to the fact that noise seriously interfered with the acquirement of shear strain data, a noise analysis based on FFT turned out to be necessary. A movement, in which the specimen tip was driven to repetitively move between -20 mm and 20 mm at 8 Hz, was first targeted in the noise analysis and its result is shown in figure 6.14. Similar results represented in frequency domain were found in all other movement patterns with different amplitudes and frequencies.

In figure 6.14 (a), which displays the data measured on beam 2, there are two obvious frequency peaks: 8 Hz and 50 Hz. The former corresponds to the movement frequency and the latter characterizes the most intense noise component. The noise intensity is estimated to be about 75% of the movement frequency, which resulted in great difficulty in understanding the shear strains measured by SG5 and SG6. In addition to these two main frequencies, some small peaks can be observed as well and they are identified as signals of mechanical harmonics. Different to the plot of beam 2, the plot in figure 6.14 (b) representing measurements of beam 3 shows only one significant peak at 8 Hz. Even though the noise at 50 Hz still exists, its intensity drops down to same level as those of the harmonic signals. As mentioned, all noise analysis process performed on the strain measurements of beam 2 similarly concluded with finding an intense noise at 50 Hz, which did not appear in the tests on beam 3.

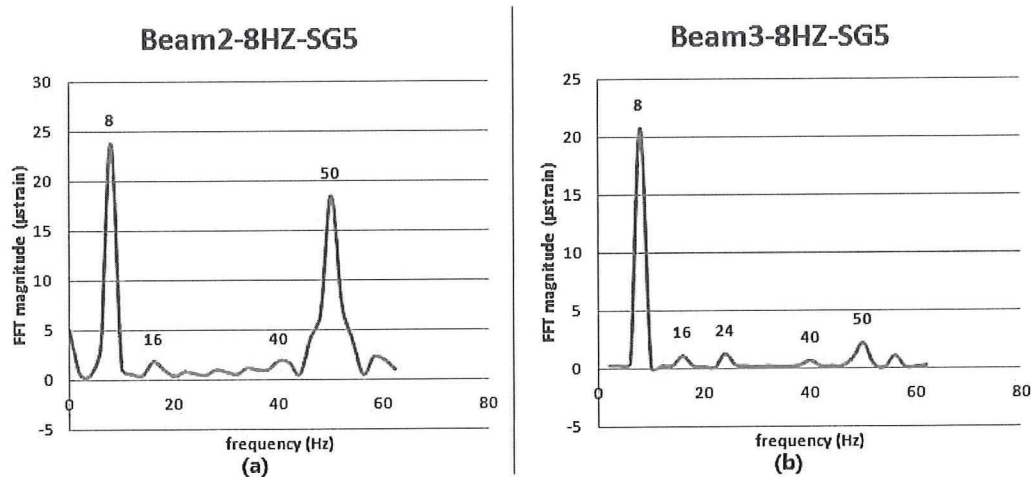


Figure 6. 14 Shear strain measured by SG5 on (a) beam 2 and (b) beam 3 in the frequency domain

According to the experimental schedule, after the tests with all the movement patterns on beam 2 was finished, beam 2 was replaced by beam 3 and mounting, connecting and calibrating were performed to prepare for the tests on beam 3. First, it can be sure that the noise was not induced by the movement of beam structure since it was not influenced by variations of movement parameters. So the potential noise source may be the hydraulic system shared by several fatigue machines or the electrical power working at 50 Hz. Because the fatigue machine employed in the test possesses the smallest loading capability among all the machines connected together by hydraulic pipes, operation of much larger machines possibly influenced the frequency signal. To attribute this noise to the hydraulic system, the operation of the other machines were assumed to be rather different after the specimen was replaced. It is rather difficult to validate this condition due to the involvement of accidental factors, which were brought by various tests operated simultaneously and by complicated test programs. Another possible noise source was the high power electrical supply nearby the test setup, especially the one close to sensor nodes in the measurement system. The noise signal could be transferred and added to the voltage signal generated by strain gauges by induction or other means, and such interaction between the power supply and the measuring system was blocked or changed when beam 3 was mounted and tested. In this way, the noise at 50 Hz became much weaker in the tests on beam 3.

In order to determine the noise source, the same analysis process was used for data from the third test section, in which tests were performed with the same setup on beam 3 but a different measuring system. The result is displayed in figure 6.15, where the peak representing noise at 50 Hz disappears and peaks of mechanical harmonics remain. Taking the related analysis on the three test sections into account, it can be concluded that the noise was introduced by the WSN. Therefore, the workstation power supply turns out to be the most possible candidate responsible for the 50 Hz noise.

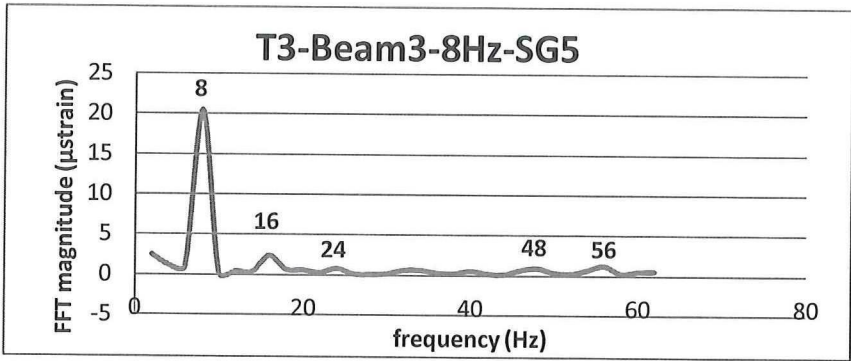


Figure 6.15 Shear strain measured by wired system in the frequency domain

6.4.2.3 Strain ratio

One important part of the data processing is to calculate the ratio between different local bending strains and the relative difference between different local shear strains. As described in section 6.4.1, due to various possible factors such as setup variation and system calibration difference, the absolute loading conditions were found to not be consistent for two specimens in an identical movement pattern. Therefore, the analysis depending on the comparison of absolute strain value may suffer from a low reliability. On the other hand, the investigation of difference in strain distribution allows a discussion about the debonding effects despite the load difference.

For bending strain, its value highly depended on the measured location along the beam. An interaction between dynamic factors and debonding influence may lead to a variation from the theoretical benchmark. Taking these two facts into account, a ratio between the strains of SG2 and SG1 and a ratio between the strains of SG4 and SG3, which reflect the bending strain distribution in both sides to some extent, are introduced in the analysis process. In both cases for beams 2 and 3, the defined ratio has a generally upward trend along with increasing amplitude, which is clearly shown in figure 6.16. In addition, it is known from the relative position of plots on behalf of data at different frequencies, a higher frequency is accompanied by a higher ratio. In summary, the two specimens share similar relations between the bending strain ratio and movement parameters including amplitude and frequency.

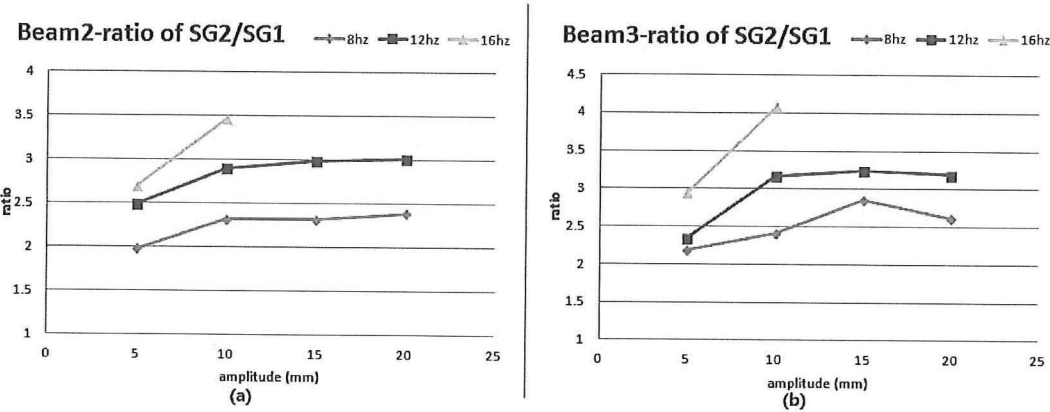


Figure 6.16 Bending strain ratio (SG2/SG1) of (a) beam 2 and (b) beam 3

With constant amplitude, the ratios calculated for the two specimens are compared at three frequencies. The upward trend along with increasing frequency is again clearly revealed in figure 6.17 (a) and (b). No matter with which amplitude, the columns in the group of 16 Hz are the highest while those in group of 8 Hz are lowest. In the comparison between beam 2 and beam 3, the ratio of bending strains measured on beam 3 has higher value in most cases. However, the ratio of beam 2 is slightly higher than the one of beam 3 in the movement pattern with 5 mm amplitude at 12 Hz, showing a result opposite with the rest. Therefore, the effect of debonding area on the ratio between local bending strains measured by SG2 and SG1 is not clear.

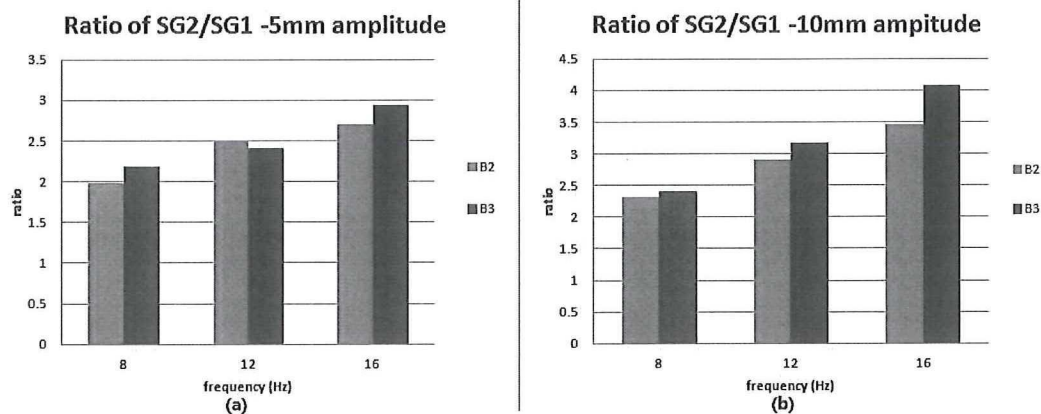


Figure 6. 17 Comparison of bending strain ratio (SG2/SG1) between beam 2 and beam 3

Same data processing is performed on the bending strains measured on the bottom surface of the specimens. The ratio between the strains of SG4 and SG3 is calculated and displayed in figure 6.18. A similar upward trend can be observed, but with an exception in the movement pattern (-20 mm, 20 mm) at 12 Hz. It is possible to attribute this exception to the fact that the strain values used in analysis is highly dependent on sampling when the movement was with large amplitude and at high frequency. In addition, once the frequency went up to 16 Hz, a mechanical resonance noise at 2 Hz was introduced in the measurements and this resulted in a varying peak-to-peak value and a blurry waveform. Therefore, the data measured at 16 Hz needs to be excluded from consideration when a strict analysis is made.

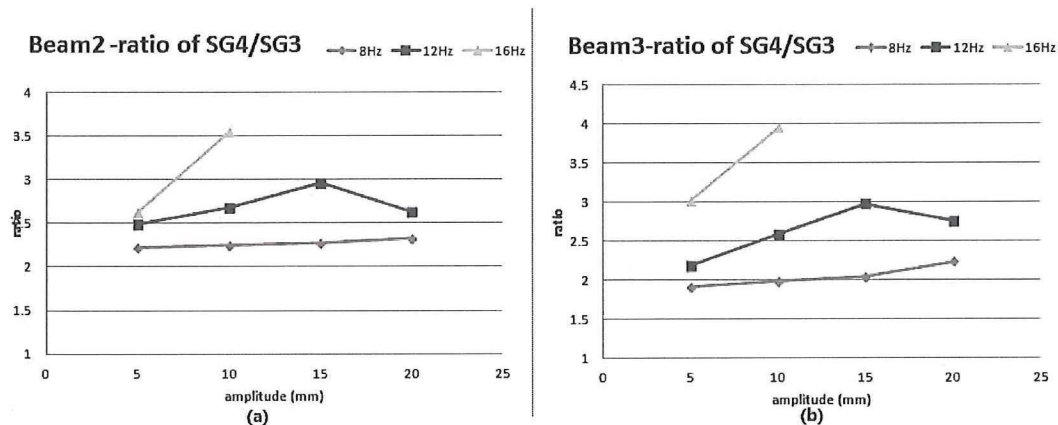


Figure 6. 18 Bending strain ratio (SG4/SG3) of (a) beam 2 and (b) beam 3

Without consideration of the ratio at 16 Hz, the comparison of the ratio between beam 2 and beam 3 shows that the specimen with the debonding area has lower ratio between strains measured by SG4 and SG3. This result can be seen in figure 6.19 and is opposite to the comparison result for the ratio of SG2/SG1, from which can be drawn the conclusion that the existence of defects brought different influences on the strain distribution on the two sides of the specimen. This conclusion is also supported by the relatively consistent ratio values on beam 2, which function as reference. Since the debonding was artificially located between the bottom skin and the core structure, it is reasonable to believe that debonding had much larger effect on bottom surface strain distribution rather than that on the top surface under bending load. In the case of beam 2, where no debonding was involved, the ratio on the bottom surface can be considered the same as the ratio on the top surface. So it is clear that the ratio of SG4/SG3 is reduced because of the debonding area, suggesting an obvious disturbance on strain distribution between debonding area and the clamp.

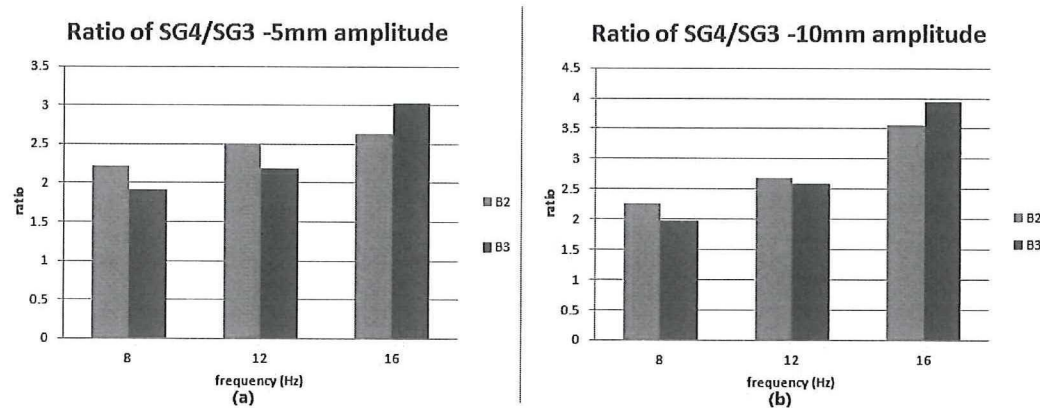


Figure 6. 19 Comparison of bending strain ratio (SG4/SG3) between beam 2 and beam 3

According to theory, the shear strain was supposed to be identical along the specimen. Thus, the relative difference between shear strains measured from two locations can be used as an analytic target. The relative difference is defined as result of $(|SG6-SG5|/SG5)$ and is calculated for each movement pattern.

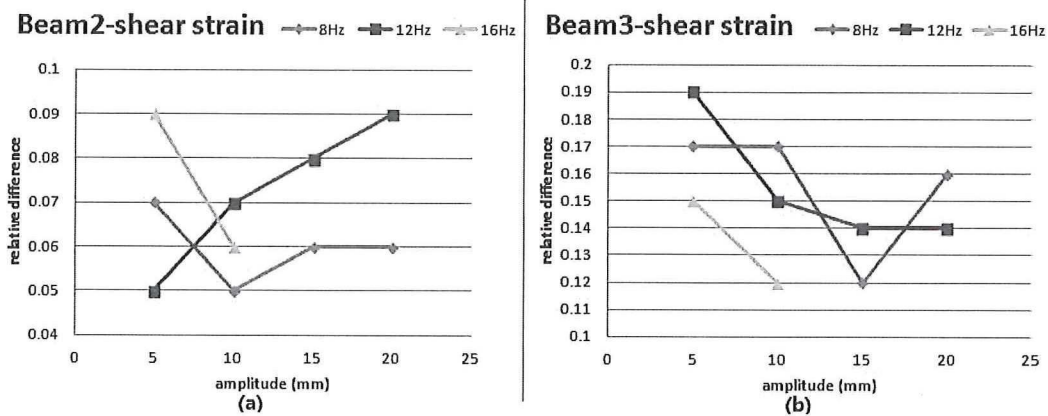


Figure 6. 20 Shear strain relative difference of (a) beam 2 and (b) beam 3

It can be seen in figure 6.20 that there is no explicit relationship between the relative differences and the movement parameters no matter which amplitude or frequency is considered. However, it is worth noting that the relative differences for beams 2 and 3 varies in two different ranges without overlap, which is more explicitly shown in the bar diagram in figure 6.21. This diagram collects the relative differences of shear strain obtained from all movement patterns at 8 Hz and compares them between beam 2 and beam 3. As shown for every group of amplitude, the red bar representing the value of beam 3 is far longer than the blue bar standing for beam 2. Overall, the ratio between relative differences of two specimens is at least 2 and can be up to 3.4, which certainly allows the conclusion that the two local shear strains measured on beam 3 had a much larger gap than their counterparts in the case of beam 2.

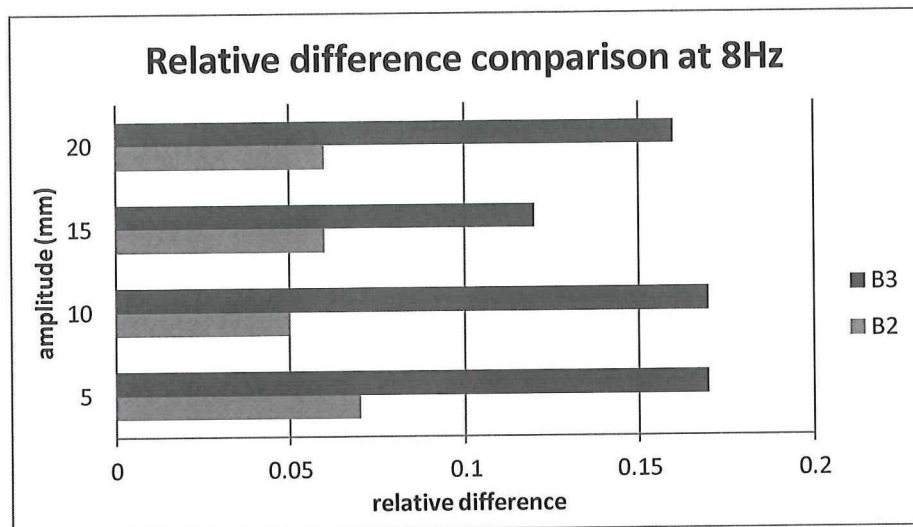


Figure 6.21 Comparison of shear strain relative difference between beam 2 and beam 3

In the case of beam 3, as described in section 3.2.2.1, SG5 and SG6 were mounted on a CFRP side wall and at two sides of the debonding area. In most tests on beam 3, values of SG6 were smaller than those of SG5 by a difference of more than 15%, which means that a significant drop in shear strain on side walls was induced by the debonding area. This difference can be clearly seen in the example shown in figure 6.22, where shear strain recording of defined movement is displayed. This was a result of the fact that the CFRP frame was damaged at the debonding area and some portions of load were transferred to the honeycomb structure to adjust to a new stiffness distribution. So this change was captured by measuring the shear strain at a location close to the debonding area.

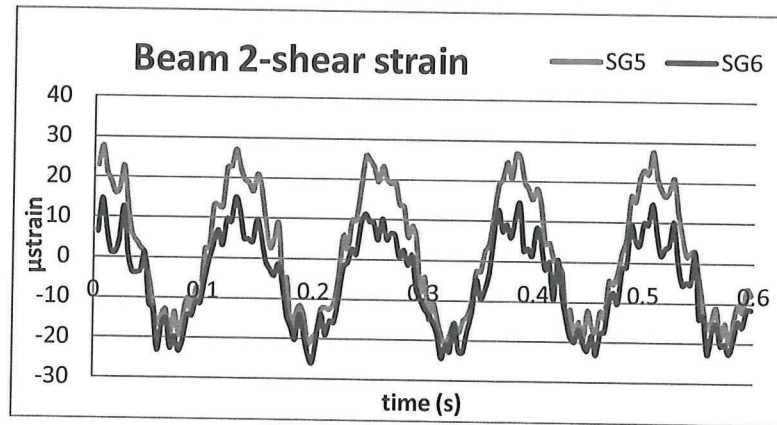


Figure 6.22 Shear strain recording of beam 3 in the movement (20 mm amplitude, 8 Hz)

The relative difference of peak-to-peak value is an alternative indicator for different performance in shear strain. Compared with the method calculating relative difference of all data, a relative difference of peak-to-peak value is susceptible to accidental factors such as measurement errors in determining the peak values. In addition, an overall shift of shear strain level is excluded if only peak-to-peak values are considered. The strain shift may also be a result of debonding effects and its involvement in the calculation can contribute to the identification of the debonding. Therefore, this method is not employed to represent relative difference of shear strain in this thesis. However, it has an advantage in reducing analysis workload as much few data points are processed, which may allow this method to be a good candidate when fast processing is required.

6.4.3 Acceleration

It is reminded that a G-Link-LXRS sensor node was mounted on top surface of beam tip and operated to measure the local accelerations in three directions: span direction, transverse direction, and the direction perpendicular to the surface. According to its working mechanism, there were three independent accelerometers measuring accelerations in these three directions and transmitting the data through three channels to the base station wirelessly. Theoretically, the accelerations in two directions parallel to top surface were supposed to be very small compared with that from the perpendicular direction.

The data from channel 1 and channel 2, which corresponded to span direction and transverse direction respectively, varied by no more than 2.5 g in all movement patterns except the movement with 20 mm amplitude at 12 Hz. As an exception, the acceleration components parallel to the top surface had instantaneous values up to 6 g in this movement. Because these high values of acceleration were measured both on beam 2 and beam 3, they are considered as reliable outputs from the accelerometers. This may be more acceptable by considering that these large accelerations occurred in the movement with most severe combination of amplitude and frequency. In such movement, the components of the force exerted by the fatigue machine in these two directions cannot be ignored when a large amplitude was reached. In addition, acceleration can be used to indicate the vibration intensity to some extent, which matches with

the violent vibration caused by this main repetitive movement and its mechanical harmonics.

In general, beam 2 and beam 3 had similar performance regarding accelerations in the span direction and the transverse direction, so the data of channels 1 and 2 measured from beam 3 are selected to represent the results in figures 6.23 and 6.24.

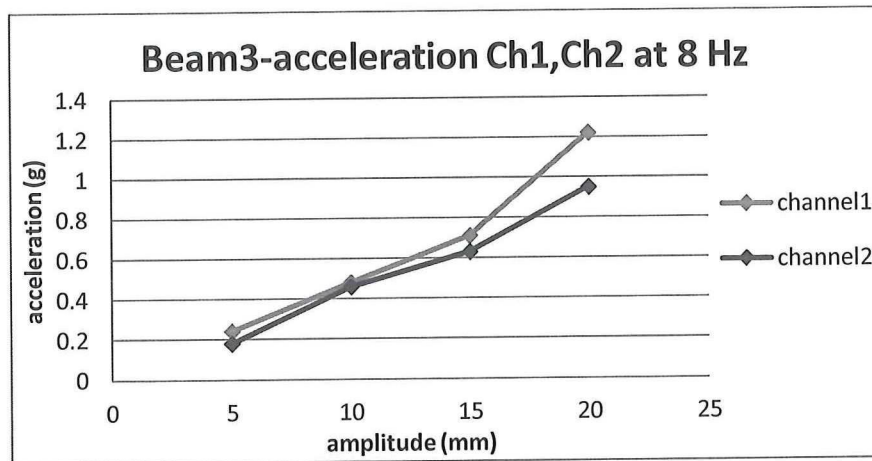


Figure 6.23 Relationship between accelerations (Ch1 and Ch2) and amplitude

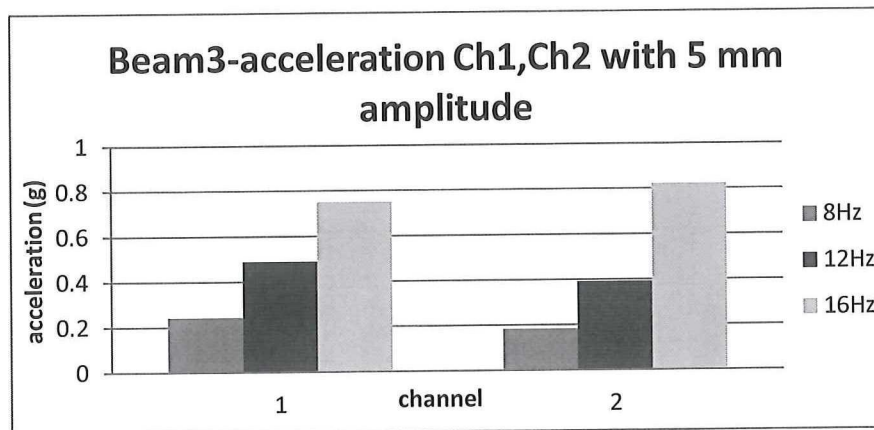


Figure 6.24 Relationship between accelerations (Ch1 and Ch2) and frequency

As shown, either a larger amplitude or a higher frequency in the repetitive movement can lead to an increase in accelerations of channels 1 and 2. This was also true for the acceleration of channel 3, which was in the direction perpendicular to the surface, but with much larger values of acceleration involved. The maximum acceleration reached in the test remains unknown, since its value went beyond the working limit of the accelerometer, 20 g, in the two most severe movements. However, a basic understanding is still allowed by the rest of the measurements, which are all included in figure 6.25. In the plot, the increasing trend along with the larger amplitude and higher frequency is confirmed. And the highest two values of acceleration are specially marked as yellow dots because the exact values are higher but cannot be acquired because of the measurement range limits.

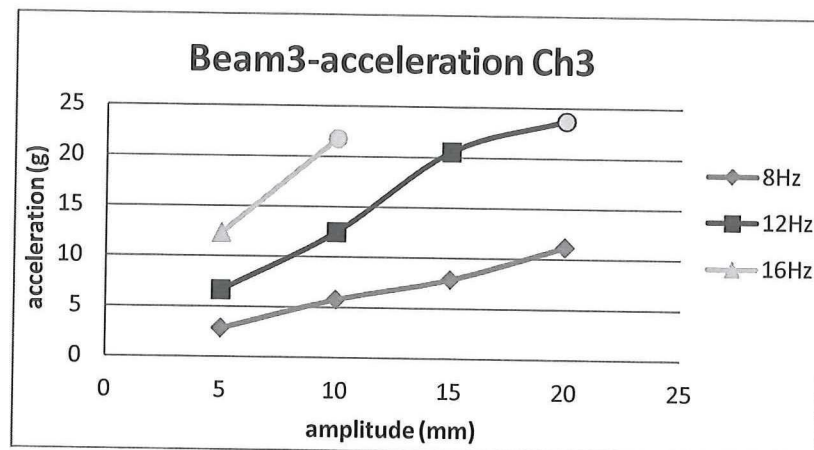


Figure 6.25 Collection of accelerations (Ch3) on beam 3

It is important to note that the accelerations of all three channels shown in plots are peak-to-peak values obtained from the measurement. For instance, in figure 6.26, the recording of acceleration of beam 2 for the movement with 15 mm amplitude at 12 Hz shows a waveform symmetrical about the zero value. Its peak-to-peak value is about 20 g, but the actual maximum acceleration reached with maximum travel distance was half of this and equal to 10 g. This relation can be applied to other movement patterns as well since the non-zero acceleration value at the initial position should be attributed to the calibration of sensors and brought no influence on peak-to-peak values.

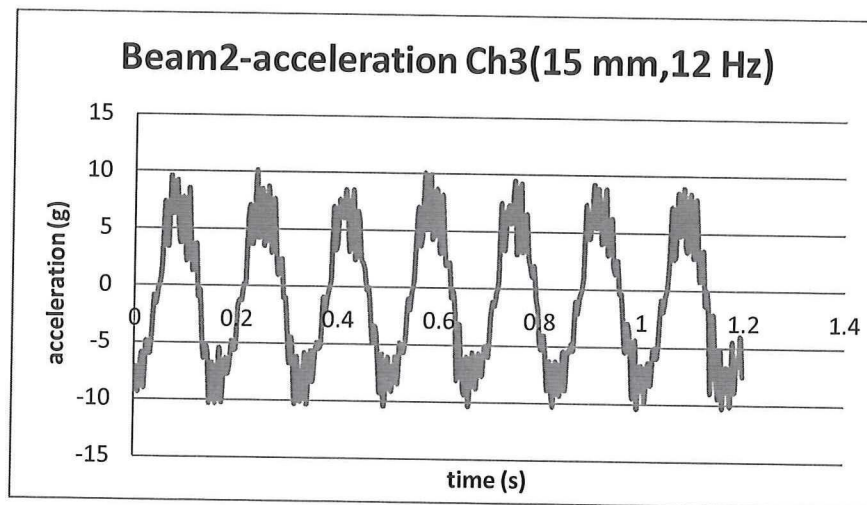


Figure 6.26 Recording of acceleration (Ch3) in a movement (15 mm, 12 Hz) on beam 2

It can be noticed in figure 6.26 that the curve is not smooth, which suggests the involvement of noise at higher frequencies. By following the same noise analysis process applied to the strain data, the acceleration data of channel 3 can be displayed in the frequency domain. For instance, the acceleration of channel 3 measured from beam 2 in the movement at 8 Hz with 15 mm amplitude is shown in figure 6.27. Except the fundamental frequency peak at 8 Hz, two main peaks at 80 Hz and 120 Hz are also shown in the frequency domain, which were probably caused by mechanical harmonics.

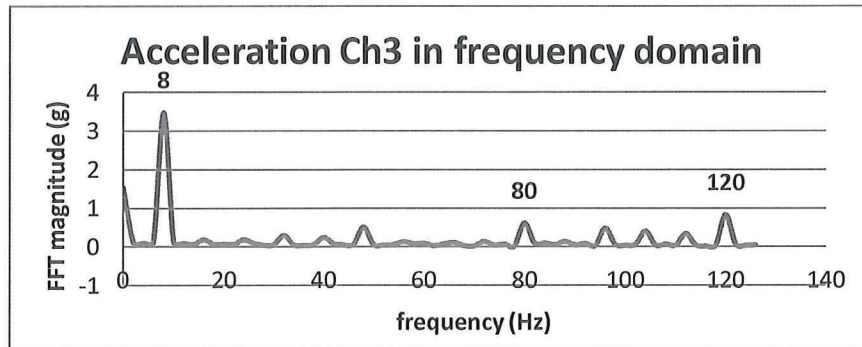


Figure 6.27 Display of acceleration (Ch3) in the frequency domain

In addition, accelerations of channel 1 and channel 2 were found to behave differently in the frequency domain although they both seem to not be regular in the time domain. As shown in figure 6.28 (a), for the data of channel 1 measured in the same movement pattern (15 mm, 12 Hz), a signal at 16 Hz is found to be much more significant than the rest, showing that the acceleration values fluctuated regularly at 16 Hz. This result means that the acceleration in the direction along the span varied for two cycles during each cycle of the main movement at 8 Hz. This can be explained by the fact that the component of vertical force in the span direction did not experience a positive-negative switch when the vertical force changed direction at the balance point. Therefore, a new cycle of acceleration of channel 1 started once the tip passed the balance point.

Figure 6.28 (b), where the accelerations of channel 2 are analyzed in frequency domain, presents several peaks at about the same height. Therefore, the acceleration in the transverse direction can be recognized as a superposition of the main signal and its mechanical harmonics at various frequencies. This difference was because of different sources of acceleration in the span and transverse directions. As mentioned, acceleration in span direction was introduced by a component of vertical force. But the vibrations the specimen tip experiencing during a repetitive movement generated an acceleration in transverse direction. A sequence of harmonic vibrations played important role while the main vibration at 16 Hz still provided the basic frequency.

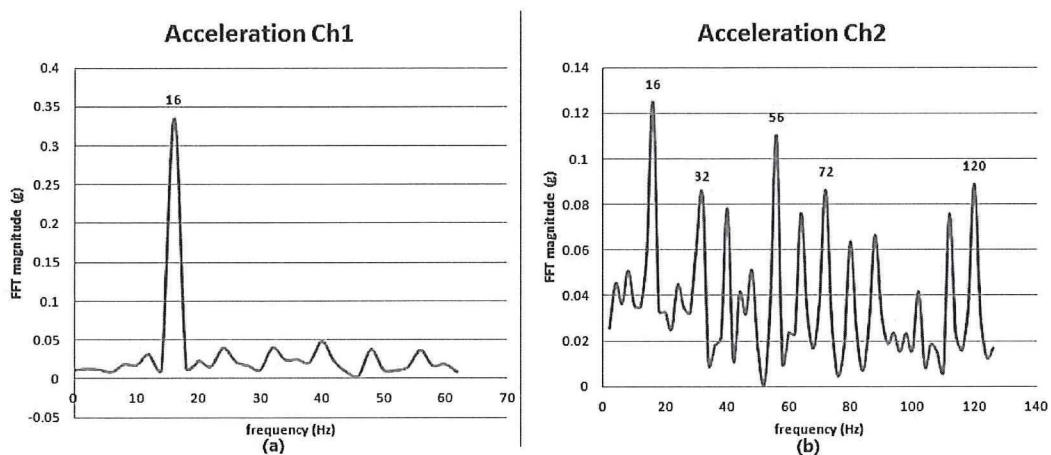


Figure 6.28 Display of accelerations of (a) Ch1 and (b) Ch2 in the frequency domain

In the last section of dynamic tests, strain gauges were connected into a wired system, forming another measurement system. This section topic was to verify the data obtained in the second section, so beam 3 was still the specimen. Due to some range setting problems for employing multiple channels in the PEEKEL system, the measurements of load and strains were not able to provide accurate values. Although the acquiring of absolute strain values was impeded by the error in range setup, ratios of SG2/SG1 and ratios of SG4/SG3 were found to be rather close to those obtained from the WSN. This great similarity in ratios between different local strains has demonstrated the accuracy of the measurement performed by the wireless system in second section. In this way, all results provided by this system in first two sections can be considered reliable.

6.5 Summary

As a main part of the experiments in this thesis, a sequence of dynamic tests was performed on two specimens (beam 2 and beam 3) using a fatigue machine. During these dynamic tests, repetitive movements at 8 Hz or higher frequencies were imposed on the specimen tip in order to simulate a rotor blade flapping. A measurement system incorporating a WSN and wired devices worked to measurement targeted parameters of the specimens. Some movements varying in pattern, amplitude, and frequency were realized by programming the fatigue machine for dynamic tests on each specimen. A metal frame was constructed to clamp the specimen root and it was fixed with the fatigue machine to form a rigid whole. And some connecting parts were specially made to achieve a tight and flexible connection between the specimen tip and the movable head of the fatigue machine. With regard to the measurement system, six strain gauges were mounted on the specimen to measure real-time bending strains and shear strains. A wireless sensor node was attached on the top surface of the tip to monitor local accelerations in three directions during movement. In addition, a load cell placed between the tip and the movable head provided real-time data of force exerted on the specimen. All these target parameters were processed by the measurement system and finally recorded in the time domain.

There were three sections in the dynamic tests. First two sections both applied the measurement system based on the WSN but had tests on beam 2 and beam 3 respectively. Beam 2 is a specimen with great structural integrity while beam 3 was manufactured with an artificial defect, a debonding area between its core structure and its CFRP bottom skin. And in the last section of tests, the WSN was replaced by a wired system and all data were amplified and transmitted to a PC. According to the targeted parameters, the results of dynamic tests and corresponding analysis were presented in aspect of load, strain, and acceleration. For each parameter, its changing trend along with movement variables such as amplitude and frequency is analyzed. More importantly, debonding effects are investigated by comparing the data obtained from two specimens and carrying out further data processing.

Different mounting condition induced by manual clamping and connecting after a specimen replacement results in an inconclusive load comparison between the two specimens. But the force showed a clear upward changing trend along with increasing amplitudes or frequencies for each specimen. In addition, with identical amplitude and frequency, a larger force was needed to excite an asymmetrical movement pattern than that of a symmetrical movement pattern. It is

also found that in each movement, there was a sudden drop of force when the tip reached its highest position, which was caused by a large downward acceleration generated at that moment. In addition to the fundamental movement, a sequence of vibration harmonics with higher orders also can be identified in the force recordings in frequency domain.

With a similar tip displacement, bending strains measured in the dynamic tests were much larger than those in static tests. It was clearly found that bending strains increased in movements with a larger amplitude. The above results relating to bending strains are true for beam 2 and beam 3, but the relation between strain level and movement frequency was different for these two specimens and was even different at different locations. At the location ahead of the debonding area on beam 3, bending strains significantly fell along with increasing frequency while at the same location on beam 2, the bending strains kept constant. At the other side of the debonding area, beam 3 had a stable strain level and beam 2 had a higher strain at the same location when a larger frequency was applied. In general, the two specimens showed different changing trends in bending strain along with frequency and the strain gap became wider at a higher frequency. Because of relatively small values of shear strain, their measurements were severely interfered with by noise. This interference was especially obvious in the tests on beam 2. By performing a noise analysis on the shear strain data obtained from the three test sections, an electrical power supply working at 50 Hz adjacent to wireless sensor nodes was identified as the noise source. So having a good control of the electromagnetic environment can effectively reduce such noise interference.

Since the loading condition cannot be ensured to be consistent for the two specimens, it is better to analyze the ratios between the local bending strains and the relative differences between local shear strains instead of comparing absolute values. A general upward variation trend of bending strain ratio was found along with increasing amplitude and frequency. By comparing the defined ratios on two specimens with various combinations of movement amplitude and frequency, it was possible to draw the valuable conclusion that the debonding area had an obvious influence on the strain distribution between the area and the clamp on the bottom CFRP skin. Although there is no clear clue in the relation between shear strain relative difference and movement variables, a comparison in relative difference between two specimens revealed an important fact that the difference between local shear strains on beam 3 was more than 15% and was about three times that on beam 2. This was because the CFRP frame at the debonding area was damaged and shear stresses were redistributed. The reduced portion of shear stress in the CFRP side walls were carried by the honeycomb core structure according to a new stiffness balance between the area and the clamp.

Three accelerometers integrated in a wireless sensor node were used to measure three orthogonal accelerations of the specimen tip in the span direction, the transverse direction, and the out-of-plane direction. The corresponding data channels in the WSN were channel 1, 2, and 3, respectively. Accelerations in all three directions share an upward changing trend along with movement parameters in dynamic tests. However, the acceleration of channel 3 had a much larger value than the accelerations in the other two directions and it was even beyond the measurement limit of 10 g for the most severe movements. When the acceleration of channel 3 was displayed in the frequency domain, some signals from vibration harmonics can be observed. In addition, accelerations parallel to the top surface varied at 16 Hz instead of the 8 Hz of the

out-of-plane acceleration. This can be explained by their different generating causes: force component and a sequence of vibrations, which are confirmed by analyzing accelerations of channel 1 and channel 2 in the frequency domain.

Chapter 7

Discussion

In this chapter, discussions of experimental results are carried out in aspects of specimens, the WSN, dynamic effects, the debonding, and noise. The results and issues are discussed in more general terms compared with analysis contents in previous chapters.

7.1 Specimen

A test specimen was designed based on a simplified version of the R22 rotor blade. Taking into account factors such as the relatively flat airfoil and profiling difficulty of honeycomb, the test specimen was determined to be a composite beam with a rectangular cross section, which is composed of a honeycomb core structure, two CFRP skins, and two CFRP side walls. According to the design, the structural properties of the specimen should be vertically symmetrical. This symmetry was well proven by stiffness measurements on beams 1 and 2. Their bending stiffness differences in two directions were only 1.6% and 1.3%. This also demonstrated that the manufacturing process was with good quality and provided specimens conforming to the design requirements. Specifically, symmetrical properties of a specimen were ensured by a well-controlled resin infusion process and an appropriate curing cycle in the autoclave. All related manufacturing parameters were optimized after few trials.

A SHM system is mainly used for detecting defects in the targeted structure, so investigating the defect influence on structural responses was the most critical part in efforts to establish a SHM system. According to a survey of various rotor blade defects, a debonding area between the CFRP bottom skin and the core was made as an artificial defect in beam 3. In order to finally obtain a clear and accurate understanding of defect effects on structural responses, the dimensions of the debonding area were relatively large: 25 cm long and 5 cm wide. Because beam 2 and beam 3 were manufactured in one batch with the only difference lying in the debonding area, a comparison between their stiffness can confirm the existence of the debonding after the curing cycle to some extent. In two bending directions, the stiffness dropped by 3% and 32% respectively. In addition, a reduction of the specimen bending strength was observed, which also

provide solid evidence of such structural difference.

It was clearly shown in the stiffness test results that beam 1 and beam 2 had some difference in structural properties although they were identical in design. This was due to variations in manufacturing conditions between different batches. Therefore, static tests and dynamic tests performed on three specimens were set with different experimental purposes according to the specimens. More specifically, the tests on beam 1 were performed to acquire knowledge of specimen structure and structural response to certain loading condition, to verify the working performance of the measurement system based on a WSN, and to optimize the experimental schedule. An identical experimental setup and schedule allowed reliable comparisons between beam 2 and beam 3, which were carried out in order to investigate debonding effects on structural responses in static conditions or various dynamic movements.

7.2 Wireless sensor network

As an important part in static tests, the reliability of the wireless sensor network (WSN) was evaluated by performing measurements with a wired system in a control group. The comparison results showed great consistency for both bending strain and shear strain. Therefore, the measurement system based on a WSN can be considered capable of accurately measuring real-time parameters of specimens. In addition, actual bending strains provided by the WSN had a pretty small difference with their theoretical values. For instance, the actual value at 1 m from the tip on beam 1 was 5.6% larger than its theoretical value, which was calculated based on the exerted tip load. Considering the assumptions involved when obtaining the theoretical strain values, the measured strains were even closer to the theoretical values. So the reliability of the WSN was confirmed again.

In the third section of dynamic tests, a wired system was used to provide reference strain measurements of beam 3. However accurate absolute strain values were found to be hard to acquire due to range setup problem of the wired device applied, especially when multiple channels were activated. Although absolute values could not be determined, the relative ratios between local strains were known and were similar with those obtained from the WSN. So the working performance of the measurement system based on a WSN in dynamic conditions can be approved to a certain extent.

Even though the measurement system based on a WSN was proven able to implement accurate measurements, three technical issues were encountered during tests. First, according to specifications of the WSN, three sensor nodes including ten active channels and sampling at 256 Hz are allowed to work simultaneously in the network with a 75% bandwidth. But sometimes in practice, real-time data transmission from one sensor node stopped in the middle of a measurement. In some cases, the data transmission then continued and had the missing data made up after a short pause. This situation was not improved by setting sampling mode of sensor nodes as low-duty cycle instead of synchronized. Second, data loss occasionally occurred for a few seconds due to wireless environmental interference. Third, a sudden overall data shift was observed for the rare cases. These technical issues had negative influences on the WSN measurement and sometimes called for repeating tests. However, they could be solved by further optimizing the network configuration and setting. And there is no need for urgent concern also

because of their occasional frequency.

7.3 Dynamic effect

Understanding dynamic effects on the specimen structural responses was one of main experimental objectives in this thesis. It was of great importance because the real operation condition of a helicopter rotor blade is highly dynamic with high frequencies involved. Dynamic effects were investigated by means of targeting several parameters with similar deformation states in static tests and dynamic tests. Parameters including force, strain, and acceleration were involved in this investigation.

7.3.1 Force

The force to statically hold the tip of beam 3 at a height of 45 mm was measured to be about 4.3 N. Due to the travel range limit of the movable head of the fatigue machine, the maximum amplitude that could be realized on each side of balanced position was 20 mm. Therefore, the maximum force was measured in a movement, in which the tip traveled between -20 mm and 20 mm at a certain frequency. For instance, the maximum value of force reached in such movement at 8 Hz was about 29 N, which was nearly seven times of the maximum force obtained in static tests. As known from section 6.4.1, asymmetrical movements needed a larger force than symmetrical movements with same amplitude. In addition, the travel range of the tip in this movement was 40 mm, which was still 5 mm less than the largest height in the static tests. Therefore, it is possible to conclude that the force generating a similar deformation state became at least six times larger when an 8 Hz movement was introduced. This was mainly due to the introduction of large accelerations in dynamic movements. For the same reason, peak values of force occurred before the highest position was reached. Because of a different test setup, especially the specimen mounting methods, it is difficult to determine the accurate increment. But a qualitative understanding of dynamic effects on loading can be obtained based on this comparison.

A force comparison among movements with a 10 mm amplitude at three frequencies can be carried out on beam 2 to further understand how a dynamic factor such as frequency affected the structural responses. The maximum force measured in movements at 8 Hz, 12 Hz, and 16 Hz was 7 N, 21.7 N, and 37.1 N respectively. These force values are found to be highly proportional with corresponding frequencies. Even though this highly proportional relation was not clearly observed in other movements, the upward changing trend of the force with increasing frequency can be affirmed. In general, it can be known that a specimen in highly dynamic conditions was subjected to a much larger force than that generating a similar deformation in static conditions. Also, such dynamic effects on force became increasingly severe when higher frequencies were reached. As introduced, the rotor blades of the R22 helicopter flap at 8 Hz in normal operations, so their loading conditions at those moments are pretty severe. And in some irregular maneuvers, rotor blades carry much heavier loads. The significant dynamic effects on the load lead to the conclusion of the necessity of monitoring in the real-time structural health of rotor blades during a flight.

7.3.2 Strain

In the slow dynamic tests, strains measured at the highest position during a movement slower than 1 Hz were compared with the reference strain data obtained in static conditions. Bending strain and shear strain had increments of 10% and 20% respectively when measurements were performed in a repetitive movement at a frequency lower than 1 Hz. In dynamic tests with tip movements faster than 8 Hz, much higher peak strains were measured. Because the movements with the most similar travel range to that of the static test were symmetrical, the valid peak strains of these movements were obtained by calculating the difference between the absolute peak and valley values. The results of both bending strains and shear strains turned out to be approximately twice those measured in static tests. By further increasing movement frequency, strain levels had larger increments. In conclusion in the strain value comparison among different tests, either bending strains or shear strains increased after an introduction of dynamic movements and kept rising along with increasing movement frequency. This was possibly due to the fact that even though the tip displacement was similar, local deformation and stress state were different when movement parameters such as frequency changed. Therefore, frequency should be regarded as a critical movement parameter when analyzing structural responses in a flapping simulation. Also, considering that one important function of a SHM system for rotor blades is to monitor their operational condition, real-time strain measurements may contribute to accomplish this function.

7.3.3 Acceleration

It was proven in one part of the static tests that a wireless accelerometer attachment had a minimal influence on structure responses as long as the attachment position was at the specimen tip, where a vertical force was exerted. According to this result, the accelerometer was attached on specimens in static tests and dynamic tests to perform acceleration measurements. As expected, the acceleration in a static condition, no matter which height the tip was hold at, was -1 g in the out-of-plane direction and 0 g in the in-plane directions. The only non-zero acceleration value represented the gravitational acceleration.

Acceleration recordings of various movements in dynamic tests are analyzed to investigate the relationship between the acceleration and movement frequencies. Because acceleration is closely related to force, an increasing trend of acceleration with higher frequency was found to be similar to the changing trend of force. For instance, the tip acceleration reached 5.8 g for a movement with 10 mm amplitude at 8 Hz. And by increasing frequency to 12 Hz and 16 Hz, the maximum acceleration measured was 12.5 g and more than 20 g, respectively. The latter value cannot be determined as it exceeds the measurement limit of ± 10 g of the accelerometer. It is worth mentioning that the factors of gravitational acceleration and initial condition were excluded since all accelerations used for analyzing were relative values.

7.4 Debonding

As introduced previously, beam 2 and beam 3 were manufactured with identical materials from one batch, so that the different properties between them can be attributed to the existence of the debonding area on beam 3. These two specimens' performance in the stiffness tests confirmed this argument. Beam 3 has 3% and 32% less stiffness than beam 2 in two bending directions. In addition, beam 3 has a bending strength which is smaller as well. These measurements were in agreement with observation of clear local deformation at debonding area.

In order to exclude factors of setup variation, debonding effects were analyzed by comparing relative values of local strains instead of absolute strain levels. The relative values of bending strains of beam 2 and beam 3 were similar while a large difference was found between their shear strain measurements. Specifically, beam 3 experienced a significant change in shear strain at the two sides of the debonding and beam 2 had nearly same shear strain at these two locations. This result suggests that a shear strain variation between two sides of the debonding area may provide valuable information regarding debonding. By applying a relative difference of shear strains for data processing in dynamic tests, the argument was proved to be also true in fast repetitive movements. A relative difference of shear strain of more than 15% was induced by the debonding while this value was only 5% for the specimen without debonding, which means that existence of this defect significantly influenced the shear strain distribution near its location. Some differences regarding bending strain ratios can be found as well, but the rule was not clear and was relatively complex to understand. In conclusion, the debonding had a much more significant effect on shear strain distribution rather than that of bending strain. And the relative difference value between local shear strains has great potential to be used as an indicator for debonding since a quantified result may be obtained from the value.

7.5 Noise

The experiments encountered three main noise issues. Firstly, a 14 Hz noise seriously impacted on the strain measurement on beams 2 and 3 in static tests and was identified as electrical noise caused by the bridge circuit. Several remedies feasible in the experimental schedule were performed to eliminate or reduce this noise. These remedies included improving wiring connection and electromagnetic environment, and adding bypass capacitors over resistors. However these operations were ineffective in making an obvious change in the noise signal. In the premise of keeping same strain gauge layout and same number of active channels, two methods could possibly solve this noise issue by abandoning the external bridge circuit. Internal modifications of bridge completion resistors of sensor nodes can be carried out by the manufacturer or a printed circuit board (PCB) could be made and screwed to terminals of the sensor node for completing the bridge circuits. Other options include applying more sensor nodes to share measurement channels and using strain gauges with higher resistance to limit the current.

Secondly, an intense noise at 50 Hz occurred in strain measurements in one dynamic test. This noise was at a typical frequency of an electrical signal. By comparing the test setup with other

tests that did not have this noise, it is determined that the noise source was an electrical power supply working at 50 Hz nearby the sensor nodes and the base station. The noise signal was transmitted to the WSN by means of induction. Although this issue can be easily solved by keeping the components of the WSN a certain distance away from other electrical elements, the susceptibility of the WSN to complex electromagnetic environments was shown. Due to the fact that such noise can largely influence the measurement accuracy, a design to prevent electromagnetic interference in an operation environment is required when applying a WSN. Thirdly, noises were caused by mechanical harmonics in dynamic tests. Strictly speaking, these signals should not be classified as noise because they represented the actual situation of the specimen. However their existence made it harder to extract useful data from measurements. Useful data herein refers to targeted parameters related to the fundamental movement.

7.6 Summary

Based on the results of the stiffness test, specimens were proved to be manufactured with properties in accordance with design. A debonding area was artificially made on beam 3. It was hard to check its existence by visual inspection, but a reduction of bending stiffness and strength was observed and was regarded as solid evidence of the debonding. Regarding to the WSN, the reliability of its measurement results was verified by performing comparisons with wired system measurements and with theoretical values. In addition, the WSN was capable of acquiring accurate real-time data of specimens in highly dynamic conditions. Such operational applicability needs to be ensured when the WSN is proposed to accomplish reliable measurements in a SHM system for rotor blades. During experiments, there were several technical issues of applying the WSN. These issues included data transmission pause in multiple-channel operation, transitory data loss, and an overall data shift. They call for further work in the WSN configuration optimization and setup improvement.

A vertical load was exerted on the specimen tip to generate the required deformation. In the static tests, the targeted parameters with this deformation were measured as reference data. And in dynamic tests, the deformation was made in order to simulate flapping. Therefore, the force was applied only for an experimental need and was not related to the measurements of the WSN. However, an investigation of dynamic effects on the exerted force can be of benefit for better understanding of the simulation condition. To generate similar deformation in movements at frequencies higher than 8 Hz, a force several times larger than that in static condition was required. So it can be concluded that highly dynamic movements such as rotor blade flapping involve a severe loading situation. Therefore, as critical structures of a helicopter, rotor blades need a real-time SHM system during operations. Dynamic effects on measured strains of the specimen were also obvious. Strains experienced an increment up to 20% when a movement at 1 Hz was introduced. Also, strains measured in dynamic tests were found to be about twice as those measured in static tests, which suggests that frequency is a critical parameter to consider in strain measurements in the flapping simulation. In addition, the acceleration in an 8 Hz movement in dynamic tests can reach 6 g and went even higher when the movement frequency further increased.

Investigating debonding influence on the structural response in the flapping simulation is of great

importance because one main function of a SHM system on rotor blades is to detect potential defects by real-time measurement. Since the mounting and clamping condition changed after specimen replacement, it was not reasonable to simply compare strain levels between two specimens. Therefore, bending strain ratio and relative difference of shear strain were defined and used in comparisons. The comparison of the former showed an unclear result, which required more tests to verify. And the latter had a much larger values on the specimen with debonding. A difference of more than 15% was found between local shear strains at two sides of the debonding, which meant that the debonding had a significant influence on shear strain distribution. In conclusion, the relative difference of local shear strains can be used as an indicator for the debonding.

Several noise issues were encountered during experiments. One of them was caused by external bridge circuits used in the strain measurements and could be solved by internal modification of sensor nodes or usage of a printed circuit board. Some noise signals represented a sequence of mechanical harmonics in addition to the fundamental movement driven by fatigue machine. The most annoying noise was induced by a nearby electrical power during dynamic tests and was eliminated by changing positions of the WSN components. The intense interference of this noise is a reminder of the susceptibility of the WSN to a complex electromagnetic environment, which needs extra attention when a WSN is employed in SHM system.

Chapter 8

Conclusion and Recommendation

8.1 Thesis work review

The main work of this thesis is to establish an SHM system based on WSNs for rotor blades. According to the structure and materials of a rotor blade, test specimens were designed and manufactured. Among them, one specimen was manufactured with an artificially introduced debonding area. Experiments including stiffness tests, static tests, and dynamic tests were performed on these specimens in order to obtain better understanding of dynamic effects, to investigate influences of the debonding, and to identify potential defect indicators, which can be targeted in the data processing of a SHM system. In addition, the verification of reliability and applicability of the WSN was also a main objective of these experiments.

8.2 Results

Rotor blades are designed with great strength to take loads but with a stiffness that is not too high to obstruct the necessary deformation for balancing lift. For this reason, composite materials including a honeycomb structure and CFRP were used to manufacture test specimens. It was verified in the tests that without damaging structure, specimens can have deformation similar with that of real rotor blades during flapping. Such a property of the specimens can add credence to arguments made from analysis of experimental results.

During the calculation process, it was assumed that all bending stress was carried by the CFRP skins. Based on this assumption, the flexural modulus of CFRP materials was calculated to be about 100 MPa. Commercial CFRP materials with 60% fiber volume often have a flexural modulus of 125 MPa. By taking the factor of using a homemade resin infusion process into account, the actual value of flexural modulus of the material was lower than 125 MPa and close to the calculation result. As a result, it is proven that the assumption is valid and that the CFRP material contributed to taking almost all bending stress. Similarly, the assumption that the CFRP walls play negligible roles in taking shear stress is proven by experimental results. In general, basically all

bending moment was taken by the CFRP material and all shear stress was carried by the honeycomb core. In addition, the results of static tests also confirmed the theoretical relation between local strains, which is different for bending strain and shear strain. All this work became an important part of the theoretical foundation for analysis and discussion in this thesis.

The reliability of the WSN applied in this thesis was verified by strain calculation results and measurements of a wired system in static tests. Also, the measurement system incorporating the WSN was proven to be applicable of performing real-time data measurement and transmission in highly dynamic conditions. The performance of the WSN in all tests suggested that it can be a good candidate to be employed in an on-board SHM system for rotor blades.

Parameters of force and strains on specimens measured in static conditions and repetitive movements were compared to analyze the dynamic effects on the structural response. As a result, forces and strains obtained in movements with similar deformation were found to be much larger. For instance, the force on tip increased by seven times and bending strains doubled. Due to such significant dynamic effects, rotor blades experience extremely severe loading and deformation during operation. Parameter increments induced by dynamic effects can be partially explained by an introduction of acceleration, which went beyond 10 g in each direction in the most severe movements. The out-of-plane acceleration varied at a frequency which was the same as that of the movement and the accelerations parallel to the specimen top surface varied at a frequency of twice of the movement frequency. Therefore, it was possible to monitor the operational frequency of the rotor blades by acquiring real-time accelerations via wireless sensor nodes.

For the specimen without debonding, shear strains measured at two locations were close both in the static tests and the dynamic tests, which can be expected based on theory. But their counterparts on the specimen with debonding were found to have a much larger difference. In all repetitive movements in dynamic tests, there was about 15% relative difference in the shear strains measured at both sides of the debonding area. The existence of debonding between the core and the bottom CFRP skin damaged the CFRP frame in that area and induced a redistribution of shear stress between the CFRP material and the honeycomb structure, resulting in a reduced shear strain on the CFRP side walls between the debonding and the clamped end. Based on this experimental result, the difference of shear strains measured at multiple locations on the side walls can be considered as a good candidate to detect defects such as debonding. So along with accelerations, shear strains are identified as valuable indicators of operational condition and potential defects.

It can be concluded from signal noise analysis for the dynamic tests that measurements performed with the WSN can be influenced by an intense electromagnetic environment. For instance, an electrical power supply placed nearby components of the network imposed a noise signal at 50 Hz on data transmitted via the wireless network possibly by means of induction and made it difficult to process these data. Such susceptibility of the WSN to electromagnetic interference can be put aside in a laboratory environment but could be a serious issue in its application on helicopter rotor blades. Some improvements in design or configuration of the WSN itself are required to ensure a reliable data transmission between distributed sensors and on-board devices, even in a complex electromagnetic environment.

8.3 Limitations

Although the experimental results are valuable, it needs to be admitted that there are several main limitations of the work in this thesis. First, repetitive movements in dynamic tests were operated to simulate flapping of rotor blades. Since a rotation around the hub can be considered as a fundamental movement pattern of rotor blades, a rotating test system would be the best option to perform dynamic tests. Such a rotating system is not equipped in laboratory at present, so one end of the specimen was clamped by a fixed structure. In addition, minor movements of feather, lead, and lag were excluded in this thesis. When considering that the debonding specified in tests mainly affects the bending resistance of the specimen, which is closely related to rotor blade performance in flapping, it is reasonable to target flapping as a preferred movement when a comprehensive experimental simulation cannot be performed.

Secondly, debonding was determined to be one of most critical defects for composite rotor blades in the literature study and an artificial debonding area was made for the tests on behave of defects. Debonding was selected from various defects because it brings significant reductions of structural properties, causes a severe issue of water penetration, and has risk of fatigue crack growth during operation. However, it is important to have additional types of common defects tested to establish a practical SHM system. Other limitations of the current work included a travel range limit of the specimen tip in the simulated movements, poor control of the experimental environment, and limited repeating tests for result verification. Based on calculations, a travel range of 60 mm was expected in the flapping simulation. In fact, the actual maximum range in tests was 40 mm, which was determined by limit positions of the movable head of fatigue machine. Regarding to the experimental environment, there were other fatigue machines nearly sharing same hydraulic system with the one used in dynamic tests and electrical interference can be caused by various electrical components in the laboratory. A better experimental environment may be achieved by applying an individual actuator instead of a fatigue machine and using a special testing room. Lastly, the number of repeated tests was far less than the number needed to draw a solid conclusion based on measurement results.

8.4 Recommendations

For future research, the main tasks are manufacturing specimens with a rotor blade aerodynamic profile, operating tests with various defect types and sizes, introducing more movement patterns in the experimental simulations, performing a sequence of full scale tests, and carrying out a research on energy harvesting solutions for wireless components in the WSN.

Due to the difficulty of profiling a honeycomb structure with small thickness, specimens were designed with a rectangular cross section. An aerodynamic profile should be included in the specimen design for future research if possible due to the fact that it can affect stress distribution to some extent. A debonding between the bottom CFRP skin and the core was used as an embedded defect needing to be detected. In addition to debonding, other common defects such as delaminations, cracks, voids, and inclusions have a chance to damage structural integrity of rotor blades and bring a risk in operational safety. Therefore, a comprehensive investigation of system applicability to various possible defects is required for establishing a SHM system. Also,

different defect sizes may affect the rotor blade performance differently and need to be included in future work as well.

As mentioned, rotor blade flapping was targeted to be simulated during tests in this thesis. In order to simulate movement patterns of leading and lagging, an actuator can be installed horizontally to generate specimen deformations in the transverse direction. And it is possible to simulate a feathering by clamping the specimen root to a torque testing machine. A test setup able to accomplish simulations of these movement patterns individually or simultaneously is beneficial in the substantive stage of establishing an SHM system. Also, all research findings and conclusions need to be verified in a sequence of full scale tests on a rotary test platform, which allows a flexible hinge connection between the specimen and the rotor hub.

In experiments, wireless sensor nodes were powered by their integral batteries and needed to be recharged after each test. Battery charging process is not feasible when considering a long-running operation and their locations on a rotor system. Energy harvesting is a process to capture and use ambient waste energy for powering low-powered electronics. Compared with a photovoltaic solution, the usage of radiation or thermal energy, wind energy harvesting, and vibration energy harvesting based on an application of piezoelectric materials is more applicable in the case of a WSN for rotor blades. Direct usable voltage outputs are allowed by a large power density of these materials, which is comparable to that of a lithium-ion battery, and the severe vibrating conditions during rotor blades operation. An alternating voltage output can be induced by the dynamic strain occurring in vibration and can be converted to direct electrical energy for driving wireless sensor nodes or recharging a battery. Therefore, work related to vibration energy harvesting is proposed in the schedule of future research. Firstly, a piezoelectric patch can be bonded onto the specimen and its power output measured with a number of load resistors determines optimal load resistance. Secondly, output power of the piezoelectric patch can be characterized during dynamic tests at three frequencies of 8 Hz, 12 Hz, and 16 Hz. Thirdly, based on the energy generation, the sampling mode and sampling rate of the wireless sensor nodes are configured. After connecting an energy storage capacitor to the node, tests with a piezoelectric harvester are conducted to examine its performance in highly dynamic condition. By partially or completely replacing batteries by piezoelectric harvesters to power wireless sensor nodes, the applicability of the WSN and the SHM system based on it can be largely improved with better endurance.

8.5 Design proposal

Based on the experimental results, especially those obtained from the dynamic tests with frequencies at least 8 Hz, a physical design of a SHM system incorporating a WSN for rotor blades is proposed. As shown in figure 8.1, two types of sensors are applied to measure real-time structural parameters.

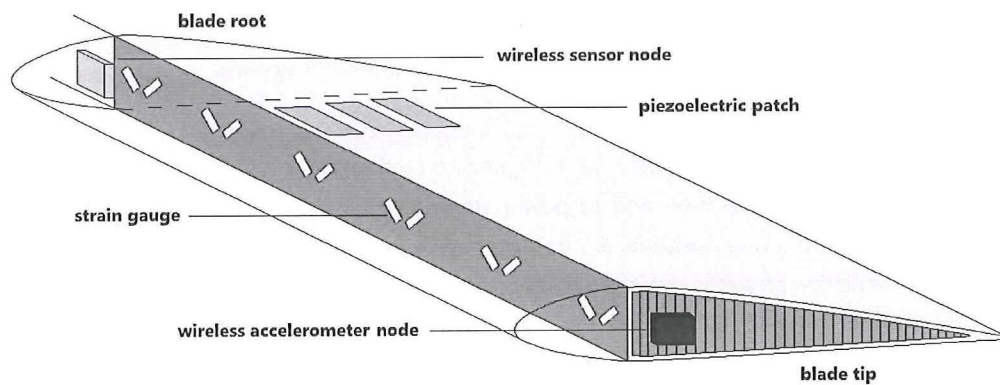


Figure 8.1 Physical design of SHM system components on a rotor blade

Several pairs of strain gauges are mounted on the front surface of the spar and each pair forms a measurement bridge with two resistors. Shear strains on this surface are measured by these strain gauges and the electrical outputs from bridges are sent to a wireless sensor node, which is located at the root of the rotor blade. According to the results from the dynamic tests, the shear strains are expected to be approximately same at every measuring location. Even though during flapping, the vertical load is distributed along the rotor blade span instead of an end load at the blade tip, the part further from the root experiences a larger load due to higher linear speed. Therefore, shear strains along the blade span are on a stable level and the locations near the root have slightly larger shear strains. With the presence of a debonding between the CFRP facing materials and the honeycomb core on the upper surface, bottom surface or front surface, there will be a sudden change in the shear strain, which can be identified by comparing measurement results from two adjacent pairs of strain gauges located near the debonding. In this way, it will be possible to locate the debonding by knowing its distance from the blade root and to characterize the size of the debonding. The latter function can be accomplished by establishing a database containing the relationship between strain change and the debonding size. The number of strain gauges and the interval between adjacent pairs are determined by the dimensions of the target rotor blade and the safety requirements with regard to defect size. In addition to identifying debondings, shear strain measurements also allow an accurate monitoring of load for the rotor blade.

A wireless accelerometer node mounted at the blade tip within the fairing measures real-time accelerations in three directions: the direction along the span, the transverse direction, and the direction perpendicular to the blade bottom surface. The acceleration in the last direction offers information about the local loads, the flapping frequency, and therefore the rotating frequency. Similarly, the acceleration in the transverse direction can offer information about the movement related to lead-lag of the rotor blade. It is also possible to get knowledge of resonant or harmonic vibrations by analyzing the frequencies of acceleration data. In general, the accelerometer node is applied for monitoring the operational condition of the rotor blade.

The wireless sensor node located at the blade root and the wireless accelerometer node both perform real-time wireless data transmissions to a base station in the helicopter fuselage, which is connected to an on-board PC. The data transmitted to the PC are recorded in a database. Useful data are extracted and analyzed by applying certain algorithms to get an assessment result.

When a debonding larger than the tolerant size is detected or the rotor blade operation is found to be abnormal, the SHM system will inform the pilots or the autopilot system.

It also can be seen in figure 8.1 that there are piezoelectric patches mounted on the bottom surface of the blade near the root. They are designed to continuously harvest energy from the blade deformation during operation and to power those two wireless sensor nodes or charge their batteries. Their mounting positions are determined by considering that the bottom surface has a smaller possibility of water penetration and that the blade root has the largest bending strains. The number of piezoelectric patches needed depends on the sampling mode of the wireless sensor nodes and its power supply scheme.